IS-T--1513

DE91 012024

Electronic Excitation Transport in Photosynthesis and Crystal and Molecular Structures of Porphyrin Compounds

by

Yang, Shumei

PHD Thesis submitted to Iowa State University

Ames Laboratory, U.S. DOE

Iowa State University

Ames, Iowa 50011

Date Transmitted: April 22, 1991

PREPARED FOR THE U.S. DEPARTMENT OF ENERGY

UNDER CONTRACT NO. W-7405-Eng-82.

DISCLAIMER

Printed in the United States of America

Available from
National Technical Information Service
U.S. Department of Commerce
5265 Port Royal Road
Springfield, VA 22161

Electronic excitation transport in photosynthesis and crystal and molecular structures of porphyrin compounds

Shumei Yang

Under the supervision of W. S. Struve and R. A. Jacobson
From the Department of Chemistry
Iowa State University

The excitation energy transfer in three photosynthetic organism samples, Bacteriochlorophyll a-protein from Prosthecochloris aestuarii, and Chl/P700~60 and Chl/P700~200 from spinach, have been investigated by pump-probe ultrafast spectroscopy. The isotropic photobleaching profiles were best described by two exponential decay components in Bchl a-protein and Chl/P700~60, and three exponential decay components in Chl/P700~200. The experimental results from the three samples show that nonrandom chromophore orientations exist and Sauer's "pebble mosaic" model is an appropriate one for excitation transfer in these samples. The polarized pump-probe transients have been analyzed in terms of an exciton hopping model that incorporates the known geometry of the Bchl a-protein.

The crystal and molecular structures of four metalloporphyrins have been determined by X-ray diffraction and molecular mechanics. The results are summarized as follows:

$(H_2O)MgT(OME)PP.HCCl_3$: monoclinic, a = 15.966(5), b = 9.192(1), c = 14.882(4) Å, and β = 100.38(2)°; space group I2; R = 0.068, R_w = 0.070. Intermolecular hydrogen bonding results in the formation of two-dimensional infinite polymers.

$[cis\text{-}(ala)_2DPE]Ni(II).CHCl_3.CH_3OH$: monoclinic, a = 14.195(5), b = 12.175(6), c = 28.071(1) , and β = 98.97(3)°; space group $P2_1/n$; R = 0.085, and R_w = 0.089. The average Ni-N distance is 1.92 Å and N-Ni-N bond angles range from 88.1(4)° to 92.3(4)° indicating that the Ni environment is essentially square planar.

$[Ni(DPE)]\text{-}(py)_2.2CHCL_3$: triclinic, a = 14.306(4), b = 14.719(5), c = 14.296(5) Å, α = 94.86°, β = 98.97(3)° and γ = 63.452°; space group $P\bar{1}$; R = 0.049, and R_w = 0.064. The average Ni-N distance is 1.92 Å and N-Ni-N bond angles range from 88.5(1)° to 91.9(1)°. The distance between the two terminal nitrogen atoms is 11.4 Å.

$[Ni(DPE)]\text{-}(py)_2.H_2O$: monoclinic, a = 14.240(2), b = 25.418(4), c = 14.725(5)) Å, and β = 96.38(3)°; space group $P2_1/n$; R = 0.081, and R_w = 0.107. The average Ni-N distance and

N-Ni-N bond angle are 1.93 Å and 90.2°, respectively. The distance between the two terminal nitrogen atoms is 7.6 Å.

Electronic excitation transport in photosynthesis

and

crystal and molecular structures of porphyrin compounds

by

Shumei Yang

A Dissertation Submitted to the

Graduate Faculty in Partial Fulfillment of the

Requirements for the Degree of

DOCTOR OF PHILOSOPHY

Department: Chemistry
Major: Physical Chemistry

Approved:

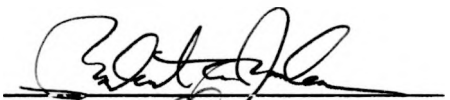

In Charge of Major Work

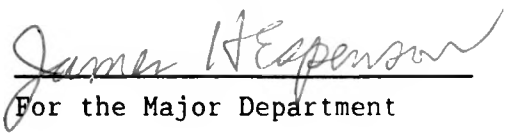

For the Major Department

For the Graduate College

Iowa State University
Ames, Iowa

1991

Table of Contents

GENERAL INTRODUCTION

Photosynthesis is a gigantic and sophisticated complex of physical and chemical engineering, whereby solar energy is converted into chemical potential.

$$CO_2 + H_2O \rightarrow O_2 + (CH_2O) + 112Kcal/mole\ CO_2$$

This highly complex process is initiated when light is absorbed by a pigment molecule within the photosynthetic membrane. Then, the absorbed energy is transferred to reaction centers by these pigments, where chemical reactions happen.

This dissertation will deal with the aspects pertaining to the very early stages in photosynthesis: the excitation energy transfer (EET) after light is absorbed by pigments and the structures of Mg porphyrin and other metal porphyrins which may provide some structural information for pigment molecules.

Explanation of Dissertation Format

An alternate format is used in this dissertation. The whole dissertation is basically divided into two parts: EET in photosynthesis and the X-ray crystal structures of metal porphyrin compounds. Sections I-IV deal with the EET and Sections V-VIII discuss the porphyrin structures. Each part includes one section of literature review (Section I and V, respectively) and three published or submitted papers. Each section contains a

separate list of references. All of the published or submitted papers are kept in the original style except for the references, which have been changed based on the ACS STYLE Guide.

SECTION I. REVIEW OF ELECTRONIC ENERGY TRANSFER

INTRODUCTION

A variety of processes can happen after a molecule is excited by a photon. The possible fates of photoexcited molecule are shown in Fig. 1.1. In summary, these processes include:

1. $M + h\nu \rightarrow {}^1M^*$ (absorption)

A molecule is excited to a singlet excited state by a photon.

2. ${}^1M^* \rightarrow M + \Sigma\Delta\varepsilon_i$

The singlet excited molecule may go back to the ground state by internal conversion(vibrational relaxation), or releasing the photon(fluorescence), or energy transfer.

3. ${}^1M^* \rightarrow {}^3M^* \rightarrow M + \Sigma\Delta\varepsilon_i$

The excited molecule may jump from a singlet to triplet state by intersystem crossing; and then back to the ground state by phosphorescence, or internal conversion.

4. ${}^1M^* \rightarrow$ product

The excited molecule may dissociate to form a new compound.

In this chapter, we mainly deal with one of these processes: singlet excitation energy transfer.

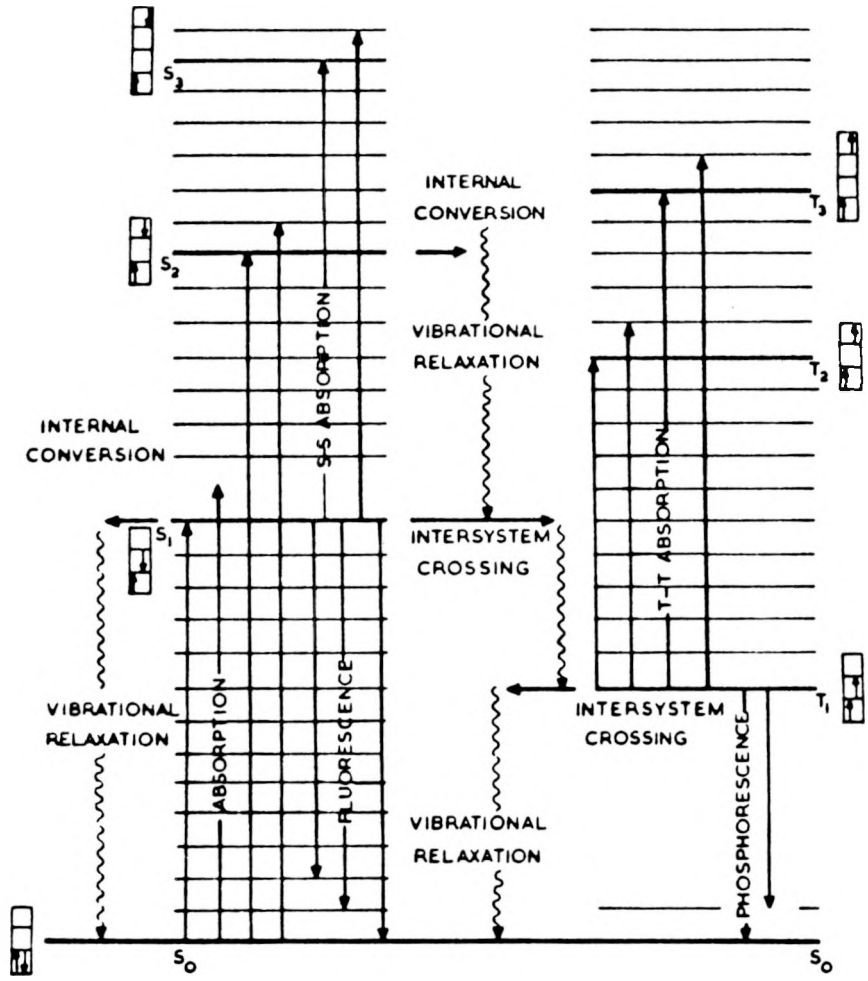

Figure 1.1 Jablonskii diagram showing fates of photoexcited complex polyatomic molecule.

TRANSFER OF ELECTRONIC EXCITATION ENERGY

Direct evidence of energy transfer between different molecules (or atoms) is provided by sensitized fluorescence. A mixture of D (donor) and A (acceptor), when irradiated with the light of the D resonance line, shows the emission (fluorescence) spectrum of A (or both). Since A molecules do not absorb the exciting light, they can be excited only indirectly by an excitation transfer from D (Fig. 1.2). This type of energy transfer is caused by neither re-absorption nor collision. It is a non-radiative transfer, which is caused by inductive resonance or mutual coupling between the electronic systems of both molecules.

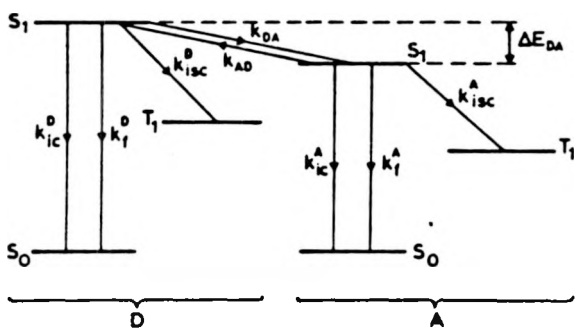

Figure 1.2 Diagram illustrating the various decay pathways of the donor D and the acceptor A. S, singlet; T, triplet levels. k_f, rate constant of fluorescence; k_{ic}, rate constant of internal conversion; k_{isc}, rate constant of intersystem crossing; k_{DA} (k_{AD}), rate constant of energy transfer from D to A (A to D).

What Is an Exciton ?

The rate of energy transfer can be calculated from exciton theory ([1]-[5]). A molecular exciton is an excited state of a condensed system which very closely resembles a molecular excited state, either as a coherent delocalized combination of states or as a localized excitation which hops from site to site[3]. Roughly, the formation of an exciton process is a two stage matter. Immediately following its creation, the motion of an exciton is wavelike (sometimes called coherent, and the excitation is delocalized between molecules), and after a certain period of time (around a subpicosecond, dephasing process), it becomes hopping (or incoherent, and the excitation is localized on a certain molecule).

The Rate of Energy Transfer

According to exciton theory, the excitation can occur on both D and A, and the states of the system should be linear combinations of the locally excited states $\phi_D^1\phi_A^0$ and $\phi_D^0\phi_A^1$ (the ground (S_0) and first excited (S_1) singlet states of D and A are described by normalized wave function ϕ_D^0, ϕ_A^0, ϕ_D^1, ϕ_A^1). The initial state (where only D is excited) is given by Dexter[6]

$$\Psi_i = 1/\sqrt{2}\,[\phi_D^1(1)\phi_A^0(2) - \phi_D^1(2)\phi_A^0(1)] \qquad (1.1)$$

and the final state(where only A is excited):

$$\Psi_f = 1/\sqrt{2}\,[\phi_D^0(1)\phi_A^1(2) - \phi_D^0(2)\phi_A^1(1)] \tag{1.2}$$

The energy transfer is caused by the interaction of the electron clouds of the donor and acceptor. Suppose V_{DA} represents this interaction. The probability that energy is transferred from a particular donor (D) to a particular acceptor (A) is of the form

$$P_{DA} = (2\pi/\hbar)\rho_E\,|\int\psi_i V_{DA}\psi_f d\tau|^2 \tag{1.3}$$

where ρ_E is the density of states. Therefore, the rate of energy transfer from the initial to the final state is governed by the interaction matrix element:

$$\begin{aligned}\langle V_{DA}\rangle &= \langle\psi_i|V_{DA}|\psi_f\rangle \\ &= \langle V_{DA}\rangle' + \langle V_{DA}\rangle''\end{aligned} \tag{1.4}$$

where
$$\langle V_{DA}\rangle' = \langle\phi_D^1(1)\phi_A^0(2)|V_{DA}|\phi_D^0(1)\phi_A^1(2)\rangle \tag{1.5}$$

$$\langle V_{DA}\rangle'' = \langle\phi_D^1(1)\phi_A^0(2)|V_{DA}|\phi_D^0(2)\phi_A^1(1)\rangle \tag{1.6}$$

From Eq. 1.4 we can see that there are two contributions to energy transfer: Coulomb $\langle V_{DA}\rangle'$ and electron exchange $\langle V_{DA}\rangle''$. The Coulomb contribution is usually the dominant term. The exchange term contributes to excitation transfer only if the Coulomb term is small(or zero when optically forbidden transitions are

involved) and the distance between the donor and acceptor is small (the electron-exchange needs some overlap of the electron clouds of both molecules). We mainly discuss the Coulomb contribution in the following.

There are two limiting cases in the Coulomb contribution based on exciton theory. In the coherent stage, the electronic systems of donor and acceptor molecules are strongly coupled. The true eigenstates are $(\phi_D^1\phi_A^0 \pm \phi_D^0\phi_A^1)/\sqrt{2}$ with an energy splitting Δ. The "quasi-transfer rate" is given by Förster[2]

$$k_{D\rightarrow A} = 4|U|/h \tag{1.7}$$

where, U is the interaction energy which arises from the interaction of charges on the molecules. Using the dipole approximation,

$$U = (|\mu_D| \ |\mu_A| \ / \ R^3) \ \kappa \tag{1.8}$$

$$\kappa = \cos\alpha - \cos\beta_D\cos\beta_A \tag{1.9}$$

where α is the angle between the donor and acceptor dipoles, and β_D (or β_A) is the angle between donor (or acceptor) dipole and the vector connecting the two dipoles.

Indeed, there is practically no meaning to "transfer" if the coupling is so strong that both the donor and acceptor are always coherently excited to one of the above states.

In the incoherent stage, the electronic systems of donor and acceptor molecules are weakly coupled. The locally excited states are $\phi_D^1\phi_A^0$ and $\phi_D^0\phi_A^1$. Assuming a thermal equilibrium distribution over the vibrational levels of both molecules, the transfer rate originally given by Förster [2] is

$$k_{D\rightarrow A} = 1/\tau_D^\circ \; [R_0 \; / \; R_{DA}]^6 = 1/\tau_D \; [\bar{R}_0 \; / \; R_{DA}]^6 \qquad (1.10)$$

$$\tau_D = \eta_D^\circ \; \tau_D^\circ \qquad (1.11)$$

τ_D is actual mean lifetime of donor. It is connected to τ_D° (the intrinsic lifetime of molecule D) and η_D° (the fluorescence yield of the donor in the absence of the acceptor), and the $\bar{R}_0$ is the acceptor distance at which transfer competes equally with the total donor deexcitation rate and is given by

$$\bar{R}_0^6 = \frac{9000\kappa^2(\ln 10)}{128\;\pi^5\;n^4\;N} \int f_D(\omega)\varepsilon_A(\omega)\omega^4 \; d\omega \qquad (1.12)$$

In typical cases, R-values from 50 to 100 Å have been calculated.

From Eq. 1.12 we can see that the energy transfer in weak coupling occurs when the absorption spectrum of the acceptor overlaps with the fluorescence spectrum of the donor. This condition is somewhat similar to that for reabsorption of the donor fluorescence by the acceptor. Nevertheless, the mechanism of the energy transfer process is an entirely different one,

leading to transfer before the emission of the donor fluorescence takes place; also it needs some amount of mutual coupling between donor and acceptor which takes place only over limited distances.

A summary of ET rate expressions and conditions is shown in Table 1.1.

Table 1.1 Energy transfer rates

Coulomb Contribution			Electron Exchange Contribution
Strong Coupling		Weak Coupling	
Condition	$\langle V_{DA}\rangle' \gg \Delta E$ ΔE is a measure of the bandwidth of the electronic transitions involved ($A \rightarrow A^*$ and/or $D \rightarrow D^*$).	The abs. spectrum of the acceptor overlaps the fl. spectrum of the donor. Thermal equilibrium distribution over the vibrational levels of both molecules – R_o: 50 ~ 100Å	Coulomb contribution is small; distance between donor and acceptor is very short (<4Å)
State	$\psi = \frac{1}{\sqrt{2}}(\phi_D^1 \phi_A^0 \pm \phi_D^0 \phi_A^1)$	$\phi_D^1 \phi_A^0$, $\phi_D^0 \phi_A^1$	
Rate Constant	$\kappa_{DA} = 4C\langle V_{DA}\rangle'$ ($\kappa_{DA} \sim 10_{13}\ s_{-1}$) dipole approximation: $\kappa_{DA} = 4\|u\|/h$ $u=(\|\mu_D\|\|\mu_A\|/R^3)\kappa$ $\kappa = \cos\alpha - \cos\beta_D \cos\beta_A$	$\kappa_{DA} = \frac{1}{\tau_D}[\bar{R}_o/R_{DA}]^6$ ($\kappa_{DA} \sim 10^{12}\ s^{-1}$)	$\kappa_{DA}^{EX} = (2\pi/h)^2 (\langle V_{DA}\rangle'')^2 \int F_D(\upsilon)\, d\upsilon$ ($\kappa_{DA} \sim 10^{12}\ s{-}1$)

ENERGY TRANSFER IN PHOTOSYNTHESIS

In photosynthesis, light energy is absorbed and transferred by antenna chlorophyll molecules to the reaction center, where chemical reactions occur. There are two categories of transfer in photosynthetic systems. The first one is the energy transfer between nonidentical chlorophyll (Chl.) molecules (sometimes called heterogeneous transfer), which is usually down an energy gradient (Fig. 1.3). The second one is the transfer between identical chl. molecules that surround and interconnect the reaction centers, where trappings take place. The latter is the subject we mainly discuss here.

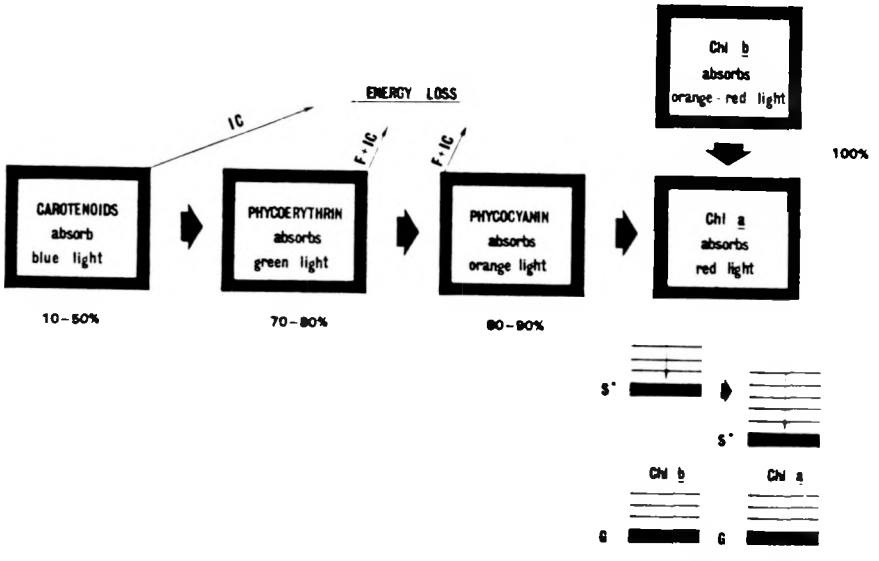

Figure 1.3 Diagrammatic scheme for excitation energy transfer. F: fluorescence; IC: internal conversion; G: ground state; S^*: excited singlet state. The numbers, in percent, refer to the efficiency of energy transfer from various pigments to Chl a.

In the previous discussion, the energy transfer rates have been based on two limiting cases: strong-coupling and weak-coupling. Which one applies to energy transfer in photosynthesis? Generally, the situation approaches the case of "weak coupling"[7], in which the excitation moves around from molecule to molecule in a random walk. Some lattice models have been developed depending on the photosynthetic unit concept (a group of antenna chlorophylls, typically 300 Chls., is associated with one reaction center and referred to as a photosynthetic unit, PSU). In Fig. 1.4a, a "lake" model is shown, where there is no separation between PS units, and if one reaction center closed, excitation energy can emigrate to another one; in Fig. 1-4b, a "puddle" model is shown, where the PSUs are independent, each unit is isolated, and there is no excitation energy exchange among the different units. It seems that the "lake" model is to be preferred. Recently, Sauer[8] proposed a "pebble mosaic" model (Fig. 1.5), in which clusters of chl. molecules constitute the lattice. The chls. within the cluster are "strong-coupling", and the interaction between clusters are "weak-coupling". This model is generally accepted in Bchl a-protein, where 7 Bchls are enclosed within an envelope of protein (subunit), with three subunits being related by a threefold symmetry axis. It has been

shown in our experiments (Section II) that the EET within the subunit obeys the "strong-coupling" mechanism, and the EET between subunits follows the "weak-coupling" mechanism. More recently, similar phenomena have been observed in a Chl/P700~200 sample (Section IV), where the various chl a spectral forms are grouped into heterogeneous clusters of chromophores, "strong-coupling" governs the EET within the cluster and "weak-coupling" controls the EET between the clusters.

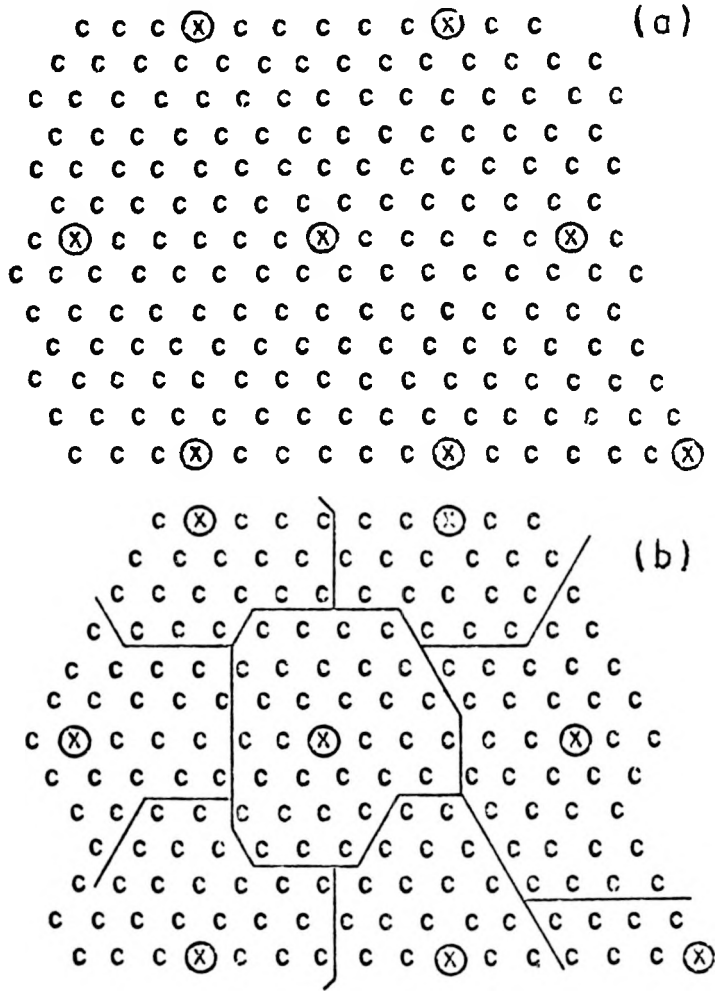

Figure 1.4 Schematic representation of the lake (a) and puddle (b) models of PSU interaction. ⊗ stands for the reaction center.

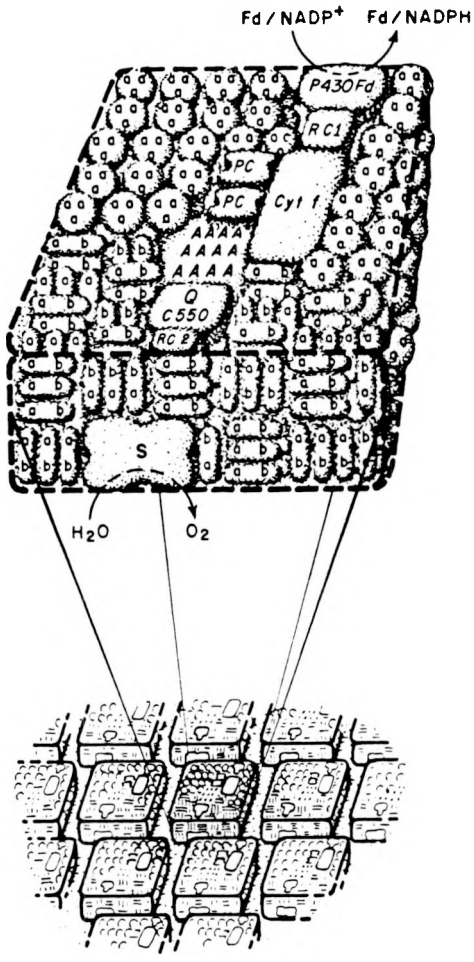

Figure 1.5 A highly schematic illustration of the pebble mosaic model. At the top is an expanded view of a single unit, consisting of an integrated array of different "pebbles": the electron transport cofactors, reaction centers and specific pigment-protein subunits.

DETECTION OF EXCITATION ENERGY TRANSFER

Fluorescence depolarization caused by excitation energy transfer provides an important tool to monitor this transfer.

When an isotropic ensemble of molecules is excited by polarized light, an anisotropic excited state distribution is generated and this polarization character is still exhibited by the emitted fluorescence of these excited molecules, which is called fluorescence polarization. When energy transfer occurs between donor and acceptor, and since it is not necessary that the acceptor have a parallel dipole orientation to the donor, the anisotropy created with polarized light on the donor will be randomized or destroyed by the excitation transport. This phenomenon is called fluorescence depolarization. Galanin[9] has shown that the overwhelming contribution to fluorescence polarization is due to fluorescence from excitations at sites which were initially excited. Thus the time dependence of the fluorescence depolarization will be related to the time-dependent probability that the excitation is at the initial site. Suppose that $G^S(t)$ is the time-dependent probability that excitation resides on the originally excited site. Then the direct relation

between the experimental observables and $G^S(t)$ given by Gochanour[10] is

$$I_{\parallel} = P(t)[1 + 0.8G^S(t)] \quad (1.13a)$$

$$I_{\perp} = P(t)[1 - 0.4G^S(t)] \quad (1.13b)$$

where $I_{\parallel}$ and $I_{\perp}$ are the fluorescence intensity polarized parallel and perpendicular to the excitation polarization, respectively; $P(t)$ is the isotropic decay function. $I_{\parallel}$ and $I_{\perp}$ could be achieved though a polarizer. $P(t)$ can be obtained by placing the collection optical polarizer at an angle such that one component of the parallely and two components of perpendicularly polarized fluorescence are collected.

$$I_{\parallel} + 2I_{\perp} = 3P(t) \quad (1.14)$$

This angle is called the "magic angle", which is 54.7°.

Eq. 1.13 is valid only when no intrinsic, rotational, or self-absorption depolarization exists. Intrinsic depolarization occurs when the absorption and emission dipoles are non-parallel. Rotational depolarization occurs when the molecule rotates on the time scale of the emission lifetime. Self-absorption occurs when the sample optical density is sufficient to permit reabsorption of sample emission. All of these imply that the experimental conditions for Eq. 1.13 should include a viscous solvent or host, linearly polarized absorption and fluorescence transition moments

along the same axis, and a weak excitation laser beam so that the orientational distribution of excited molecules is random.

The expression for $G^S(t)$ has different forms dependent on the systems studied. For a large range of concentrations of organic dye molecules in solution, two-particle theory[11] shows that $G^S(t)$ in a 3-dimensional system has the form

$$G^S(t) = \exp[-C_D(\pi t/2\tau_D)^{1/2}] \tag{1.15}$$

where C_D is the dimensionless reduced donor concentration,

$$C_D = 4/3\ \pi\ R^3\ \rho_D \tag{1.16}$$

Here, ρ_D is the donor number density. For nonrandom systems, the polarization decays in different way. For example, in the PSI-60 sample(Section III), $G^S(t)$ has the following form

$$G^S(t) = (1-a)\exp(-t/\tau) + a \tag{1.17}$$

where a is the residual anisotropy.

Pump-Probe Spectroscopy

The return of molecules to the ground state can also be followed by the change in transmission of a weak probe pulse through a sample as a function of delay time after the arrival of the strong pump pulse; this is called pump-probe spectroscopy. The transmission change (or absorption change) in pump-probe spectroscopy is proportional to the population in the first

excited state as fluorescence, if one assumes no excitation to a higher level when the probe pulse goes through the sample. Two photobleaching components $A_{\parallel}$ and $A_{\perp}$ (which stand for the polarization of probe parallel and perpendicular, respectively to the polarization of the pump) correspond to $I_{\parallel}$ and $I_{\perp}$ above (Fig. 1.6); and Eq 1.13 is still valid for $A_{\parallel}$ and $A_{\perp}$:

$$A_{\parallel} = P(t)[1 + 0.8G^{S}(t)] \qquad (1.18a)$$

$$A_{\perp} = P(t)[1 - 0.4G^{S}(t)] \qquad (1.18b)$$

since parallel absorption and emission dipoles have been assumed. The isotropic decay $P(t)$ is measured with probe beam polarization rotated 54.7° from the pump beam polarization.

Pump-probe spectroscopy has two significant advantages. The first is that a multiple modulation technique is employed in the detection system, which provides high selectivity and sensitivity in signal detection. The second is that the experimental time resolution is limited by the pump- and probe-pulse durations and not by the time resolution of the detector.

Pump-probe spectroscopy is employed to detect EET in this dissertation (Fig. 1.7) since it can monitor EET on a shorter time scale than other instruments.

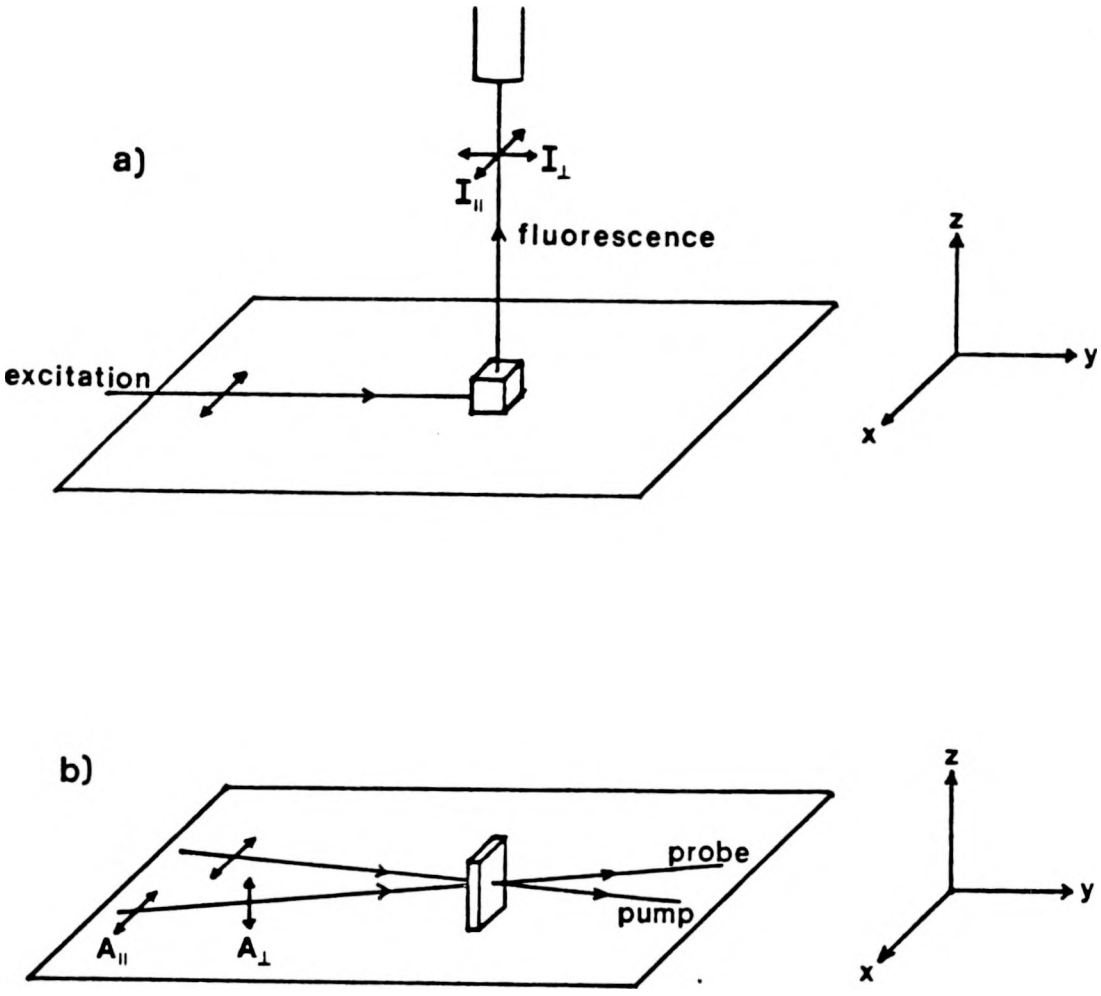

Figure 1.6 Schematic of energy transfer detected by a) fluorescence depolarization, and b) absorption depolarization. In both cases, excitation beams are linearly polarized; in a) polarized fluorescence is detected.

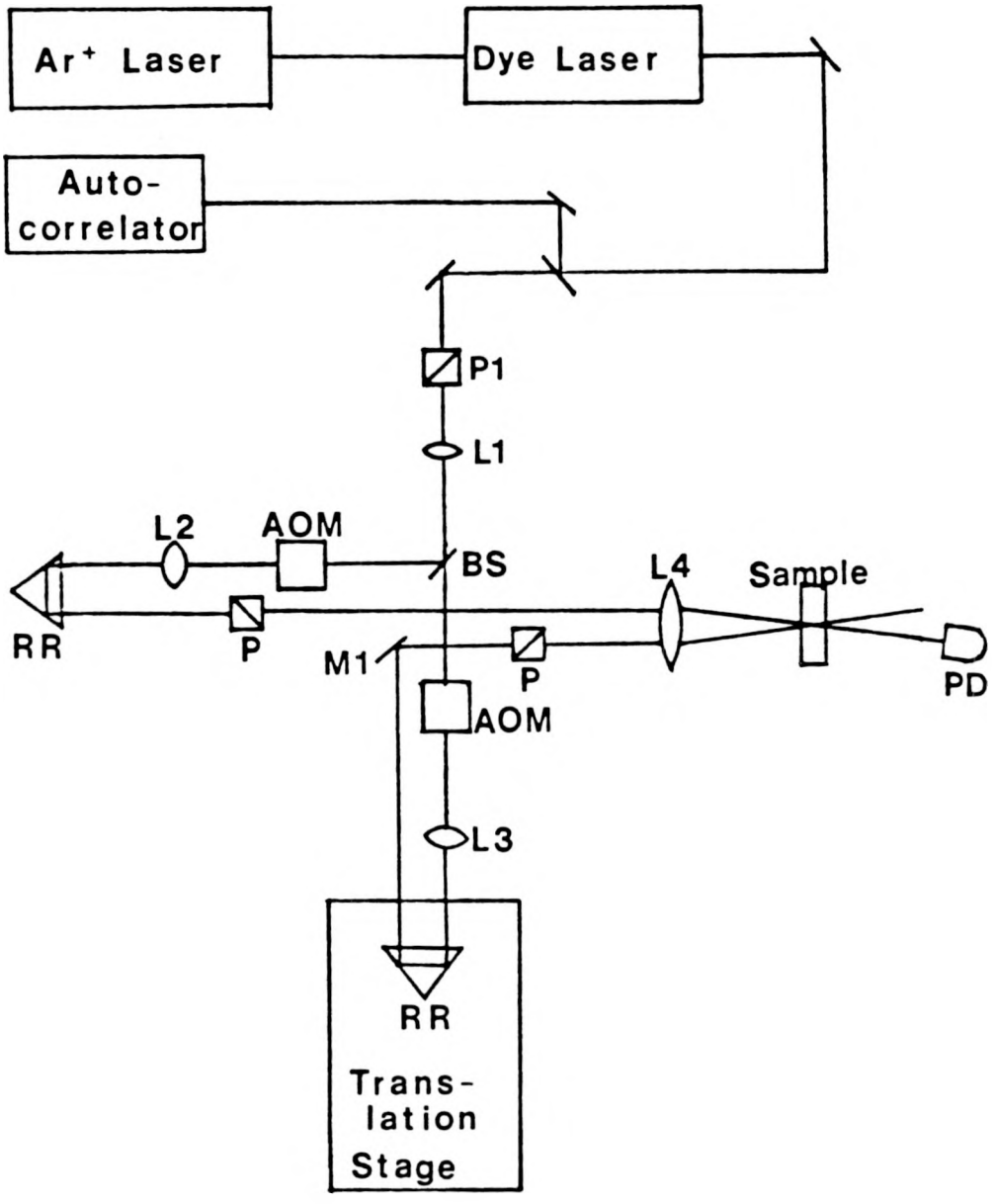

Figure 1.7 Schematic of optical arrangement for transient absorption (pump-probe) spectroscopy as used to study depolarization due to electronic energy transfer. P: polarizer; PD: photodiode; BS: beamsplitter; L: lens; AOM: acousto-optic modulator; RR: retroreflector; M: mirrow.

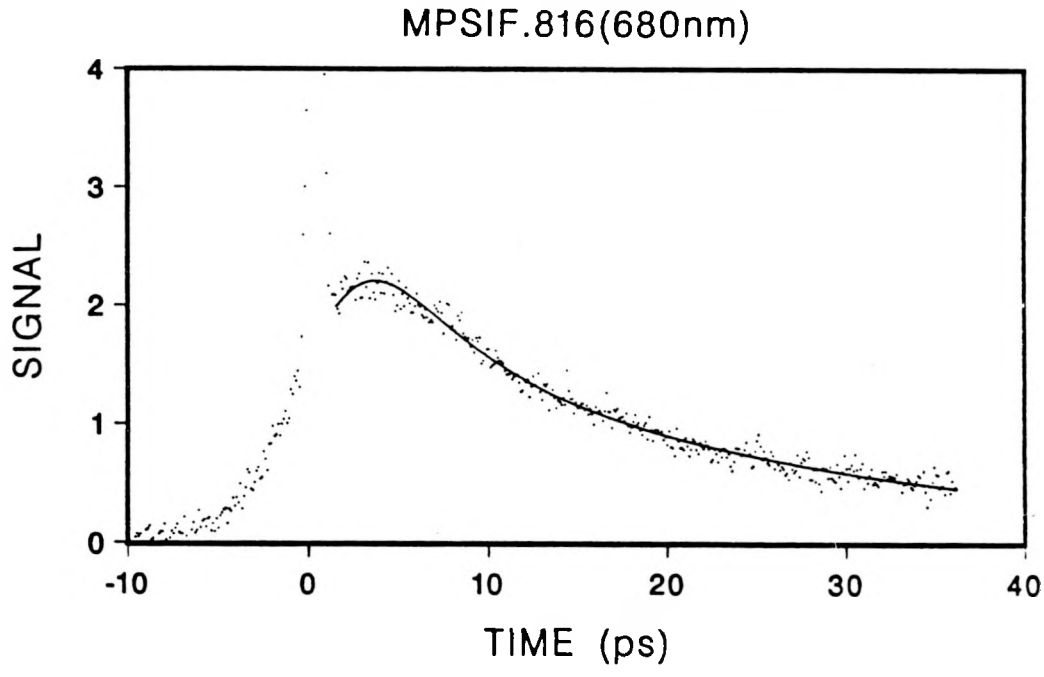

Figure 1.8 Photo-bleaching profile from Chl/P700~45 from spinach. The sharp spike at zero delay results from the coherent interaction of the identical pump and probe pulses in the sample.

EXPERIMENTAL ARTIFACTS

Some experimental artifacts may arise in pump-probe spectroscopy and two are considered here.

The first is a coherent coupling artifact. Fig. 1.8 shows a ground-state recovery trace in a pump-probe experiment. The sharp peak around zero time in Fig. 1.8 resulting from the coherent interaction of the identical pump and probe pulses in the sample is called a coherent coupling artifact or coherent spike. According to Fleming[12], the regions of constructive and destructive interference across the sample, which are caused by the pathlength differences between the identical pump and probe beams, act like a transient grating. The first-order diffraction from this grating results in each beam being diffracted into each other, and the sharp spike that then results from the diffraction of some pump photons into the probe beam direction.

Since the coherent spike is symmetric with respect to delay time, it could be eliminated by antisymmetrizing the signal intensity[13]. Assume $S(\tau)$ is the signal,

$$S(\tau) = \gamma(\tau) + \beta(\tau) + \beta'(\tau) \qquad (1.19)$$

where $\beta(\tau)$ and $\beta'(\tau)$ are the coherent-coupling artifact and grating term respectively, and $\gamma(\tau)$ is the convolution of the

system response ($R^i(t)$, incoherent response) with the autocorelation of the pulse($G(t-\tau)$),

$$\gamma(\tau) = \int G(t-\tau)R^i(t)\ dt \tag{1.20}$$

The antisymmetrized form of the signal does not contain the coherent spike,

$$\begin{aligned} S_a &= 1/2\ [S(\tau) - S(-\tau)] = 1/2\ [\gamma(\tau) - \gamma(-\tau)] \\ &= 1/2\ [\int G(t-\tau)R^i(t)\ dt - \int G(t-\tau)R^i(-t)\ dt] \\ &= \int G(t-\tau)R_a^i(t)\ dt \end{aligned} \tag{1.21}$$

$$R_a^i(t) = 1/2\ [R^i(t) - R^i(-t)] \tag{1.22}$$

$R_a^i(t)$ is the antisymmetrized form of the response function and could be found by deconvolution of Eq. 1.21. The full response function can then be obtained from

$$R^i(t) = 2\theta(t)R_a^i(t) \tag{1.23}$$

where $\theta(t)$ is a step function.

The second artifact is excitation annihilation which usually occurs in pump-probe experiments on photosynthetic systems, where anomalously low yields and short lifetimes were observed upon the use of intense short laser pulses. As we know, a lot of excitations could be simultaneously present in one domain when intense laser pulse are used. If two excited molecules are close together, one could transfer its energy to the other and return to the ground state while the other is promoted to a higher

excited state due to the dipolar interaction. This higher excited state can revert again to the lowest excited state via a rapid internal conversion. The net result of this process is the loss of one excitation. Eq. 1.19 and 1.20 show the singlet-singlet and singlet-triplet annihilations respectively.

$$(B)Chl^{*} + (B)Chl^{*} \rightarrow (B)Chl^{*} + (B)Chl \qquad (1.19)$$

$$Car^{T} + (B)Chl^{*} \rightarrow Car^{T} + (B)Chl \qquad (1.20a)$$

$$(B)Chl^{T} + (B)Chl^{*} \rightarrow (B)Chl^{T} + (B)Chl \qquad (1.20b)$$

The avoidance of excitation annihilation is achieved in practice by using a lower energy laser pulse.

REFERENCES

1. Kasha, M. Radiat. Res. 1963, 20, 55-70.

2. Förster, Th. In "Modern Quantum Chemistry, Part IIIB: Light and Organic Crystals"; Sinanoglu, O., Ed.; Academic Press: New York, 1965; P. 93.

3. Knox, R. S. In "Bioenergetics of Photosynthesis"; Govindjee, Ed.; Academic Press: New York, 1975; P. 189.

4. Knox, R. S. In "Primary Processes of Photosynthesis"; Barber, J., Ed.; Elsevier: Amsterdam, 1977; Vol. 2, P. 73.

5. Pearlstein, R. M., In "Photosynthesis - Energy Conversion by Plants and Bacteria"; Govindjee, Ed.; Academic Press, New York, 1982; Vol. 1, P. 293.

6. Dexter, D. L., J. Chem. Phys. 1953, 21, 836-850.

7. Rabinowitch, E., Govindjee "Photosynthesis"; John Wiley & Sons, INC. New York, 1969; P. 160.

8. Sauer, K., In "Bioenergetics of Photosynthesis"; Govindjeer, Ed.; Academic Press, New York, 1975; P. 115.

9. Galanin, M. D., Tr. Fiz. Inst. Akad. Nauk USSR 1950, 5, 339.

10. Gochanour, C. R., Fayer, M. D., Chem. Phys. 1981, 85, 1989.

11. Huber, D. L., Hamilton, D. S., Barnett, B., Phys. Rev. B. 1977, 16, 4642.

12. Fleming, G. R., "Chemical Applications of Ultrafast Spectroscopy"; Oxford University Press, New York, 1986; P. 74.

13. Engh, R. A., Petrich, J. W., Fleming, G. R., J. Phys. Chem. 1985, 89, 618.

SECTION II. POLARIZED PUMP-PROBE SPECTROSCOPY OF EXCITON TRANSPORT IN BACTERIOCHLOROPHYLL A-PROTIEN FROM PROSTHECOCHLORIS AESTUARII

POLARIZED PUMP-PROBE SPECTROSCOPY OF EXCITON TRANSPORT IN BACTERIOCHLOROPHYLL A-PROTEIN FROM PROSTHECOCHLORIS AESTUARII

Shumei Yang, Timothy P. Causgrove, and Walter S. Struve

Department of Chemistry and Ames Laboratory-USDOE

Iowa State University, Ames, Iowa 50011

INTRODUCTION

Electronic excitation transport (EET) is the first process which occurs after light absorption by antenna pigments in green photosynthetic bacteria and plants. The excitation migration is believed to proceed by an incoherent random-walk mechanism [1] arising from Förster dipole-dipole coupling [2] between molecules or aggregates containing antenna chromophores. The antenna chlorophylls in plants are complexed with proteins in units containing six or more chromophores. In Sauer's "pebble mosaic" model, the chlorophylls within such units are strongly coupled, and electronic excitation exists as exciton states which are delocalized over the clusters [3]. Chromophores belonging to different units are weakly coupled, and EET between clusters is presumed to occur by ordinary Förster hopping.

Few time-domain experiments have directly resolved the antenna EET processes in green photosynthetic organisms. Owens et al. [4] recently measured the reaction center quenching of antenna fluorescence lifetimes in photosystem I core antennae of P700 Chl a-protein complexes from barley, and in a photosynthetic mutant of Chlamydomonas reinhardtii without the photosystem II antenna/reaction center complex. The fluorescence lifetime varied linearly with core antenna size in both cases, in

accordance with random walk models [5,6] in which the chlorophylls are assumed to occupy the sites of a regular lattice. Analysis of the fluorescence profiles in terms of the lattice models yielded a calculated single-step EET time of between 0.1 and 0.2 ps in the core antenna of photosystem I. Excitation migration was found to be nearly diffusive, with photoconversion in the reaction center occurring on the average of once per 2.4 excitation hops from the core antenna.

In our EET program, systems excited with linearly polarized laser pulses have been studied by analyzing the time-dependent fluorescence profiles $I_{\parallel}(t)$, $I_{\perp}(t)$ polarized parallel and perpendicular to the laser polarization [7,8]. Unlike reaction center trapping of antenna fluorescence, this technique's sensitivity is specific to fluorescence depolarization attending single excitation hops from the laser-excited chromophore. However, the instrument function of ~45 ps FWHM [8] in our current time-correlated single photon counting apparatus is far too slow for direct characterization of single-step EET in green photosynthetic antennae. We have therefore resorted to polarized pump-probe spectroscopy. The relationships between the polarized optical density components $A_{\parallel}(t)$, $A_{\perp}(t)$ and time-resolved observables in EET are analogous to those for fluorescence intensity components, but the time resolution is laser pulse-

limited. In separate experiments [9], we probed EET in glycerol solutions of rhodamine 640 at concentrations between 3.4 μM and 1.4 mM, using both time-correlated single photon counting (to evaluate $I_{\parallel}(t)$ and $I_{\perp}(t)$) and pump-probe techniques (which yielded $A_{\parallel}(t)$ and $A_{\perp}(t)$). The transport was found to be well described by a two-particle theory [10] for the time-dependent probability that the excitation resides on the laser-pumped molecule. Optimized Förster parameters from nonlinear least-squares fits of the two-particle theory to the polarized profiles from both photon counting and pump-probe experiments proved to be congruent to within data scatter, ensuring that our pump-probe techniques furnish a valid test of transport in this prototype system.

For our initial study of EET in photosynthetic antennae, we elected the bacteriochlorophyll (BChl) a-protein from the green sulfur bacterium Prosthecochloris aestuarii -- the only bacterial antenna system whose 3-dimensional structure is known [11]. Photon absorption in such bacteria occurs in the chlorobium chlorophyll system, which comprises some 10^3 BChl c, d, or e molecules per reaction center. Excitation is channeled to a BChl a-protein complex containing ~10^2 chromophores, which in turn funnels the excitation to the reaction center. The basic structural unit in BChl a-protein is a trimer of subunits

containing 7 BChl a molecules each. The nearest-neighbor Mg-Mg separations for BChl a chromophores within a subunit range from 11.3 to 14.4 [11]. The BChl a-protein crystallizes in either the $P6_3$ (hexagonal) or $P6_1$ (trigonal) space group [12]; there are no Mg-Mg separations shorter than 24 (30) for chromophores in different subunits in crystals of $P6_3$ ($P6_1$) symmetry [11]. (Tronrud et al. [13] have recently refined the x-ray structure of the BChl a-protein; they concentrated on the protein sequence and BChl a conformations, and did not report the chromophore orientations or positions). Hence, BChl a-protein from P. aestuarii presents a possible realization of the "pebble mosaic" model, in which EET (whose rate scales as R^{-6} for chromophores separated by R) is expected to be far more rapid within subunits than among subunits. Absorption and circular dichroism spectra of the BChl a-protein in a triglycerophosphate buffer show strong evidence for exciton interactions in both the Q_y absorption system at 809 nm and in the Q_x system at 603 nm [14]. The observed splittings in the Q_y system are comparable to off-diagonal resonance dipole interaction energies (up to ~250 cm^{-1}) calculated [15] by a transition monopole method [16]. However, attempts to simulate the absorption and CD spectra based on the known BChl a-protein geometry have not been successful.

In this work, we have performed pump-probe experiments on the BChl *a*-protein Q_x band system at wavelengths between 598 and 609 nm. The long-time behavior of $A_{\parallel}(t)$ and $A_{\perp}(t)$ varies with probe wavelength and is related to the projection of the probed transition moment along the crystal *c*-axis. The time-resolved data are analyzed using a kinetic model derived from the geometry of the BChl *a*-protein.

EXPERIMENTAL

The BChl a-protein solution in triglycerophosphate buffer [14,17] was generously provided by R. E. Fenna[11]. For most experiments, it was concentrated to ~5.0 optical density for 1 cm path length at 809 nm; its room temperature absorption spectrum between 590 and 840 nm matched published spectra [17,18]. Such solutions contain BChl a-protein crystallites with a mean particle size of at least 30 trimers [19]. Samples were housed between $\lambda/4$ fused silica flats separated by a 800 μm teflon spacer; they were rotated at 12 Hz to minimize photooxidation by the laser beams during pump-probe scans.

A multiline argon ion laser with 6 W plasma tube pumped a passively mode-locked dual-jet rhodamine 590-DQOCI laser [20] to produce vertically polarized pulses between 598 and 609 nm with ~50 mW average power at 125 MHz repetition rate. Real-time autocorrelation traces [21] exhibited ~1.5 ps FWHM. The output beam was divided into pump and probe beams, which were modulated at 5.0 and 0.5 MHz respectively with ~80% modulation depth using Isomet 1206C acoustooptic modulators. The variably delayed pump beam was reflected by a BK-7 corner cube prism mounted on a Micro-Controle UT10050PP translation stage (0.1 μm/step, 5 cm range). The beam polarizations were selected using identical

calcite Glan-Thompson polarizers; the probe polarization was fixed at 45° from the laser polarization, and the pump polarization was varied. A 7.3 cm f. l. lens focussed both beams to ~20 μm diameter in the rotating sample. The average incident power was <5 mW in each beam. The transmitted probe beam was collected by an EG&G FOD-100 photodiode, and phase-locked single-sideband detection was achieved at 5.5 MHz using a modified Drake R-7A radio receiver [22]. The receiver's signal-bearing 50 kHz intermediate frequency (IF) was tapped and routed to a Stanford Research Systems SR510 lock-in amplifier (LIA) and was demodulated using the receiver reference IF output. Data were transmitted during pump-probe sweeps from the LIA via an RS-232 port to a DEC MINC-23 computer operating in a TSX-Plus multiuser environment. Pump-probe scans were normalized to the instantaneous square of the laser intensity by deflecting part of the laser beam into another FOD-100 photodiode, processing the signal in a current-to-voltage converter and RC filter, and transmitting the digitized signal through the LIA RS-232 port to the computer.

RESULTS AND DISCUSSION

A typical pump-probe profile obtained at 603 nm (the Q_x band maximum) with the probe polarization rotated 54.7° from the pump polarization is shown in Fig. 2.1. The observed decay, which corresponds to ground state repopulation in the BChl *a*-protein, is highly nonexponential; it is well described by the biexponential law P(t) = 0.41exp(-t/14.6 ps) + 0.59exp(-t/52.4 ps). These time constants are some two orders of magnitude shorter than intrinsic Q_y lifetimes of BChl *a* chromophores [23]. The isotropic decay obtained with the average power halved in both beams is very similar (P(t) = 0.43exp(-t/17.0 ps) + 0.57exp(-t/68.6 ps)). The rapid decay is therefore not primarily a consequence of exciton annihilation, which would be important if far more intense laser pulses were used; typical pulse energies were ~0.05 nJ at 603 nm.

In Fig. 2.2, we show the polarized pump-probe transients $A_{\parallel}(t)$ and $A_{\perp}(t)$ at 603 nm and at 598 nm. They are dominated by coherent coupling artifacts [24] during the first ~1.5 ps. These can be removed in principle by data antisymmetrization [25]; this procedure is useful only for data with higher S/N, which is limited here by the available concentrations of BChl *a*-protein.

The transients were fitted instead with convolutions of the laser autocorrelation function with the phenomenological expressions

$$A_{\parallel}(t) = P(t)\{1 + 0.8[(1-a)\exp(-t/\tau) + a]\}$$
$$A_{\perp}(t) = P(t)\{1 - 0.4[(1-a)\exp(-t/\tau) + a]\} \quad (2.1)$$

beginning with the data channel corresponding to 2.5 ps past the coherent coupling peak. The isotropic decay function $P(t)$ was expressed as a biexponential function with parameters fixed at values obtained by fitting isotropic decays analogous to that shown in Figure 2.1. The polarized profiles $A_{\parallel}(t)$ and $A_{\perp}(t)$ were fitted simultaneously in a linked deconvolution procedure [26] which minimized the combined sum of residuals for both profiles with respect to the parameters $\underline{a}$ and τ. The results of such analyses are given for several pump-probe experiments at 609, 603, and 598 nm in Table 2.1. Nonzero values of the parameter $\underline{a}$ are required to simulate the polarized photobleaching decays at 609 and 603 nm: analyses of pump-probe scans obtained over 125 ps windows (not shown in Fig. 2.2) confirm that $A_{\parallel}(t)/A_{\perp}(t)$ does not approach unity at long times, and they yield fitting parameters similar to those derived from the shorter scans, which were limited to 25 ps windows.

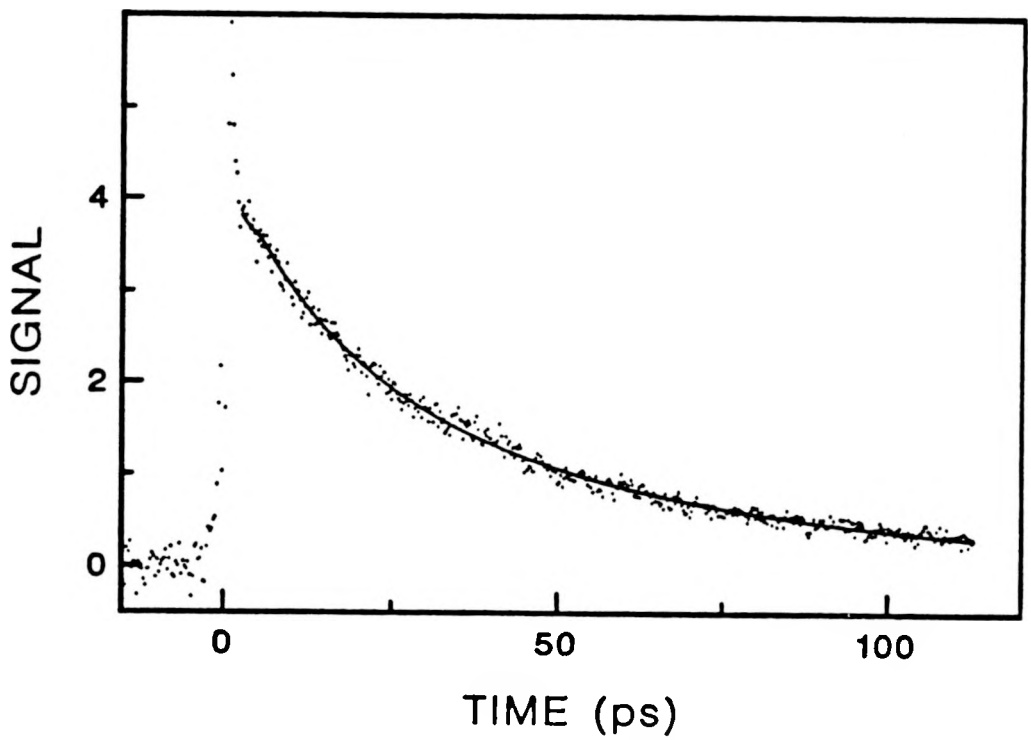

Figure 2.1 Photobleaching transient of triglycerophosphate buffer solution of BChl a-protein from P. aestuarii, obtained using 603 nm pump and probe polarizations 54.7° apart. Continuous curve gives convolution of laser autocorrelation function with biexponential decay law $P(t) = 0.41\exp(-t/14.6ps) + 0.59\exp(-t/52.4ps)$.

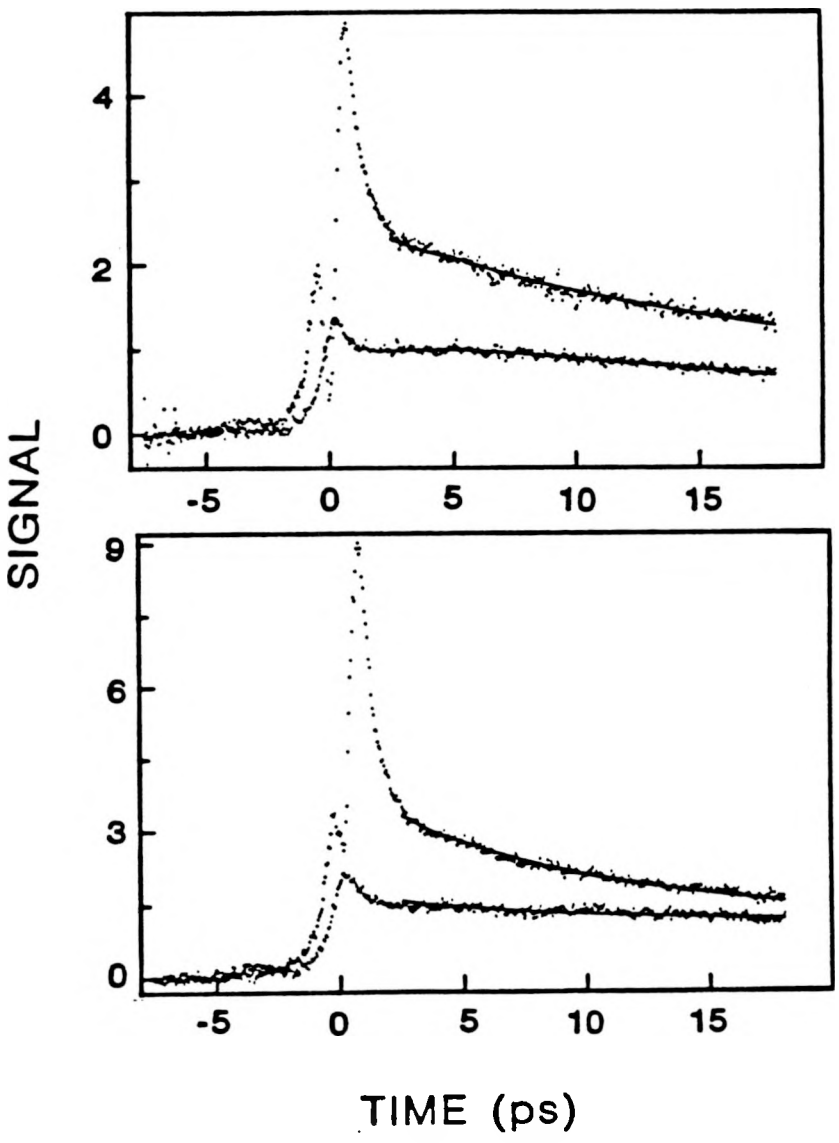

Figure 2.2 Polarized pump-probe transients for BChl a-protein at 603 nm (upper panel) and at 598 nm (lower panel). In each panel the upper and lower traces correspond to $A_{\parallel}(t)$ and $A_{\perp}(t)$, respectively. Continuous curves show convolutions of laser autocorrelation function with Eqs. 6.1, with lifetime and anisotropy parameters optimized as described in text. Note the slower depolarization timescale at 598 nm.

To model the depolarization due to EET in BChl a-protein, we consider the $P6_3$ crystal structure shown in Fig. 2.3. The unit cell contains two trimers [11,13] which are labelled ABC and DEF. Trimer ABC is located in an ab-plane which is displaced by 49.3 Å along the c-axis from the plane occupied by trimers DEF, GIJ, and HKL. Because spectroscopic evidence supports the existence of strong exciton interactions between BChl a chromophores inside a subunit [14,15], our model presumes that Förster excitation hopping occurs between exciton states which are delocalized over tightly coupled groups of seven BChl a molecules. Creation of an exciton state in subunit A may be followed by migration to exciton states centered on other subunits. We arbitrarily restrict EET to hopping between neighboring subunits, and we distinguish two kinds of contiguous subunit pairs. The first kind

Table 2.1 Fitting parameters for polarized pump-probe profiles in BChl a-protein from P. aestuarii

Wavelength, nm	Scan duration, ps	a	τ, ps
609	125	0.497	3.48
609	125	0.485	1.47
603	25	0.530	3.50
603	25	0.435	5.65
603	25	0.468	4.74
603	25	0.422	5.12
603	125	0.467	9.44
603	125	0.537	5.28
598	25	0.0[a]	20.9
598	25	0.0[a]	18.3
598	125	0.034	32.9

[a]Parameter held fixed at 0.0.

is an adjacent pair of subunits within the same trimer, typified by A-B or D-E. The second kind is a pair of neighboring subunits belonging to different trimers, such as A-D or B-H. The Förster hopping rate between subunits i and j will scale approximately as

$$w_{ij} = R_{ij}^{-6}\kappa_{ij}^{2} \tag{2.2}$$

where R_{ij} is the separation between subunits. The orientational factor κ_{ij} is given in terms of the transition moment orientations $\hat{d}_i$, $\hat{d}_j$ in the lowest-energy exciton component of the Q_y state by

$$\kappa_{ij} = \hat{d}_i \cdot \hat{d}_j - 3(\hat{d}_i \cdot \hat{R}_{ij})(\hat{d}_j \cdot \hat{R}_{ij}) \tag{2.3}$$

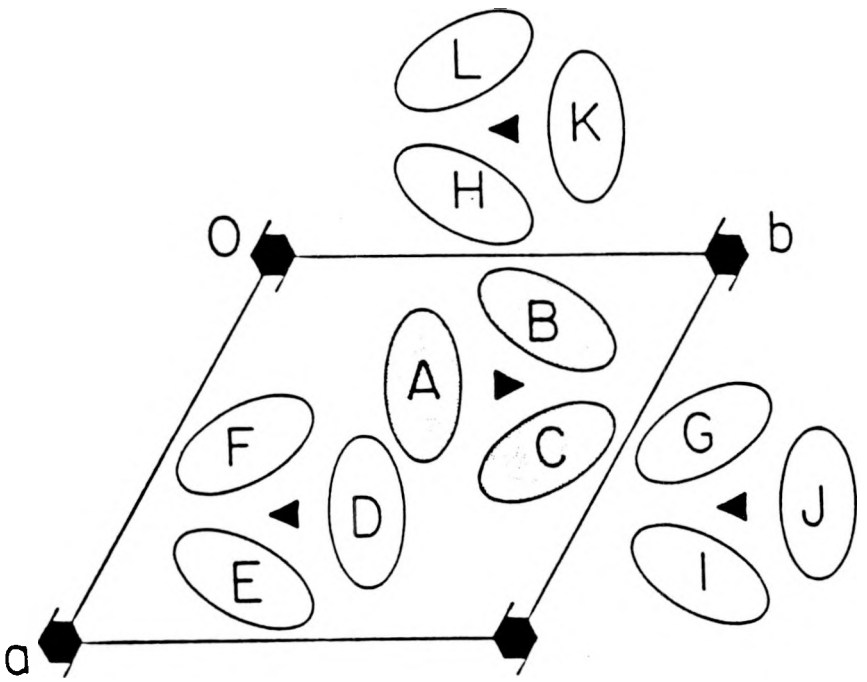

Figure 2.3 Schematic diagram of $P6_3$ (hexagonal) unit cell of BChl a-protein from P. aestuarii. Unit cell dimensions are a = b = 111.9 Å, c = 98.6 Å[11]. Trimers ABC and DEF are separated by 49.3 Å along the c-axis.

If a subunit centroid is defined as the mean Mg atom position inside that subunit, and if one associates R_{ij} with the separation between centroids of subunits $\underline{i}$ and $\underline{j}$, the distances R_{AB} and R_{AD} pertinent to the first and second kinds of hopping are 33.1 and 61.5 Å, respectively. Equation 2.2 then implies that the relative transition rates will be given by $w_{AD}/w_{AB} \sim 0.024\ \kappa_{AD}^2/\kappa_{AB}^2$. Owing to the crystal symmetry, the orientational factors can be compactly expressed in terms of the transition moment orientation $\hat{d}_A = (\rho, \sigma, \upsilon) \equiv (\rho, \sigma, \sqrt{1-\rho^2-\sigma^2})$ (where ρ, σ, υ are unit vectors) in subunit A; they are

$$\kappa_{AB} = 1 - \frac{9}{4}\rho^2 + \frac{3}{4}\sigma^2 \tag{2.4}$$

$$\kappa_{AD} = \frac{3}{4}\rho^2 + \frac{1}{4}\sigma^2 - \rho\sigma\varsigma 3/2 - 1 \tag{2.5}$$

The ratio $\kappa_{AD}^2/\kappa_{AB}^2$ is a slowly varying function of the (unknown) transition moment components ρ, σ in the ab-plane for most $\rho^2 + \sigma^2 < 1$; typical values range between 0.0 and 2.0. The function $\kappa_{AD}^2/\kappa_{AB}^2$ is singular at special combinations of ρ and σ where κ_{AB} vanishes (e.g., $\rho \sim 0.7$ and $\sigma \sim 0.3$, Eq. 6.4). The ratio w_{AD}/w_{AB} of intertrimer to intratrimer hopping will consequently be small for most orientations $\hat{d}_A$; it only becomes large for the singular orientations corresponding to very slow hopping rates w_{AB} between subunits in the same trimer. The qualitative migration patterns for $w_{AD}/w_{AB} \gg 1$ and $w_{AD}/w_{AB} \ll 1$ are illustrated in Fig. 2.4.

Prior to modelling EET for general w_{AD}/w_{AB}, we treat the limiting case where $w_{AD}/w_{AB} << 1$ (cf., Fig. 2.4b). The depolarization at early times following excitation of subunit A will then be dominated by hopping among subunits A, B, and C; negligible exciton populations will be found in subunits D through L. The time-dependent probabilities A(t), B(t), C(t) of finding excitation in subunits A, B, C are then given by solutions to the kinetic equation

$$-\frac{dA}{dt} = w_{AB}(2A - B - C) \tag{2.6}$$

under the initial conditions

$$A(0) = A_0 \tag{2.7}$$

$$B(0) = C(0) = 0 \tag{2.8}$$

The solutions are

$$A(t) = A_0[1 + 2\exp(-3w_{AB}t)]/3 \tag{2.9}$$

$$B(t) = C(t) = A_0[1 - \exp(-3w_{AB}t)]/3 \tag{2.10}$$

We next consider an idealized pump-probe experiment in which subunit A is excited in a trimer having the specific orientation shown in Fig. 2.5. The pump pulse is polarized along the laboratory-fixed x-axis, and pulses which probe $A_{\parallel}(t)$ and $A_{\perp}(t)$ are polarized along the x- and y-axes respectively. The trimer ab-plane is parallel to the xy-plane.

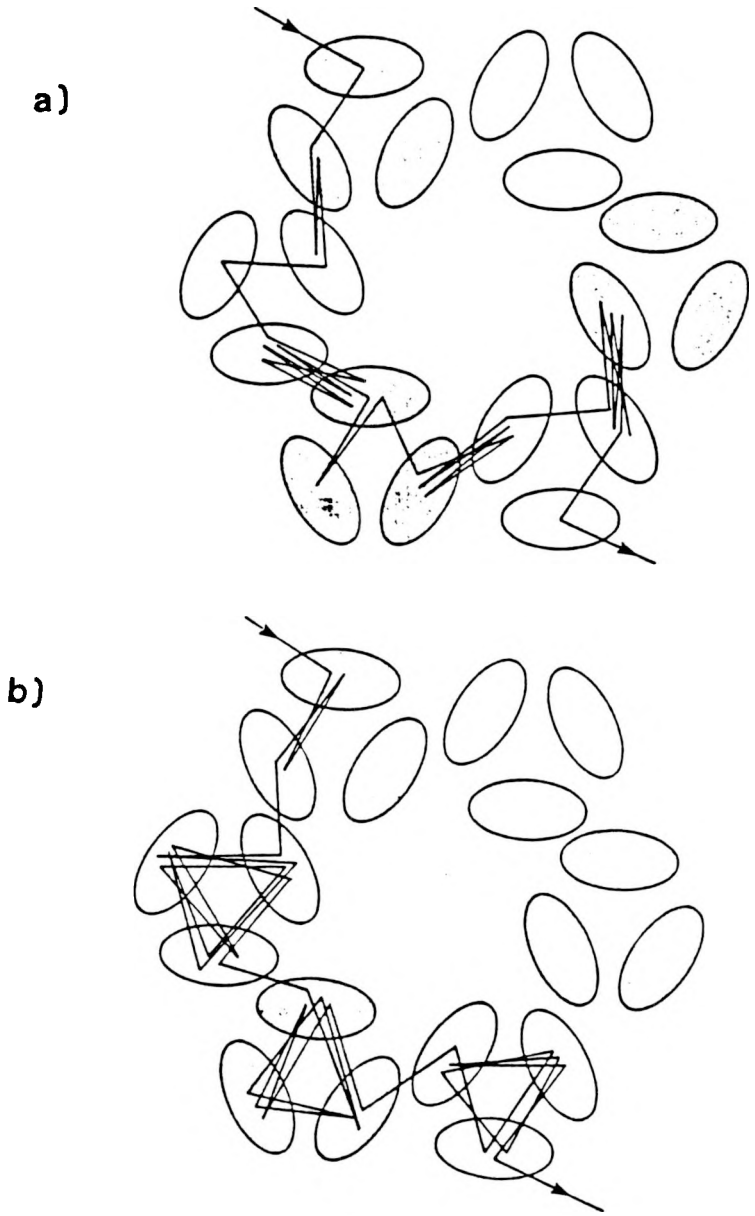

Figure 2.4 Excitation migration patterns for a) $w_{AD} >> w_{AB}$ and b) $w_{AD} << w_{AB}$.

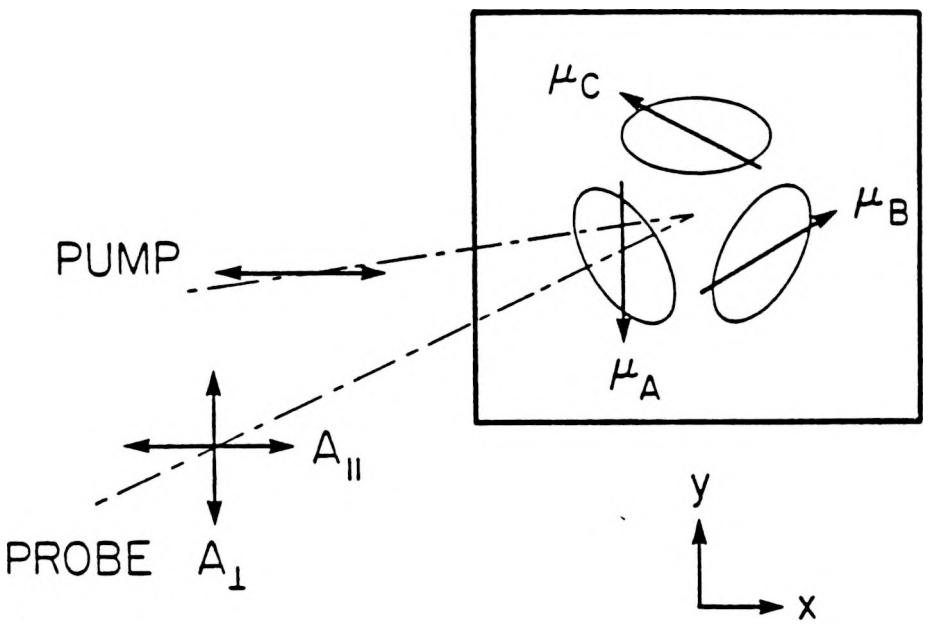

Figure 2.5 Pump-probe beam geometry and exciton transition moment orientations used in derivation of Eqs. 6.11 through 6.13.

The exciton transition moment for subunit A at the probe wavelength has components $\mu^{\circ}_{Ax} = \alpha$, $\mu^{\circ}_{Ay} = \beta$, $\mu^{\circ}_{Az} = \gamma$; these components are normalized so that $\alpha^2 + \beta^2 + \gamma^2 = 1$. By symmetry, the transition moments for the same exciton transition in subunits B and C are

$$\mu^{\circ}_{Bx} = -\alpha/2 - \beta\sqrt{3}/2 \tag{2.11a}$$

$$\mu^{\circ}_{By} = \alpha\sqrt{3}/2 - \beta/2 \tag{2.11b}$$

$$\mu^{\circ}_{Bz} = \gamma \tag{2.11c}$$

$$\mu^{\circ}_{Cx} = -\alpha/2 + \beta\sqrt{3}/2 \tag{2.11d}$$

$$\mu^{\circ}_{Cy} = -\alpha\sqrt{3}/2 - \beta/2 \tag{2.11e}$$

$$\mu^{\circ}_{Cz} = \gamma \tag{2.11f}$$

For a trimer whose orientation is displaced from that in Fig. 2.5 by arbitrary Euler angles ϕ, θ, χ, the transition moments in the laboratory system may be expressed using the pertinent rotation matrix $\underline{\underline{\lambda}}$ [27],

$$\begin{aligned} \underset{\sim}{\mu}_A &= \underline{\underline{\lambda}} \bullet \underset{\sim}{\mu}^{\circ}_A \\ \underset{\sim}{\mu}_B &= \underline{\underline{\lambda}} \bullet \underset{\sim}{\mu}^{\circ}_B \\ \underset{\sim}{\mu}_C &= \underline{\underline{\lambda}} \bullet \underset{\sim}{\mu}^{\circ}_C \end{aligned} \tag{2.12}$$

Rotational averaging over the random BChl a-protein crystallite orientations in the solution then yields

$$A_{\parallel}(t) = P(t)[\langle\mu_{Ax}^4\rangle A(t) + \langle\mu_{Ax}^2\mu_{Bx}^2 + \mu_{Ax}^2\mu_{Cx}^2\rangle B(t)]$$

$$A_{\perp}(t) = P(t)[\langle\mu_{Ax}^2\mu_{Ay}^2\rangle A(t) + \langle\mu_{Ax}^2\mu_{By}^2 + \mu_{Ax}^2\mu_{Cy}^2\rangle B(t)] \quad (2.13)$$

Substitution of Eqs. 6.9-6.12 into Eqs. 6.13 then leads to expressions for $A_{\parallel}(t)$, $A_{\perp}(t)$ which are identical to the phenomenological Eqs. 6.1 if one makes the associations

$$\tau = 1/3w_{AB} \quad (2.14)$$

and

$$a = (3\gamma^2 - 1)^2/4 \quad (2.15)$$

According to this model, the observed depolarization lifetime τ is shorter than the exciton hopping time w_{AB}^{-1} by a factor of three. The form of the residual anisotropy parameter a, which depends on the projection γ of the exciton moment along the trimer symmetry axis, is reminiscent of intrinsic fluorescence depolarization observed in solutions of molecules in which the fluorescence transition moment is inclined at an angle $\cos^{-1}\gamma$ from the absorption moment [28].

Extension of this kinetic model to general w_{AB}/w_{AD} requires ad hoc assumptions about the crystal boundaries. To test the effects of crystal size on the calculated absorption transients, we compared the EET simulated in $P6_3$ crystallites containing 7

trimers and 27 trimers. In the first type of calculation, excitation in the initially excited subunit A was allowed to migrate to subunits in the six trimers adjacent to trimer ABC. (These six trimers coincide with trimers DEF, GIJ, and HKL in the projection of Fig. 2.3, and they occupy ab-planes located 49.3 Å above and 49.3 Å below the plane of trimer ABC.) Only six of the 21 subunit exciton populations in this 7-trimer calculation are independent by symmetry. Their Laplace transforms a(s) through i(s) obey

$$(2w_{AB} + 2w_{AD} + s)a(s) - 2w_{AB}b(s) - 2w_{AD}d(s) = A_0 \qquad (2.16a)$$

$$-w_{AB}a(s) + (w_{AB} + 2w_{AD} + s)b(s) - 2w_{AD}g(s) = 0 \qquad (2.16b)$$

$$-w_{AD}a(s) + (2w_{AB} + w_{AD} + s)d(s) - 2w_{AB}e(s) = 0 \qquad (2.16c)$$

$$-w_{AB}d(s) + (w_{AB} + s)e(s) = 0 \qquad (2.16d)$$

$$-w_{AD}b(s) + (2w_{AB} + w_{AD} + s)g(s) - 2w_{AB}i(s) = 0 \qquad (2.16e)$$

$$-w_{AB}g(s) + (w_{AB} + s)i(s) = 0 \qquad (2.16f)$$

The seven determinants required for computation of the six Laplace transforms were evaluated numerically, and the inverse transforms A(t) through I(t) were obtained using the Stehfest algorithm [29]. Using equations for the 7-trimer system analogous to Eqs. 6.11 and 6.13, the polarized absorption transients $A_{\parallel}(t)$ and $A_{\perp}(t)$ were computed for given hopping rates w_{AB}, w_{AD} and probed exciton moment projection γ along the c-axis. In the 27-trimer calculation, the kinetic model included three

trimers coinciding with ABC in the projection of Fig. 2.3, located at c=0 and ±98.6 Å; the two trimers superimposed on each of DEF, GIJ, and HKL and located at c = ±49.3 Å; and 18 peripheral trimers having subunits whose ab-projections are contiguous to those of subunits E, F, I, J, K, and L, located at c = 0 and ±98.6 Å. The anisotropy functions $r(t) = 2.5(A_{\parallel} - A_{\perp})/(A_{\parallel} + 2A_{\perp})$ yielded by 7-trimer and 27-trimer calculations are compared for several combinations of w_{AB} and w_{AD} in Fig. 2.6. The 7-trimer and 27-trimer calculations produce virtually identical results for large w_{AB}/w_{AD}, e.g., for w_{AB}/w_{AD} = 3 in the top plot in Fig. 2.6. The effect of finite crystal size becomes apparent when intertrimer EET becomes more rapid than intratrimer transport, as shown for w_{AB}/w_{AD} = 1/3 in the bottom plot of Fig. 2.6. In the limit where $w_{AB}/w_{AD} >> 1$, the depolarization dynamics are controlled by the first few migration steps, and are relatively insensitive to details of EET on the periphery. The anisotropy function in this limit approaches the single-exponential form $r(t) = (1-\underline{a})\exp(-t/\tau)+\underline{a}$, with the parameters τ and $\underline{a}$ given by Eqs. 6.14 and 6.15. The opposite limit w_{AB}/w_{AD} = 0 is a somewhat artificial case (κ_{AB} = 0) in which the excitation equilibrates between two parallel stacks of subunits whose projections coincide with A and D in Fig. 2.3. The anisotropy decay here becomes single-exponential in a 7-

trimer calculation with lifetime $\tau = (3w_{AD})^{-1}$, and biexponential with lifetimes $(1.38w_{AD})^{-1}$ and $(3.62w_{AD})^{-1}$ in a 27-trimer calculation. For general combinations of w_{AB}, w_{AD} the anisotropy decay is nonexponential, with $r(\infty) = \underline{a}$ given by Eq. 6.15.

Most of the pump-probe profiles were obtained at 603 nm, the peak absorption wavelength in the room-temperature Q_x system. The 603 nm depolarization times τ obtained by fitting $A_{\parallel}$, $A_{\perp}$ with convolutions of Eqs. 6.1 with the laser autocorrelation function are distributed about a 4.78 ps mean with 0.76 ps standard deviation. We plot in Fig. 2.7 the anisotropy functions r(t) yielded by 27-trimer calculations for (a) $w_{AB} \neq 0$, $w_{AD} = 0$, (b) $w_{AB} = 3w_{AD}$, (c) $w_{AB} = w_{AD}$, and (d) $w_{AB} = w_{AD}/3$. The c-component γ of the probed exciton transition moment was fixed at 0.9, corresponding to a residual anisotropy parameter $\underline{a} = 0.511$ similar to the 603 nm experimental values (Table 2.1). In each case, the values of w_{AB} and w_{AD} (Table 2.2) were scaled to render the 1/e decay time in r(t) equal to 4.78 ps. The 4.78 ps single-exponential decay time in case (a) corresponds to the hopping rates $w_{AB} = 1/3\tau = (14.3\ \text{ps})^{-1}$ and $w_{AD} = 0$. While the anisotropy decays in cases (b) and (c), $w_{AB} = 3w_{AD}$ and $w_{AB} = w_{AD}$, are (strictly speaking) nonexponential, they are nearly indistinguishable from the single-exponential decay in case (a). Hence, Figure 2.7 emphasizes that the observed decay will be

essentially single-exponential in our model for $w_{AB}/w_{AD} \geq 1$, and that a continuum of combinations of the hopping rates can account for the observed decay. Discernible nonexponentiality sets in for $w_{AB}/w_{AD} = 1/3$ (case (d)) in Fig. 2.7, but the displayed differences between this and the near-exponential

Table 2.2 Förster transition rates from 27-trimer simulation of EET in BChl a-protein from P. aestuarii

Case	w_{AB}/w_{AD}	w_{AB}^{-1}, ps	w_{AD}^{-1}, ps	$w_{AB} + w_A$, ps^{-1}
a	∞	14.3	∞	0.070
b	3	20.2	60.7	0.066
c	1	28.5	28.5	0.070
d	1/3	66.0	22.0	0.061

cases are too small for detection under current S/N in polarized pump-probe experiments. In summary, our 603 nm data establish a well-defined timescale for EET depolarization in the BChl a-protein. In the context of our kinetic model (which assumes migration only occurs between proximate subunits), they are consistent with the ranges of hopping timescales $0 < w_{AB}, w_{AD} \leq (15 \text{ ps})^{-1}$ in combinations typified by Table 2.2. Figure 2.7 shows that depolarization studies alone cannot prove whether one of the migration patterns illustrated in Fig. 2.4 dominates EET; independent knowledge of the pertinent orientational factors

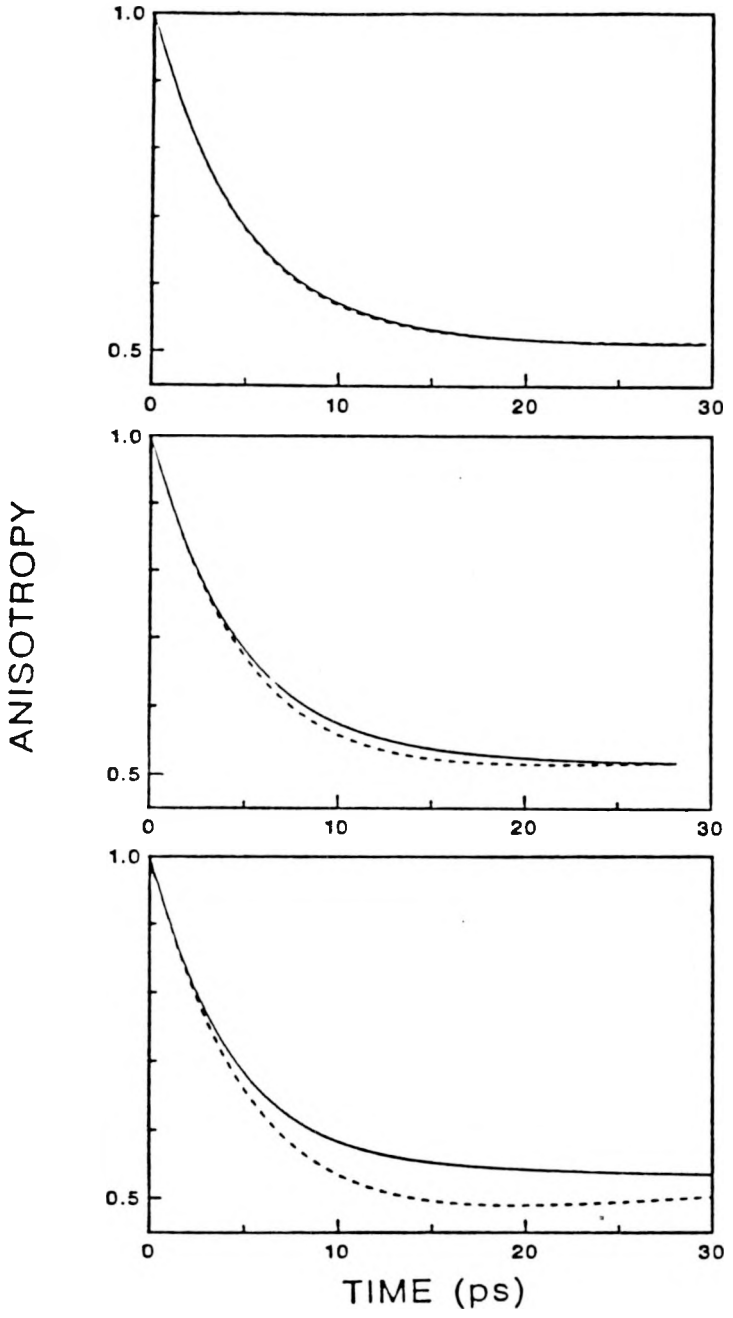

Figure 2.6 Calculated anisotropy functions r(t) from EET simulations in BChl a-protein for (top) w_{AB} = (20.2 ps)$^{-1}$, w_{AD} = (60.7 ps)$^{-1}$; (center) w_{AB} = w_{AD} = (28.5 ps)$^{-1}$; (bottom) w_{AB} = (66.0 ps)$^{-1}$, w_{AD} = (22.0 ps)$^{-1}$. Dashed and continuous curves are 7-trimer and 27-trimer simulations, respectively.

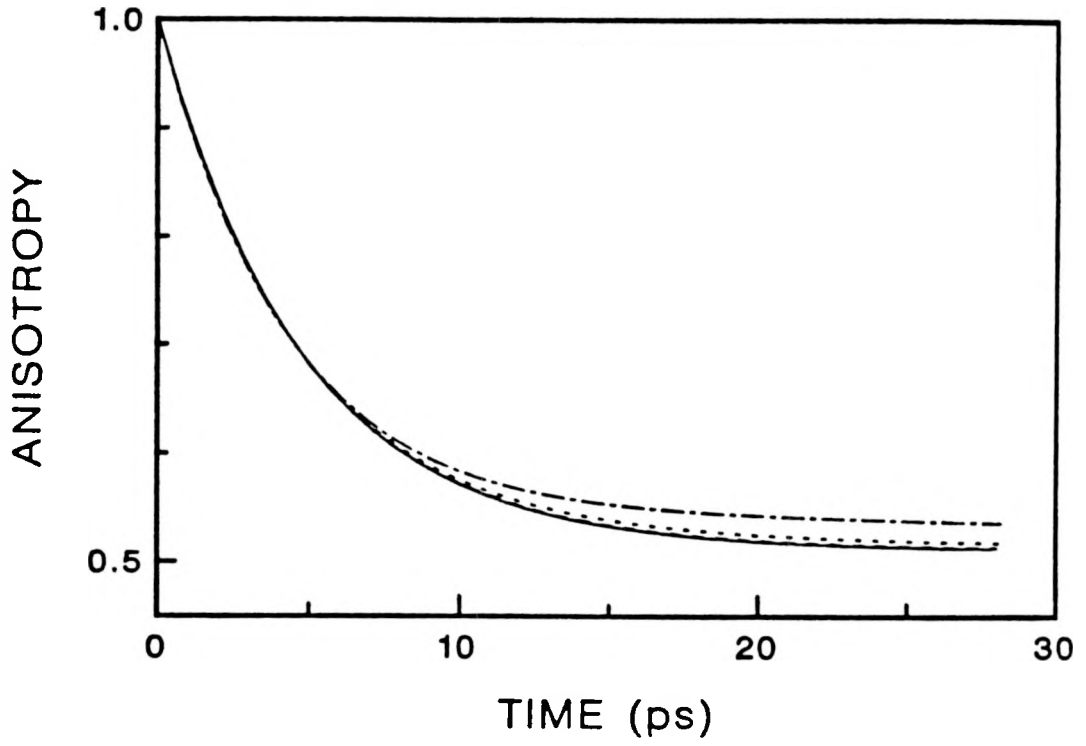

Figure 2.7 Calculated anisotropy functions r(t) from 27-trimer EET simulations, scaled to exhibit same decay time (4.78 ps) as the experimental mean from fits of 603 nm profiles using Eqs. 6.1. Anisotropy decays for cases (a) and (b), corresponding to $w_{AB}/w_{AD} = \infty$ and 3, are essentially congruent and are given by continuous curve. Cases (c) and (d), corresponding to $w_{AB}/w_{AD} = 1$ and 1/3, are given by dotted and dot-dashed curves respectively.

(e.g., from polarized single-crystal absorption studies of the 809 nm Q_y system or from successful modeling of exciton structure in the Q_y absorption and CD spectra) is required.

The 609 nm profiles are considerably noisier (S/N ~4) than those shown for 598 and 603 nm in Fig. 2.2. Their depolarization lifetimes, 3.48 and 1.47 ps, agree with the 603 nm mean (4.78 ps) within data scatter. The mean anisotropy parameter $\underline{a}$ = 0.477 at 603 nm agrees well with the values $\underline{a}$ = 0.497 and 0.485 obtained at 609 nm. This nominally corresponds to a Q_x exciton transition moment inclined 27° from the crystallite c-axis (Eq. 6.15). However, the P. aestuarii exciton bands overlap appreciably due to thermal broadening at 300K [7], and two distinct electronic transitions ($2\text{-}1^*$ and $1\text{-}2^*$ in the notation of Petke et al. [30]) contribute to the Q_x system. More than one exciton band may therefore contribute to the observed anisotropy.

At 598 nm, the depolarization lifetime (24 ps mean, Table 2.1) and lack of anisotropy contrast with the behavior exhibited at longer wavelengths. Wavelength variations in the anisotropy parameter $\underline{a}$ are easily rationalized in terms of contrasting exciton transition moment orientations within the Q_x system. Our model cannot account for the observed disparity in depolarization lifetime, however, because EET should occur in the lowest-energy exciton component in the 809 nm Q_y system irrespective of

excitation wavelength. In separate experiments, we obtained polarized Q_y fluorescence profiles from similar BChl *a*-protein solutions using a time-correlated single photon counting apparatus with 300 ps instrument function [7,8]. Under this resolution, profiles excited at 609 and 603 nm proved to be completely depolarized at all times, while discernible anisotropy ($I_{\parallel} > I_{\perp}$) appeared during the first few tens of ps in profiles excited at 593 nm. This behavior is consistent with the observed pump-probe depolarization timescales. These results suggest that some species other than BChl *a*-protein trimers contributes to the absorption at shorter wavelengths. Since the trimers cannot be dissociated into subunits without separating the BChl *a* from the protein [31], the impurity species may be randomly oriented BChl *a* molecules. This would explain the observed lack of anisotropy ($a = 0$) at 598 nm; the observed negative polarization ($I_{\parallel} - I_{\perp} < 0$) at 593 nm would be a consequence [32] of the perpendicular Q_x and Q_y transition moments exhibited by BChl *a* monomers. (The Q_x and Q_y transition moments are not generally orthogonal in BChl *a*-protein, owing to exciton interactions.) Furthermore, the Q_x spectrum of BChl *a* monomers in solution peaks to the blue (573 nm in ether [14]) of the BChl *a*-protein spectrum. The difficulty experienced in simulating the Q_y absorption and CD spectra of

similar BChl a-protein solutions may stem in part from such inhomogeneity.

In principle, crystallite orientational diffusion could contribute to the observed depolarization. The linear dichroism of electric field-aligned BChl a-protein particles exhibits a decay time of ~140 μs [19]. Particle reorientation is thus far too slow to account for our depolarization timescale, as would be expected for BChl a-protein aggregates containing several tens of trimers. The magic-angle photobleaching decay (Fig. 2.1) may be attributed to excitation trapping at defect sites in the interior and on the surface of the BChl a-protein particles. Its nonexponentiality is logically a consequence of dispersion in the aggregate size and random walk length. The dominant long-component lifetime (52.4 ps) of the biexponential fit to the magic-angle decay in Fig. 2.1 is equivalent to ~3.7 excitation hops between neighboring subunits. It is consistent with the 55.1 ps dominant component lifetime which we find in the magic-angle Q_y fluorescence profile excited at 603 nm: a triexponential fit to this profile yields the decay law $I(t) = 0.816\exp(-t/55.1\ \text{ps}) + 0.073\exp(-t/507\ \text{ps}) + 0.121\exp(-t/2247\ \text{ps})$.

ACKNOWLEDGEMENTS

We are indebted to Professor R. E. Fenna for the donation of the BChl *a*-protein. We are grateful to W. E. Catron for supporting one of us (T. P. C.) through a Research Fellowship. The Ames Laboratory is operated for the U. S. Department of Energy by Iowa State University under Contract No. W-7405-Eng-82. This work was supported by the Office of Basic Energy Sciences.

REFERENCES

1. Geacintov, N. E.; Breton, J. CRC Crit. Rev. Plant Sci. 1987, 5, 1.

2. Förster, Th. Discuss. Faraday Soc. 1959, 27, 7.

3. Sauer, K. In "Bioenergetics of Photosynthesis"; Govindjee, Ed.; Academic Press: New York, 1975; P 183.

4. Owens, T. G.; Webb, S. P.; Mets, L.; ALberte, R. S.; Fleming, G. Natl. Acad. Sci. USA 1987, 84, 1532.

5. Hemenger, R. P.; Lakatos-Lindenburg, K.; Pearlstein, R. M. J. Math. Phys. 1972, 13, 1056.

6. Pearlstein, R. M. Photochem. Photobiol. 1982, 35, 835.

7. Hart, D. E.; Anfinrud, P. A.; Struve, W. S. J. Chem. Phys. 1987, 86, 2689.

8. Anfinrud, P. A.; Struve, W. S. J. Chem. Phys. 1987, 87, 4256.

9. Causgrove, T. P.; Bellefeuille, S. M.; Struve, W. S. J. Phys. Chem., in press.

10. Huber, D. L.; Hamilton, D. S.; Barnett, B. Phys. Rev. B. 1977, 16, 4642.

11. Fenna, R. E.; Ten Eyck, L. F.; Matthews,. B. W. Biochem. Biophys. Res. Commun. 1977, 75, 751.

12. Olson, J. M. Biochim. Biophys. Acta 1980, 594, 33.

13. Tronrud, D. E.; Schmid, M. F.; Matthew, B. W. J. Mol. Biol. 1986, 188, 443.

14. Phillipson, K. D.; Sauer, K. Biochemistry 1972, 11, 1880.

15. Pearlstein, R. M.; Hemenger, R. P. Proc. Natl. Acad. Sci. USA 1978, 75, 4920.

16. Chang, J. C. J. Chem. Phys. 1977, 67, 3901.

17. Whitten, W. B.; Nairn, J. A.; Pearlstein, R. M. Biochim. Biophys. Acta 1978, 503, 251.

18. Lutz, M.; Hoff, A. J.; Brehamet, L. Biochim. Biophys. Acta 1982, 679, 331.

19. Whitten, W. B.; Pearlstein, R. M.; Phares, E. F.; Geacintov, N. E. Biochim. Biophys. Acta 1978, 503, 491.

20. French, P. M. W.; Taylor, J. R. In "Ultrafast Phenomena V"; Fleming, G. R.; Siegman, A. E., Eds.; Springer-Verlag: Berlin, 1986; p. 11.

21. Yasa, Z. A.; Amer, N. M. Opt. Commun. 1981, 36, 406.

22. Anfinrud, P.; Struve, W. S. Rev. Sci. Instrum. 1986, 57, 380.

23. van Grondelle, R.; Amesz, J. In "Light Emission by Plants and Bacteria"; Govindjee; Amesz, J.; Fork, D. C., Eds.; Academic Press: New York, 1986.

24. Fleming, G. R. "Chemical Applications of Ultrafast Spectroscopy"; Oxford University Press: New York, 1986.

25. Engh, R. A.; Petrich, J. W.; Fleming, G. R. J. Phys. Chem. 1985, 89, 618.

26. Anfinrud, P. A.; Hart, D. E.; Hedstrom, J. H.; Struve, W. S. J. Phys. Chem. 1986, 90, 2374.

27. Marion, J. B. "Classical Dynamics of Particles and Systems"; Academic Press: New York, 1965; p. 391.

28. Chuang, T. J.; Eisenthal, K. B. J. Chem. Phys. 1972, 57, 5094.

29. Stehfest, H. Commun. ACM 1970, 13, 47.

30. Petke, J. D.; Maggiora, G. M.; Shipman, L.; Christofferson, R. E. Photochem. Photobiol. 1979, 30, 203.

31. Matthews, B. W.; Fenna, R. E. Acc. Chem. Res. 1980, 13, 309.

32. Seely, G. R.; Connolly, J. S. In "Light Emission by Plants and Bacteria"; Govindjee; Amesz, J.; Fork, D. C., Eds.; Academic Press: New York, 1986.

SECTION III. ELECTRONIC EXCITATION TRANSPORT IN CORE ANTENNAE OF ENRICHED PHOTOSYSTEM I PARTICLES FROM SPINACH CHLOROPLASTS

ELECTRONIC EXCITATION TRANSPORT IN CORE ANTENNAE OF ENRICHED PHOTOSYSTEM I PARTICLES FROM SPINACH CHLOROPLASTS

Shumei Yang, Timothy P. Causgrove, and Walter S. Struve

Department of Chemistry and Ames Laboratory-USDOE

Iowa State University, Ames, Iowa 50011

and

John H. Golbeck

Department of Chemistry, Portland State University

Portland, Oregon 97207

INTRODUCTION

Electronic excitation transport (EET) in antenna chlorophyll complexes of green photosynthetic organisms has been extensively modeled by theoreticians [1-7]. Singlet excitation, created by photon absorption in light-harvesting antenna complexes, is believed to migrate by an incoherent random-walk mechanism until it is trapped at a reaction center complex. The excitation hopping is governed by a resonance dipole-dipole interaction [8] which produces transition rates varying with chromophore separation as R^{-6}. Little structural information exists concerning the chlorophyll organization in green plant antennae; EET in such systems is frequently treated under the assumption that the chromophores occupy sites on a regular lattice [2,3]. It is now recognized that antenna chlorophyll molecules are complexed with proteins into clusters of six or more chromophores [7,9]. In Sauer's "pebble mosaic" model [9], electronic excitation is rapidly delocalized within such clusters, and migrates relatively slowly between clusters. Calculations which contrast the EET dynamics in a regular lattice with those in model systems containing strongly interacting clusters of five molecules [2] predict similar timescales in both cases for excitation trapping at reaction centers. Kinetic measurements of

antenna fluorescence quenching by reaction centers therefore cannot easily differentiate between the regular lattice model and the pebble mosaic model for antenna EET.

Owens et al. [10] recently studied antenna fluorescence lifetimes in photosystem I core antennae of P700 Chl a-protein complexes from barley, and in a photosynthetic mutant of Chlamydomonas reinhardtii without the photosystem II antenna/reaction center complex. They determined that the fluorescence lifetime varied linearly with core antenna size in both species, in accordance with random walk models [11,12] in which the Chl a chromophores occupy sites in a regular lattice. Further analysis of the fluorescence profiles yielded a single-step EET time of 0.1 - 0.2 ps between chromophores in photosystem I core antennae. The excitation migration was found to be nearly diffusive, and photoconversion in the reaction center occurred on an average of once per 2.4 excitation visits from the core antenna.

In a separate work [13], we performed a polarized pump-probe study with ~1.5 ps resolution on the structurally well-characterized BChl a-protein from the green photosynthetic bacterium Prosthecochloris aestuarii. Solutions of the BChl a-protein in triglycerophosphate buffer were excited in the Q_x system with linearly polarized pulses between 598 and 609 nm, and

probed with pulses polarized parallel or perpendicular to the pump polarization. The resulting transient photobleaching profiles $A_{\parallel}(t)$, $A_{\perp}(t)$ were fitted with convolutions of the laser autocorrelation function with the expressions

$$A_{\parallel}(t) = P(t)\{1 + 0.8[(1-a)\exp(-t/\tau) + a]\}$$
$$A_{\perp}(t) = P(t)\{1 - 0.4[(1-a)\exp(-t/\tau) + a]\} \qquad (3.1)$$

The isotropic function $P(t)$, which describes ground-state recovery in BChl a-protein if the Q_x and Q_y excited states do not absorb at the probe wavelength, was determined from magic-angle profiles obtained with the probe polarization rotated by 54.7° from the pump polarization. The time-dependent depolarization implicit in Eqs. 3.1 describes the reorientation in the probed transition moment accompanying EET. Such pump-probe experiments therefore focus on the initial steps following laser excitation, rather than on overall random walk duration. At 603 nm, the mean depolarization lifetime τ for BChl a-protein was 4.78 ps. The depolarization dynamics were analyzed with a kinetic model [13] based on the crystal structure [14] of BChl a-protein, in which the basic structural unit is a trimer of subunits containing 7 BChl a molecules each. Spectroscopic evidence [15,16] suggests that strong exciton interactions exist between BChl a

chromophores inside a subunit; the model therefore assumed that Förster excitation hopping occurred between exciton states delocalized inside subunits. EET was arbitrarily restricted to migration between neighboring subunits, and two kinds of hopping were distinguished. The first kind occurred with transition rate w_{AB} between subunits in the same trimer (e.g., A→B or D→E in the projection of the BChl a-protein $P6_3$ crystal structure shown in Fig. 3.1). The second kind occurred with rate w_{AD} between subunits in different trimers (e.g. A→D or B→H). The 4.78 ps depolarization lifetime observed at 603 nm proved to be consistent with combinations of w_{AB} and w_{AD} satisfying $(w_{AB} + w_{AD})^{-1} \simeq 15$ ps. In the limiting case where $w_{AB}/w_{AD} \gg 1$ (i.e., where intratrimer transport occurs far more rapidly than intertrimer transport), the theoretical expressions for $A_{\parallel}(t)$, $A_{\perp}(t)$ become identical to Eqs. 3.1; the observed depolarization lifetime τ is then related to the intratrimer hopping rate w_{AB} by $w_{AB} = (3\tau)^{-1}$. In such a case, the transition rate w_{AB} consistent with $\tau = 4.78$ ps would be $(14.3 \text{ ps})^{-1}$. Nonzero values of the residual anisotropy parameter a were required to fit most polarized pump-probe profiles using Eqs. 3.1, owing to the nonrandom chromophore orientations in BChl a-protein. For the trimer packing geometry illustrated in Fig. 3.1, the parameter a is related to the direction cosine γ of the probed exciton

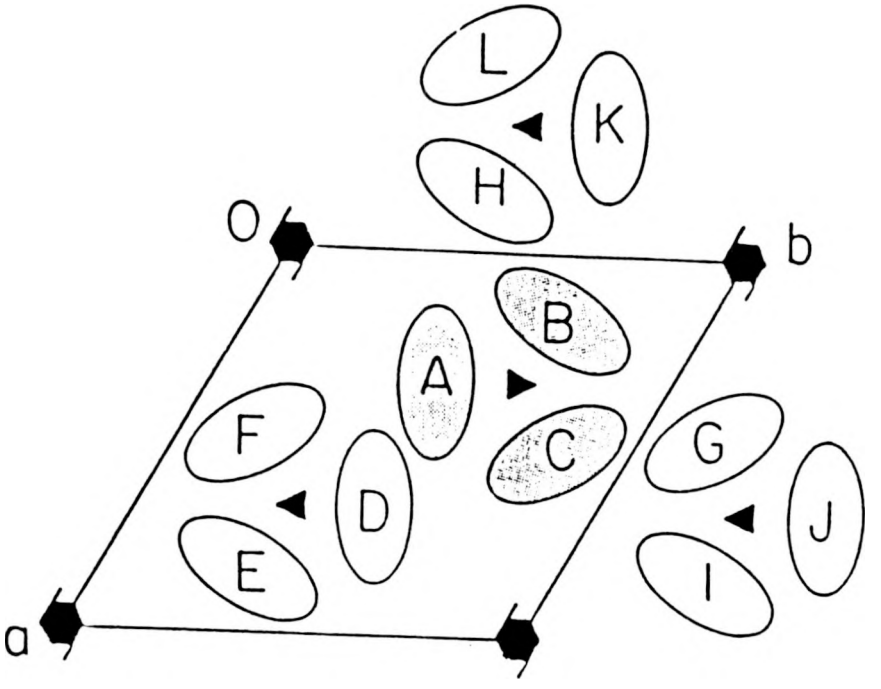

Figure 3.1 Schematic projection upon the ab-plane of the $P6_3$ crystal structure of BChl a-protein from Prostecochloris aestuarii, the only bacterial antenna system whose 3-dimensional structure is known. Unit cell dimensions are a = b = 111.9 Å, c = 98.6 Å [14]. Trimers DEF, GIJ, and HKL are separated from trimer ABC by 49.3 Å along the c-axis.

transition moment along the trimer symmetry axis by [13] $\underline{a} = (3\gamma^2 - 1)^2/4$.

In the present work, the pump-probe experiments have been extended to the Chl _a_-protein core antenna complex in enriched photosystem I particles from spinach chloroplasts. The antenna Chl _a_-protein architecture is unknown in spinach (as in other plants), and these experiments offer clues on the Chl _a_ chromophore organization. The present pump and probe wavelengths (665 - 681 nm) overlap the lowest-energy band in the Q_y system of the enriched PS I particles (Fig. 3.2), providing direct excitation and monitoring of the singlet electronic state involved in transport. (This configuration contrasts with the BChl _a_-protein work [13] in which Q_y transport was monitored following excitation of the Q_x system.) The polarized profiles $A_{\parallel}(t)$, $A_{\perp}(t)$ from spinach PS I core antennae are remarkably similar to those obtained from _P. aestuarii_, and their isotropic decays $P(t)$ yield direct information concerning the excitation trapping at the reaction centers.

EXPERIMENTAL

For experiments performed between 665 and 681 nm, a multiline Ar^+ laser with 6 W plasma tube pumped a passively mode-locked dual-jet DCM/DDCI dye laser to produce vertically polarized pulses with ~40 mW average power at 125 MHz repetition rate. Autocorrelation traces at these wavelengths displayed FWHM ranging from 1.75 ps to 2.15 ps. The output beam was split into pump and probe beams, which were modulated at 5.0 and 0.5 MHz respectively with ~80% modulation depth using Isomet 1206C acousto-optic modulators. The pump beam delay was varied by reflection from a translatable BK-7 corner cube prism mounted on a Micro-Controle UT10050PP translation stage. The beam polarizations were defined using calcite Glan-Thompson prism polarizers; the probe polarization was fixed at 45° from the laser polarization, while the pump polarization was varied. Both beams were focussed to ~10 μm diameter in the sample using a 7.3 cm f.l. lens, and the average incident power was ~5 mW in each beam. The probe beam was monitored by an EG&G FOD-100 photodiode, and phase-locked single-sideband detection was performed at 5.5 MHz using a modified Drake R-7A radio receiver [17].

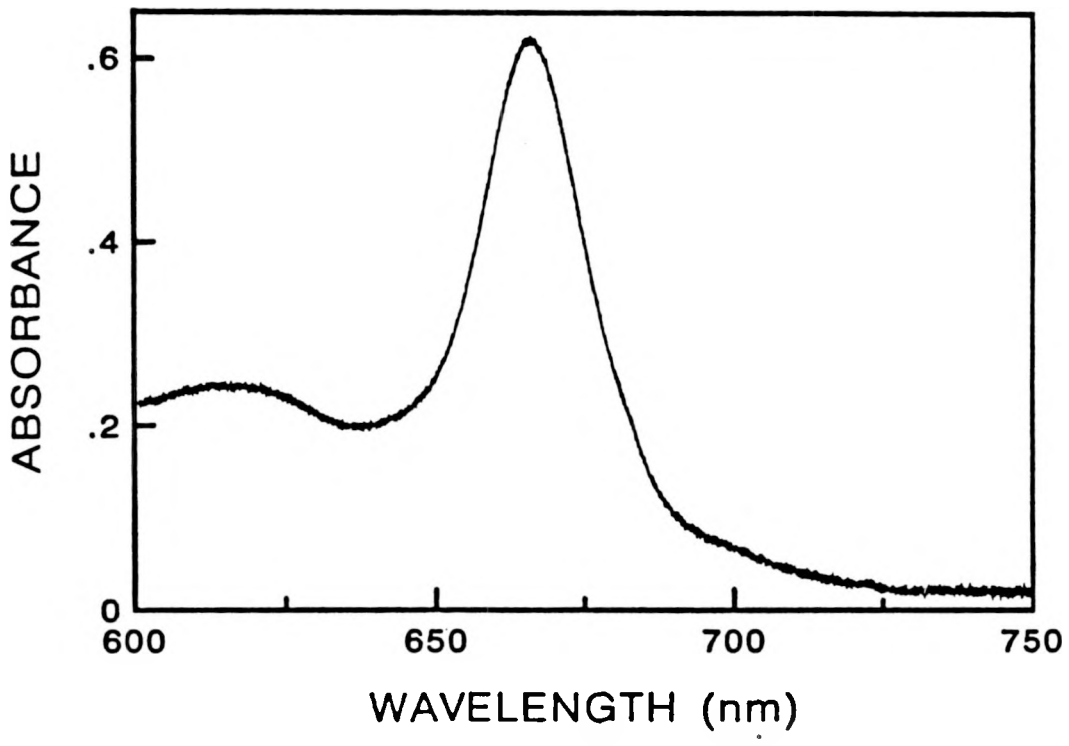

Figure 3.2 Absorption spectrum of PS I-60 particles from spinach at 1.6°K.

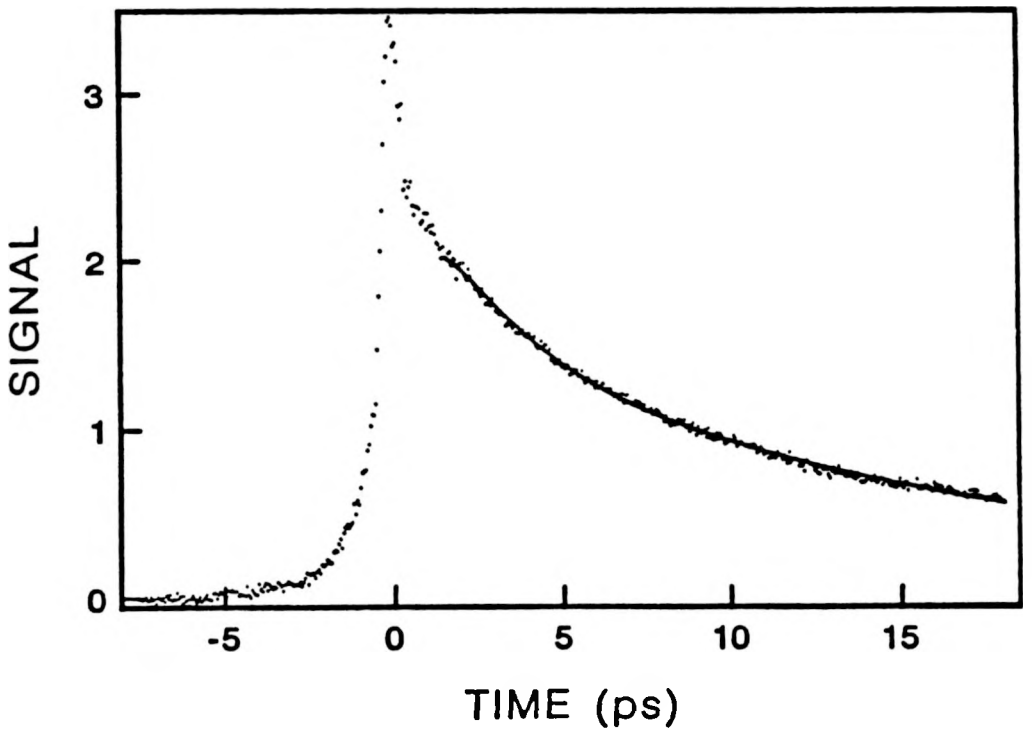

Figure 3.3 Magic-angle profile for PS I-60 particles at 675 nm. Continuous curve is convolution of laser autocorrelation function with biexponential decay law $P(t) = 0.534\exp(-t/1.99\ \text{ps}) + 0.466\exp(-t/16.8\ \text{ps})$.

Table 3.1 Biexponential fitting parameters for magic-angle profiles from spinach photosystem I particles

Wavelength, nm	Scan duration, ps	A_1	τ_1, ps	A_2	τ_2, ps
665	25	0.725	1.41	0.275	18.7
	25	0.781	1.10	0.219	17.2
	25	0.744	1.25	0.256	16.8
	25	0.712	1.29	0.288	17.0
	50	0.678	3.94	0.322	36.8
	50	0.699	2.78	0.301	28.2
670	25	0.597	1.64	0.403	17.6
	25	0.599	1.69	0.401	17.8
	25	0.624	1.69	0.376	18.2
	25	0.615	1.47	0.385	16.5
	50	0.630	4.39	0.370	29.8
	50	0.634	4.38	0.366	31.8
675	25	0.520	2.00	0.480	15.8
	25	0.534	1.99	0.466	16.8
	25	0.570	2.99	0.430	19.9
	50	0.665	5.97	0.335	33.0
	50	0.672	6.06	0.328	32.5
	50	0.632	5.67	0.368	31.9
681	25	0.551	3.38	0.449	19.7
	25	0.506	2.83	0.494	17.9
	50	0.613	6.47	0.387	23.2
	50	0.460	4.90	0.540	18.5
	50	0.541	5.69	0.459	22.8
	50	0.568	6.00	0.432	22.7
	50	0.544	6.13	0.456	22.9
	50	0.629	5.60	0.371	29.1
	50	0.603	5.64	0.397	25.9

Table 3.2 Fitting parameters for polarized pump-probe profiles from photosystem I particles from spinach

Wavelength, nm	Scan duration, ps	a	a	τ, ps	τ, ps
665	25	0.489	0.625	4.36	6.59
	25	0.658		7.73	
	25	0.677		7.02	
	25	0.402		6.77	
	50	0.687		0.92	
	50	0.837		12.8	
670	25	0.427	0.466	5.00	3.65
	25	0.409		2.79	
	25	0.409		3.31	
	25	0.489		2.88	
	50	0.651		5.54	
	50	0.412		2.43	
675	25	0.460	0.431	2.47	2.85
	25	0.458		2.91	
	25	0.446		2.01	
	50	0.313		2.33	
	50	0.492		3.72	
	50	0.419		3.64	
681	25	0.542	0.627	3.37	3.47
	50	0.636		2.91	
	50	0.621		2.68	
	50	0.671		5.51	
	50	0.674		4.19	
	50	0.725		3.00	
	50	0.522		2.66	

The receiver's signal-bearing 50 kHz intermediate frequency was tapped and demodulated in a Stanford Research Systems SR510 lock-in amplifier (LIA). Pump-probe data were transmitted from the LIA through an RS-232 port to a DEC MINC-23 computer operating in a TSX-Plus multi-user environment, where they were normalized to the square of the instantaneous laser intensity detected by a second EG&G FOD-100 monitor photodiode.

The PS I-60 sample preparation, which extracts solutions of highly purified reaction center particles enriched in iron-sulfur protein and P700 from spinach chloroplasts, has been described previously [18]. A PS I-60 particle contains an 82-83 kDa reaction center Chl a-protein complex (CP I), along with 6 to 8 polypeptides (8-25 kDa) which are not complexed with chlorophyll and are termed Subunits II-VIII [19]. CP I and Subunits II-VIII contain two 2Fe-2S centers and two 4Fe-4S centers, respectively; the 43-45 kDa light-harvesting Chl a/Chl b antenna complex (LHC I) present in PS I-110 particles [19] are absent in PS I-60. The particles are largely free of Chl b, cytochromes f, b_6, and b-559; their β-carotene content is considerably reduced. PS I-60 solutions in water, glycerol, Tris buffer, and Triton X-100 exhibited ~2.5 optical density at 675 nm in a 1 cm cell. Samples were housed between λ/4 fused silica flats separated by an 800 μm teflon spacer, and were rotated at 12 Hz during pump-probe scans

to minimize photooxidation by the laser beams. All experiments were performed at room temperature.

RESULTS

Close similarities appear among the PS I-60 magic-angle photobleaching profiles obtained at 665, 670, 675, and 681 nm, wavelengths which lie near the peak of the main Chl *a* Q_y absorption band of the core antenna (Fig. 3.2). The isotropic decay at these wavelengths is nonexponential; a typical 675 nm magic-angle profile is shown in Fig. 3.3. Each of the magic-angle profiles was fitted for times later than ~1.5 ps with a convolution of the laser autocorrelation function with a biexponential decay law; the resulting optimized parameters are listed in Table I. Two pump-probe scan durations were used (25 and 50 ps); the final biexponential parameters depend on the duration selected, in consequence of the multi-exponential character of the isotropic decays. The profiles accumulated using 25 ps sweeps invariably show a dominant short component with average lifetime between 1.26 ps (665 nm) and 3.11 ps (681 nm); the long component lifetimes are distributed about a mean of 17.8 ps with a standard deviation of 1.2 ps. The short component tends to exhibit a somewhat larger preexponential factor at 665 nm than at 670, 675, or 681 nm. There is little else to distinguish among the isotropic decays at these four wavelengths. Nearly identical magic-angle profiles were obtained when the pump

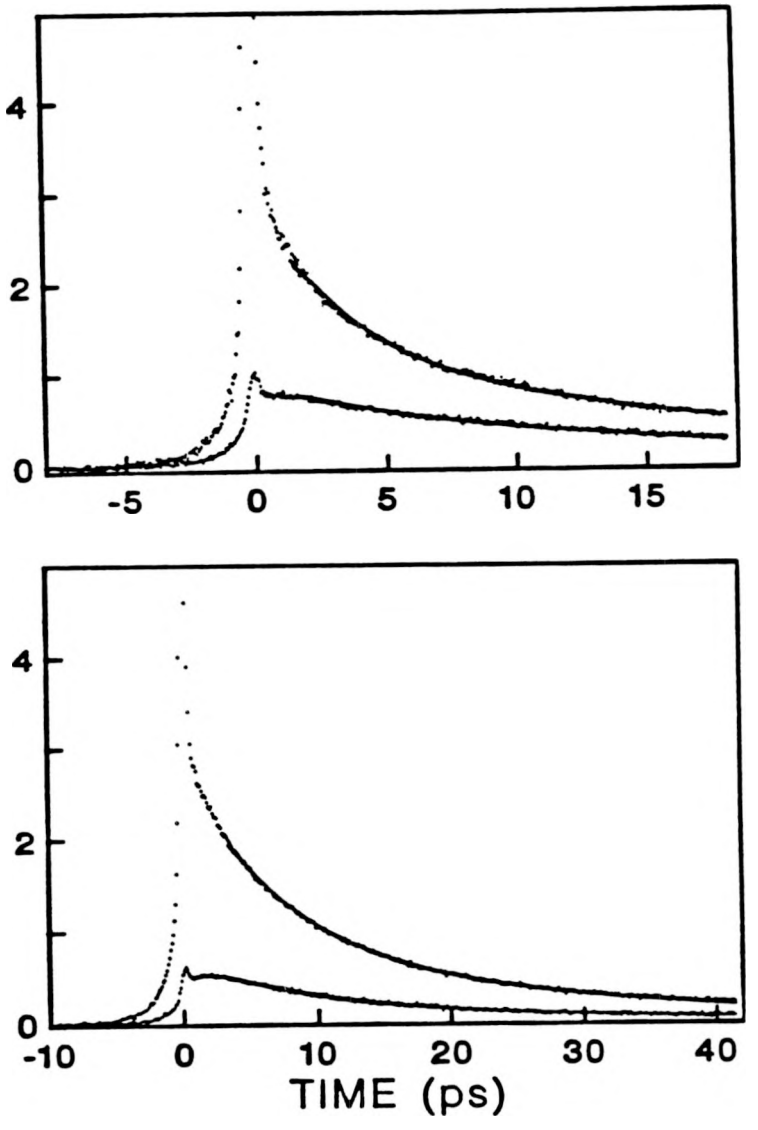

Figure 3.4 Polarized pump-probe transients for PS I-60 particles at 675 nm (upper panel) and at 681 nm (lower panel). In each panel, the upper and lower traces correspond to A (t) and A (t) respectively. Continuous curves show convolutions of laser autocorrelation function with Eqs. 3.1, with lifetime and anisotropy parameters as described in text. Parameters for displayed profiles are τ = 2.90 ps, $\underline{a}$ = 0.458 (675 nm), and τ = 2.91 ps, $\underline{a}$ = 0.636 (681 nm).

and probe beams were both attenuated by 50%; exciton annihilation is not a major component of the isotropic decay. A caveat should be attached to the present use of the 125 MHz laser repetition rate, which corresponds to 8 ns pulse spacing. While the intersystem crossing quantum yield in Chl *a* is low, sufficiently high repetition rates can build up appreciable triplet state populations to introduce artifacts into the absorption transients. Cavity-dumped pump-probe experiments testing the effects of variable repetition rate are planned in our laboratory.

Polarized transient profiles $A_{\parallel}(t)$ and $A_{\perp}(t)$ are shown in Fig. 3.4 for 675 and 681 nm. Such profiles were fitted with convolutions of the autocorrelation function with Eqs. 3.1 using a linked convolute-and-compare algorithm described previously [20]. The biexponential parameters in the isotropic decay P(t) were held at the optimized values obtained from deconvolution of the corresponding magic-angle profiles (Table I); the phenomenological depolarization lifetime τ and the residual anisotropy parameter *a* were varied. The final parameters from these linked deconvolutions are listed in Table II. Since $A_{\parallel}(t)/A_{\perp}(t)$ do not tend to unity at long times (cf., Fig. 3.4), nonzero anisotropy parameters were generally required to fit the polarized transients. (According to Eqs. 3.1, this ratio

approaches $(1 + 0.8\underline{a})/(1 - 0.4\underline{a})$ as $t \rightarrow \infty$.) Moreover, the anisotropy parameter depends on the wavelength probed. The difference between the average anisotropy parameters $\underline{a} = 0.431$ and 0.627 at 675 and 681 nm, respectively, is significantly larger than their standard deviations, 0.062 and 0.069. This wavelength variation is also reflected in Fig. 3.4, in which the profiles exhibit contrasting asymptotic ratios $A_{\parallel}(t)/A_{\perp}(t)$ at 675 and 681 nm. The average depolarization lifetimes $\bar{\tau}$ range from 6.59 ps at 665 nm to 2.85 ps at 675 nm. This depolarization timescale is similar to that found in BChl _a_-protein from _P. aestuarii_ [13], and the residual anisotropy in PS I-60 is also reminiscent of the behavior exhibited that system. The former observation is pertinent to the physical interpretation of the transient depolarization in _P. aestuarii_, since those experiments probed photobleaching in the Q_x rather than the Q_y system of the BChl _a_-protein [14]. The similarity of the depolarization timescales in the two species corroborates the attribution of the BChl _a_-protein depolarization to EET, rather than to nonradiative processes such as $Q_x \rightarrow Q_y$ internal conversion.

DISCUSSION

Owens et al. [10] recently reported that the fluorescence decay of P700 Chl a-protein preparations with Chl a/P700 ratios <40 exhibits a dominant component with lifetime between 15 and 30 ps. This order of magnitude is commensurate with our PS I-60 isotropic long-component decays ($\bar{\tau}$ = 17.8 ps) in Table I, and suggests that our isotropic decay mechanism for 665 nm < λ < 681 nm is efficient excitation trapping at the P700 reaction center. The short components in Table I typically contribute <15% of the integrated photobleaching decay, and would escape detection under the 60-80 ps instrument function [10] in time-correlated single photon counting.

While much is now known about the 3-dimensional structure of BChl a-protein from P. aestuarii [14], the light-harvesting Chl a/b-protein complex of photosystem II [21], and the light-harvesting C-phycocyanin biliprotein from the blue-green alga Mastigocladus laminosus [22], we are unaware of similar data on the structure of photosystem I core antennae. The oligomers in the well-characterized pigment-containing proteins in photosynthetic systems have all proven to be trimers, perhaps because three-fold symmetry is the minimum required for isotropic absorption of light polarized in a plane perpendicular

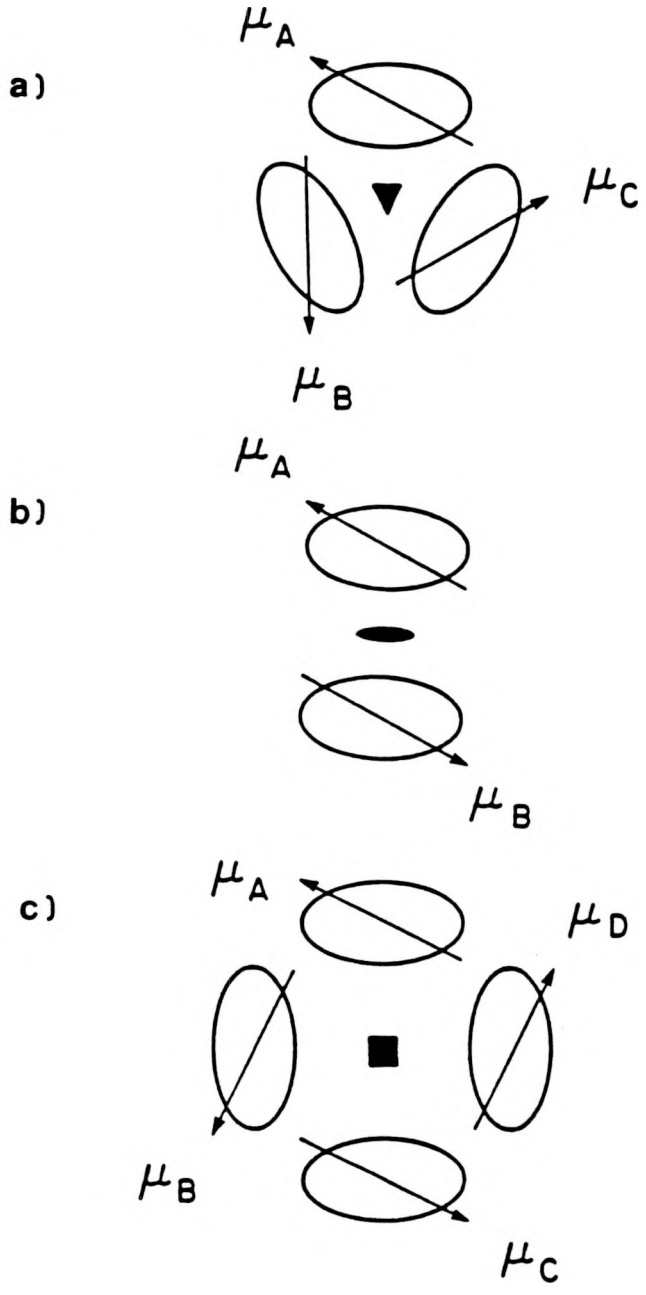

Figure 3.5 Oligomeric Chl a-protein models for interpretation of time-dependent depolarization due to EET: (a) trimer, as in BChl a-protein from P. aestuarii; (b) dimer; and (c) tetramer.

to the oligomer's symmetry axis [14]. We therefore consider kinetic depolarization models similar to one proposed earlier [13] for EET in BChl a-protein. Closed-form expressions for $A_{\parallel}(t)$ and $A_{\perp}(t)$ are obtained when the intratrimer transition rate w_{AB} is assumed to be much faster than the intertrimer transition rate w_{AD}. Under these conditions, the exciton state populations A(t), B(t), C(t) in subunits A, B, and C following creation of an exciton state in subunit A evolve as [13]

$$\begin{aligned} A(t) &= A_0[1 + 2\exp(-3w_{AB}t)]/3 \\ B(t) &= C(t) = A_0[1 - \exp(-3w_{AB}t)]/3 \end{aligned} \tag{3.2}$$

where k is the rate constant for hopping between adjacent subunits. The corresponding expressions for the polarized transient components are

$$A_{\parallel}(t) = P(t)[\langle\mu_{Ax}^4\rangle A(t) + \langle\mu_{Ax}^2\mu_{Bx}^2 + \mu_{Ax}^2\mu_{Cx}^2\rangle B(t)] \tag{3.3a}$$

$$A_{\perp}(t) = P(t)[\langle\mu_{Ax}^2\mu_{Ay}^2\rangle A(t) + \langle\mu_{Ax}^2\mu_{By}^2 + \mu_{Ax}^2\mu_{Cy}^2\rangle B(t)] \tag{3.3b}$$

Here μ_A, μ_B, μ_C are the exciton transition moments in subunits A, B, C; the laboratory-fixed x and y axes are oriented along the parallel and perpendicular probe polarizations, respectively. EET between adjacent subunits in a trimer rotates the probed

exciton transition moment by $2\pi/3$ about the trimer symmetry axis. Rotational averaging of Eqs. 3.3 over the random BChl *a*-protein crystallite orientations in solution then leads to Eqs. 3.1 for the polarized transients $A_{\parallel}(t)$ and $A_{\perp}(t)$, provided that $\tau = 1/3w_{AB}$ and $\underline{a} = (3\gamma^2 - 1)^2/4$. We may also consider dimers (n=2) and tetramers (n=4) as possible oligomeric forms *a priori* (Fig. 3.5). Exciton migration between adjacent subunits with rate constant w_{AB} rotates the probed exciton transition moment by $2\pi/n$ about the oligomer symmetry axis. For dimers, our kinetic model again leads to Eqs. 3.1 for $A_{\parallel}(t)$ and $A_{\perp}(t)$, with the depolarization lifetime and residual anisotropy parameter given by $\tau = 1/2w_{AB}$ and $\underline{a} = 1 - 3\gamma^2 + 3\gamma^4$. For tetramers, the model leads to more complicated expressions with three depolarization lifetimes,

$$A_{\parallel}(t) = P(t)\{(2-2\gamma^2+3\gamma^4) + (1+2\gamma^2-3\gamma^4)\exp(-4kt) + 2(\gamma^2-\gamma^4)[\exp(-2kt) - \exp(-6kt)]\} \quad (3.4a)$$

$$A_{\perp}(t) = P(t)\{(3+2\gamma^2-3\gamma^4) + (3\gamma^4-2\gamma^2-1)\exp(-4kt) - 2(\gamma^2-\gamma^4)[\exp(-2kt) - \exp(-6kt)]\}/2 \quad (3.4b)$$

While these do not exhibit the form of Eqs. 3.1, the asymptotic depolarization at long times may be described for tetramers using an effective anisotropy parameter

$\underline{a} = 2.5[A_{\parallel}(\infty) - A_{\perp}(\infty)]/[A_{\parallel}(\infty) + 2A_{\perp}(\infty)] = (3\gamma^2 - 1)^2/4.$

Generalization of these kinetic models to include EET between subunits belonging to different oligomers would require knowledge of the oligomer packing in photosystem I core antennae; this architecture has not been characterized.

All of these models generally predict a nonvanishing anisotropy parameter $\underline{a}$ in consequence of the nonrandom chromophore organizations in the oligomers. The observation of $\underline{a} \neq 0$ in Table II establishes for the first time that local ordering exists in the Chl $\underline{a}$-protein core antenna of PS I-60, irrespective of the oligomer model assumed. Polarized photobleaching decays exhibiting the form of Eqs. 3.1 are consistent with either dimers of trimers as basic Chl $\underline{a}$-protein structural units. In our judgement, the present time resolution and profile S/N (cf., Fig. 3.4) are not sufficient to differentiate between the single-exponential polarization decay predicted for dimers and trimers (Eqs. 3.1) and the multiexponential decay expected in higher oligomers (e.g., Eqs. 3.4) and in more sophisticated kinetic models incorporating transport between oligomers. This question may be resolved by performing similar pump-probe experiments with a high-power, low-noise Nd:YAG-pumped dye laser. If the oligomers are assumed to be trimers of Chl $\underline{a}$-protein subunits, the average depolarization

lifetimes $\bar{\tau}$ = 6.59 and 2.85 ps at 665 and 675 nm (Table II) correspond to rate constants $w_{AB} = (19.8 \text{ ps})^{-1}$ and $(8.6 \text{ ps})^{-1}$ respectively for hopping between adjacent subunits. The fractional scatter in depolarization lifetimes τ is considerably larger than that in the anisotropy parameters a, because the depolarization timescale exceeds the laser pulse FWHM by less than an order of magnitude.

The depolarization timescale in PS I-60 is more than an order of magnitude slower than the 0.2 ps single-step hopping time calculated by Owens et al. [10] using a regular lattice model for EET in P700 Chl a-protein complex preparations. A logical rationalization for the comparatively long depolarization lifetimes τ in Table II is that they arise from EET between clusters of Chl molecules, rather than between individual chromophores. On the basis of spectral hole-burning experiments on PS I core antenna complexes, Gillie et al. [23] have already pointed out that the antenna protein structure may endow EET with some delocalized exciton character. In this interpretation, the wavelength variation in the resi-dual anisotropy parameter would stem from contrasting directions of trans-ition moments in different exciton components of the Chl a-protein Q_y sys-tem. A detailed rationalization of time-domain experiments like

ours awaits better structural characterization of the Chl *a*-protein complexes.

ACKNOWLEDGEMENTS

We are grateful to W. E. Catron for supporting one of us (T. P. C.) through a Research Fellowship. We thank Professor John Golbeck for providing the PS I-60 preparations, and we thank Mr. J. Kevin Gillie for obtaining the PS I-60 absorption spectrum in Fig. 3.2. We are indebted to Professors Gerald Small and Kenneth Sauer for illuminating discussions. The Ames Laboratory is operated for the U. S. Department of Energy by Iowa State University under Contract No. W-7405-Eng-82. This work was supported by the Office of Basic Energy Sciences.

REFERENCES

1. Knox, R. S. In "Bioenergetics of Photosynthesis"; Govindjee, Ed.; Academic Press: New York, 1975.

2. Knox, R. S. In "Primary Processes of Photosynthesis", Vol. 2; Barber, J., Ed.; Elsevier: Amsterdam, 1977.

3. Pearlstein, R. M. In "Photosynthesis: Energy Conversion by Plants and Bacteria", Vol. 1; Govindjee, Ed.; Academic Press: New York, 1982.

4. Paillotin, G. J. Theor. Biol. 1972, 36, 223.

5. Paillotin, G. J. Theor. Biol. 1976, 58, 219.

6. van Grondelle, R. Biochim. Biophys. Acta 1985, 811, 147.

7. Geacintov, N. E.; Breton, J. CRC Crit. Rev. Plant Sci. 1987, 5, 1.

8. Förster, Th. Discuss. Faraday Soc. 1959, 27, 7.

9. Sauer, K. In "Bioenergetics of Photosynthesis"; Govindjee, Ed.; Academic Press: New York, 1975.

10. Owens, T. G.; Webb, S. P.; Mets, L.; ALberte, R. S.; Fleming, G. R. Proc. Natl. Acad. Sci. USA 1987, 84, 1532.

11. Hemenger, R. P.; Lakatos-Lindenburg, K.; Pearlstein, R. M. J. Math. Phys. 1972, 13, 1056.

12. Pearlstein, R. M. Photochem. Photobiol. 1982, 35, 835.

13. Causgrove, T. P.; Yang, S.; Struve, W. S. J. Phys. Chem. 1988, 92, 6121.

14. Matthews, B. W.; Fenna, R. E. Acc. Chem. Res. 1980, 13, 309.

15. Philipson, K. D.; Sauer, K. Biochemistry 1972, 11, 1880.

16. Pearlstein, R. M.; Hemenger, R. P. Proc. Natl. Acad. Sci. USA 1978, 75, 4920.

17. Anfinrud, P.; Struve, W. S. Rev. Sci. Instrum. 1986, 57, 380.

18. Golbeck, J. H. Methods Enzymol. 1980, 69, 129.

19. Green, B. R. Photosyn. Res. 1988, 15, 3.

20. Anfinrud, P. A.; Hart, D. E.; Hedstrom, J. H.; Struve, W. S. J. Phys. Chem. 1986, 90, 2374.

21. Lyon, M. K.; Unwin, P. N. T. Photochem. Photobiol. 1988, 47, 30S (Abstracts of the 16th Annual Meeting for the American Society for Photobiology, March 13-17, 1988).

22. Schirmer, T.; Bode, W.; Huber, R.; Sidler, W.; Zuber, H. J. Mol. Biol. 1985, 184, 257.

23. Gillie, J. K.; Hayes, J. M.; Small, G. J.; Golbeck, J. H. J. Phys. Chem. 1986, 90, 3795.

SECTION IV. POLARIZED PUMP-PROBE SPECTROSCOPY OF PHOTOSYSTEM I ANTENNA EXCITATION TRANSPORT

POLARIZED PUMP-PROBE SPECTROSCOPY OF PHOTOSYSTEM I ANTENNA EXCITATION TRANSPORT

Shumei Yang, Timothy P. Causgrove, and Walter S. Struve

Department of Chemistry and Ames Laboratory-USDOE

Iowa State University, Ames, Iowa 50011

INTRODUCTION

The structure and electronic excitation transport (EET) dynamics in photosystem I core and peripheral antennae of green plants have been extensively studied by protein/pigment characterization [1-5], absorption and circular dichroism (CD) spectra [6-8], and subnanosecond fluorescence [8-15] and picosecond absorption [16-19] spectroscopy. The PS I core antenna contains some 25-30 Chl a molecules [6] that are complexed with the P700 reaction center by two polypeptides, whose molecular weights have been variously reported as in the 60-70 kD range [20, 21] and as 82, 83 kD [1]. The peripheral antenna comprises Chl a and Chl b chromophores complexed with several smaller (19-25 kD) polypeptides [4, 5, 22, 23]. Recent CD studies of the molecular organization in the PS I core antenna [6, 7] suggest that the chlorophylls are grouped in clusters of 5-7 molecules, which is reminiscent of the known chromophore grouping in the bacteriochlorophyll a-protein from the green sulfur bacterium Prosthecochloris aestuarii [24, 25].

It has long been recognized that the 670-680 nm Chl a core antenna Q_y absorption band encompasses several spectrally distinguishable Chl a excited states [26]. These may arise a priori from exciton interactions among strongly coupled

chromophores, from localized excitations on spectrally different Chl a molecules (e.g., due to contrasting porphyrin conformations occasioned by nonuniform protein environment), or from both. Such spectral inhomogeneity raises two major issues concerning the antenna structure and transport kinetics in PS I. The first of these deals with the spatial organization of the spectral Chl a forms and its bearing on the EET dynamics. Enriched PS I particles with contrasting core antenna sizes including particles with Chl a/P700 ratio as low as 8-10 [27] exhibit very similar absorption spectra [8]. Hence, removal of antenna chlorophylls in preparations yielding different core antenna sizes does not alter the proportions of Chl a species responsible for various Q_y subbands. This appears to be inconsistent with the "funnel" model [28] for antenna structure, in which the shorter wavelength Chl a species are visualized at the periphery and the longer-wavelength species are proximate to the reaction center. Alternatively, the Chl a spectral forms may be randomly distributed about the reaction center, so that the statistical ratios of spectral forms left intact in solutions of PS I particles with decreasing antenna size are invariant. Finally, the spectral Chl a forms in the core antenna may be complexed into identical protein subunits containing identical, inhomogeneous sets of chromophores; detergent fractionation may

then reduce the antenna size in quantum steps of one subunit, automatically preserving the species population ratios. Owens et al. [8] showed that the time-resolved core antenna excitation and fluorescence spectra of PS I core antennae are independent of antenna size. Their time-resolved spectra indicated that the emitting Chl a species are not limited to the long-wavelength form(s), but are "nearly homogenized" over all of the spectral forms present throughout the emission lifetime. This rapid "homogenization" of core antenna excitation argues against the "funnel" model (in which excitation transport occurs sequentially from short-wavelength to long-wavelength components); it is consistent with randomly distributed spectral forms, and with spectral forms organized into essentially identical subunits.

The second issue is the extent of excitonlike (delocalized) character of PS I antenna excitations. Owens et al. [9] measured fluorescence lifetimes in PS I core antennae of P700 Chl a-protein complexes from barley, and in a photosynthetic mutant of Chlamydomonas reinhardtii without the PS II antenna/reaction center complex. The lifetime of the fast fluorescence component varied linearly with core antenna size in both species, in agreement with random walk models [29, 30] in which the excitations were assumed to be localized on Chl a chromophores occupying sites on a regular lattice. Analysis of the

fluorescence profiles yielded a single-step EET time of 0.1-0.2 ps between chromophores. The excitation migration was found to be nearly diffusive, and photoconversion in the reaction center typically occurred once per 2.4 excitation visits from the core antenna. More recently [31], we obtained polarized photobleaching profiles through pump-probe spectroscopy on PS I-60 particles enriched in iron-sulfur protein and P700 (Chl a/P700 ratio ~60). At the wavelengths 665, 670, 675, and 681 nm, the photobleaching polarization decayed with mean lifetimes between 2.9 and 6.6 ps. This comparatively slow timescale suggested that the depolarization accompanied EET between clusters of Chl a chromophores, rather than between individual nearest-neighbor chromophores. Considerable residual anisotropy appeared in the photobleaching profiles at long times, proving that local ordering exists in the Chl a-protein core antenna complex of PS I-60.

In order to clarify the relationship between the pump-probe depolarization dynamics [31] and the numerous PS I antenna fluorescence studies [8-15], we have extended our work to PS I-200 particles (Chl a/ P700 ~200) from spinach chloroplasts. Details of the magic-angle Chl a photobleaching decay observed in this work between 660 and 681 nm closely parallels the multiexponential fluorescence decays reported

elsewhere [8,9] for particles of similar size. At shorter wavelengths (645-655 nm), the magic-angle decay is dominated by a fast (~5 ps lifetime) component that is likely associated with excitation migration from Chl b. The observed Chl a depolarization lifetime between 660 and 681 nm exhibits marked wavelength dependence, behavior which was masked by the lower S/N and narrower wavelength range accessible in our earlier PS I-60 work. This wavelength dispersion in depolarization lifetime is consistent with predictions of Förster excitation transport rates based on published PS I core antenna absorption and fluorescence spectra [7,8]. Our results point to a PS I core antenna model in which the excitations are thermalized spectrally less than 1 ps, but require considerably more time (several ps) for spatial homogenization. This model is consistent with Sauer's "pebble mosaic" model [32], in which electronic excitation is rapidly delocalized within clusters of chlorophyll chromophores, and migrates relatively slowly between clusters.

EXPERIMENTAL

The PS I-200 particles (Chl/P700 ratio ~200) were isolated from spinach chloroplasts following the procedure of Mullet et al. [22]. Such native PS I particles retain all of the polypeptides which bind the light-harvesting antenna, core antenna, P700 reaction center, and associated electron acceptors [33]. The Chl a/Chl b ratio in the light-harvesting complex is ~3.5, and contains some 100 chromophores [4, 34, 35]; the overall Chl a/Chl b ratio for PS I-200 particles is ~6 [34, 35]. PS I-200 particles exhibit the structural and functional properties of PS I in thylakoids [34]. Particles were stored at 77 K in a buffered glycerol-water mixture (pH = 8.3) with 0.1% Triton X-100. In contrast, the PS I-60 particles used in earlier work [31] were largely free of Chl b, cytochromes f, b_6, and b-559, and their β-carotene content was considerably reduced [36]. They contained the 82, 83 kD reaction center Chl a-protein complex, together with 6 to 8 polypeptides (8-25 kD) which are not complexed with chlorophyll. The light-harvesting Chl a/Chl b antenna complex present in PS I-200 particles was absent in PS I-60. Samples were housed between λ/4 fused silica flats separated by an 800 μm teflon spacer, and were rotated at 12 Hz

during pump-probe experiments to minimize photooxidation by the laser beams. All experiments were performed at room temperature.

The pump-probe apparatus and optics were identical to those used previously [31]. The multiline Ar^+ laser used for pumping the passively mode-locked dye laser was superseded by a Coherent Antares 76-s Nd:YAG cw mode-locked laser, which generated 532 nm SH pulses with ~2 W average power at 76 MHz repetition rate. The SH pulse width was ~70 ps FWHM. The hybrid mode-locked dye laser contained two jets (DCM lasing dye, DDCI saturable dye) and yielded vertically polarized pulses at wavelengths between 645 and 681 nm. A Coherent Model 7210 cavity dumper head driven by a Coherent Model 7200 driver reduced the natural 76 MHz pulse repetition rate to values as low as 1 MHz to check for effects of long-lived excited state buildup on the Chl a/b photobleaching transients. Autocorrelation traces taken between 645 and 681 nm typically exhibited ~1.5 ps fwhm. The pump and probe beams were modulated at 3.0 and 0.5 MHz respectively using Isomet 1206C acoustooptic modulators. A BK-7 corner cube prism mounted on a Micro-Controle UT10050PP translation stage delayed the pump beam. Beam polarizations were selected by calcite Glan-Thompson prism polarizers; the probe polarization was maintained at 45° from the vertical laser polarization, while the pump polarization was alternatively parallel to, perpendicular to, or displaced 54.7°

from the probe polarization. The two beams were focussed into the sample using a 7.3 cm f.l. lens. The probe beam was monitored by an EG&G FOD-100 photodiode, and phase-locked single-sideband detection was achieved at the 3.5 MHz sum frequency using a modified Drake R-7A radio receiver [37]. The receiver's internal 50 kHz signal-bearing frequency was demodulated in a Stanford Research Systems SR510 lock-in amplifier. Pump-probe data were transmitted to a DEC MINC-23 computer, where they were normalized to the square of the instantaneous laser intensity detected by a second EG&G FOD-100 monitor photodiode.

RESULTS

Isotropic photobleaching decay

A perspective display of the wavelength dependence of the PS I-200 magic-angle photobleaching decay (obtained with the pump and probe polarizations 54.7° apart) is given in Fig. 8-1. The coherent coupling artifact at very early times [38] is a consequence of the single wavelength pump-probe technique used; the relative S/N ratios obtained at different wavelengths reflect on the available laser power as well as on the photobleaching action spectrum (vide infra). The continuous curves in Fig. 8-1 show the optimized convolutions of the laser autocorrelation functions (obtained with a KDP SHG crystal in place of the sample) with a single-exponential decay law (645 nm), biexponential decay laws (650 and 655 nm), and triexponential decay laws (660 through 681 nm). The final fitting parameters for all analyzed magic-angle profiles are listed in Table 4.1. At wavelengths between 660 and 681 nm, a minimum of three exponentials is required to describe the decay. The first component τ_1 in Table 4.1, with lifetime typically 1 to 2 ps, has no counterpart in the fluorescence decays observed in PS I core antennae [8-15], because photon counting instrument functions are limited to $\gtrsim$45 ps fwhm. Similar short-lifetime components were

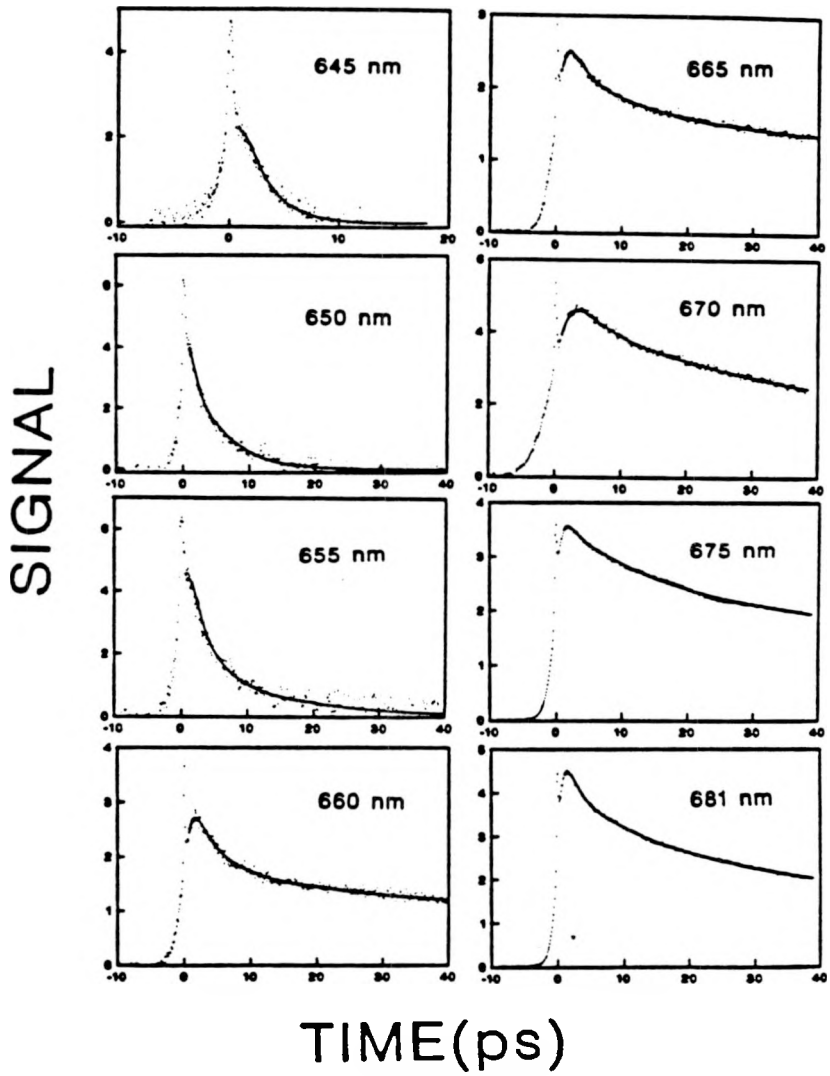

Figure 4.1 Magic-angle photobleaching transients for PS I-200 particles at eight wavelengths from 645 to 681 nm. The pump and probe wavelengths are identical. Continuous curves are optimized convolutions of laser autocorrelation functions with bi-exponential decay law (645-655 nm) and triexponential decay law (660-681 nm). Note different time scale used at 645 nm.

Table 4.1 Multiexponential fitting parameters for magic-angle profiles for PS I-200 particles from spinach

$$P(t) = A_1\exp(-t/\tau_1) + A_2\exp(-t/\tau_2) + A_3\exp(-t/\tau_3)$$

Wavelength nm	A_1	τ_1, ps	A_2	τ_2, ps	A_3	τ_3, ps
645	1.000	2.00				
	1.000	2.04				
	0.713	2.11	0.287	2.11		
650	0.506	0.765	0.494	4.54		
	-0.131	1.64	0.869	2.24		
	-0.231	3.12	0.769	3.21		
	0.753	0.393	0.247	4.86		
	0.727	0.267	0.273	2.76		
	0.679	1.60	0.321	7.95		
655	0.776	2.43	0.224	13.9		
	0.810	2.67	0.190	24.1		
	0.869	2.84	0.131	29.2		
	0.807	2.81	0.193	25.9		
	0.829	2.81	0.171	39.6		
660	0.448	2.56	0.227	12.6	0.325	250
	0.367	1.32	0.294	7.94	0.339	250
	0.436	3.50	0.182	15.7	0.382	250
	0.472[a]	2.20	0.286	33.6	0.242	250
665	0.342	1.92	0.263	14.2	0.395	250
	0.493	1.19	0.180	11.5	0.327	250
	0.426	1.47	0.205	11.4	0.369	250
	0.458[a]	1.43	0.344	34.8	0.198	250

[a]Magic angle profiles obtained from 250 ps scans. All other profiles were obtained using 50 ps sweeps.

Table 4.1 (continued)

Wavelength nm	A_1	τ_1, ps	A_2	τ_2, ps	A_3	τ_3, ps
670	0.489	1.11	0.240	14.9	0.271	250
	0.433	1.72	0.302	21.8	0.265	250
	0.317[a]	3.67	0.421	37.0	0.262	250
675	0.413	1.34	0.175	24.5	0.412	194
	0.563	0.500	0.128	16.0	0.309	194
	0.564	0.557	0.173	16.0	0.263	194
	0.339[a]	3.21	0.241	39.0	0.420	254
	0.330[a]	4.23	0.257	44.7	0.413	255
	0.342[a]	2.42	0.210	29.8	0.448	215
681	0.340	1.23	0.224	12.3	0.436	179
	0.377	0.225	0.206	13.1	0.416	179
	0.329	1.65	0.222	13.5	0.445	179
	0.340	1.23	0.224	12.3	0.436	179
	0.358[a]	4.15	0.243	38.1	0.399	234
	0.576[a]	1.48	0.163	26.9	0.261	213
	0.558[a]	2.36	0.182	23.9	0.260	212

observed in our PS I-60 pump-probe experiments between 665 and 681 nm [31]. The optimized values of the second and third component lifetimes τ_2 and τ_3 depend on the duration selected for pump-probe scans. The second-component lifetimes τ_2 derived from the longer (250 ps) scans in Table 4.1 are generally 25-40 ps, times which resemble the "fast" fluorescence components reported by Owens et al. [8] for photosystem I particles with Chl/P700 ratios $\gtrsim$40; they are also similar to the fast PS I fluorescence decay times reported for chloroplasts and intact algae [39]. Third-component lifetimes τ_3 obtained from 250 ps scans at 675 and 681 nm (Table 4.1; not shown in Fig. 4.1) are clustered around 200 to 250 ps; these are similar to the "intermediate" fluorescence components characterized in PS I preparations with Chl a/P700 ratios greater than 65 [8, 40, 41]. This decay component was not observed in our PS I-60 pump-probe experiments [31]. Less accurate values for τ_3 are obtained in triexponential fits of magic-angle profiles obtained with 50 ps scans (cf., Fig. 4.1), whose durations are considerably shorter than τ_3 values derived from 250 ps scans. (The 50 ps scans were accumulated for purposes of modeling the isotropic decay function for analysis of the polarized photobleaching decays, because the depolarization timescale proved to be much faster than τ_3.) The 660-681 nm magic-angle decays monitored using 50 ps time windows were

therefore fitted with a triexponential model function in which τ_3 was fixed at 250 ps, and the other five triexponential parameters were floated. We do not attach physical significance to the final parameters for triexponential fits to these 50 ps magic-angle profiles, which are used only to separate the isotropic and anisotropic portions of the polarized photobleaching profiles.

While the magic-angle profiles for 660-681 nm in Fig. 4.1 superficially appear to exhibit risetimes (i.e., rising portions following the coherent spikes at t=0), the convolute-and-compare analysis shows that this phenomenon is entirely a consequence of the broad wing on the laser pulse shape autocorrelation. The unusually broad "risetime" feature in the 670 nm panel of Fig. 4.1, for example, is accompanied by a visibly broadened rising (t<0) edge in the profile. Deconvolution of these profiles with triexponential model functions uncovered no evidence for any risetime components (negative preexponential factors); we estimate that any risetimes present would be much shorter than 1 ps.

In preliminary PS I-200 magic-angle profiles taken at 675 and 681 nm, the third-component lifetime τ_3 was found to be ~170 ps. Reduction of the laser power in the pump and probe beams yielded τ_3 in the 200-250 ps range reported in Table 4.1; the isotropic decay in the earlier profiles was accelerated by exciton

annihilation. The laser power employed in the earlier profiles had been shown to be sufficiently low to avoid annihilation effects in photobleaching decay of PS I-60 particles, and so the PS I-200 profiles which exhibited τ_3 ~ 170 ps indicate that the effective domain size [42] in 660-681 nm photobleaching is significantly larger in PS I-200 than PS I-60 particles.

The 250 ps maximum time window of our pump-probe scans was insufficiently wide to verify the presence of the 5-6 ns "long" decay component observed by Owens et al. in PS I antenna fluorescences [8, 9]. The PS I-200 isotropic photobleaching signal typically decayed to ~15% of the initial amplitude by 250 ps, so the upper limit on the preexponential factor for such a component is conservatively estimated to be less than 0.1.

At the three shortest wavelengths (645, 650, and 655 nm) the 200-250 ps decay component is absent, and the decay is well represented within noise by a biexponential law. The isotropic decay accelerates toward shorter pump-probe wavelengths, and exhibits ~2 ps lifetime at 645 nm. Figure 4.2, which plots the wavelength dependence of preexponential factors A_1 and A_3 for the first and third triexponential decay components, emphasizes this trend toward more rapid magic-angle decay in the blue portion (645-655 nm) of the spectrum.

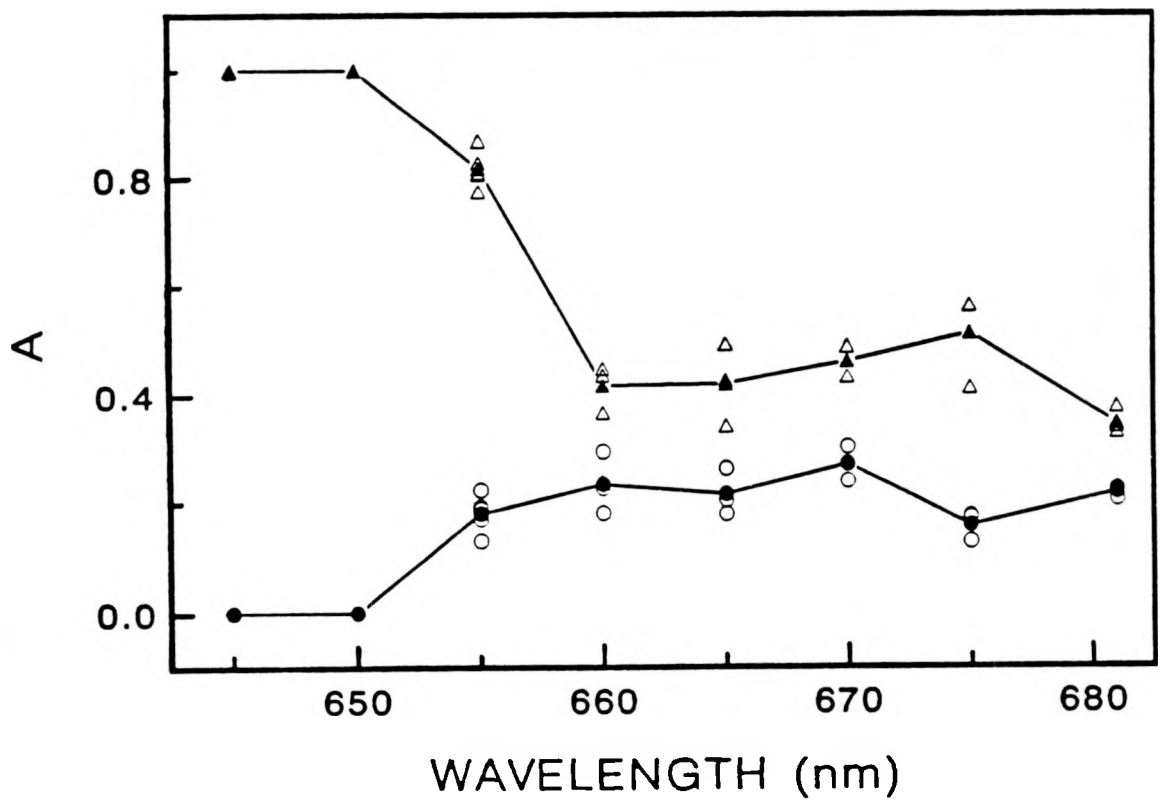

Figure 4.2 Wavelength dependence of preexponential factors A_1, A_3 for triexponential fits to PS I-200 magic-angle photobleaching decays, $P(t) = A_1\exp(-t/\tau_1) + A_2\exp(-t/\tau_2) + A_3\exp(-t/\tau_3)$. The sum of preexponential factors is normalized to unity at each wavelength.

The majority of these pump-probe profiles were accumulated with the dye laser cavity dumper repetition rate at 9.5 MHz. In separate experiments, isotropic photobleaching profiles were obtained for PS I-60 particles at several repetition rates down to 1 MHz; the profiles were not materially changed by such reductions in repetition rate. This fact, coupled with the similarity in PS I antenna excited state lifetime parameters found here and in the fluorescence studies [8-15], is convincing evidence that artifacts arising from long-lived excited state buildup are not present in this work. Our previous experience with pump-probe spectroscopy of EET in alcohol solutions of rhodamine 640 [43] has shown that accurate isotropic and anisotropic photobleaching profiles are readily obtainable even when the laser pulse spacing is considerably shorter than the T_1 state lifetime.

Anisotropic photobleaching decay

Representative anisotropic pump-probe profiles, generated using parallel and perpendicular pump-probe polarizations, are shown for PS I-200 particles at 665 and 675 nm in Fig. 8-3. The simplest time-dependent functions capable of modeling these and the other anisotropic profiles obtained at 660 through 681 nm have the form

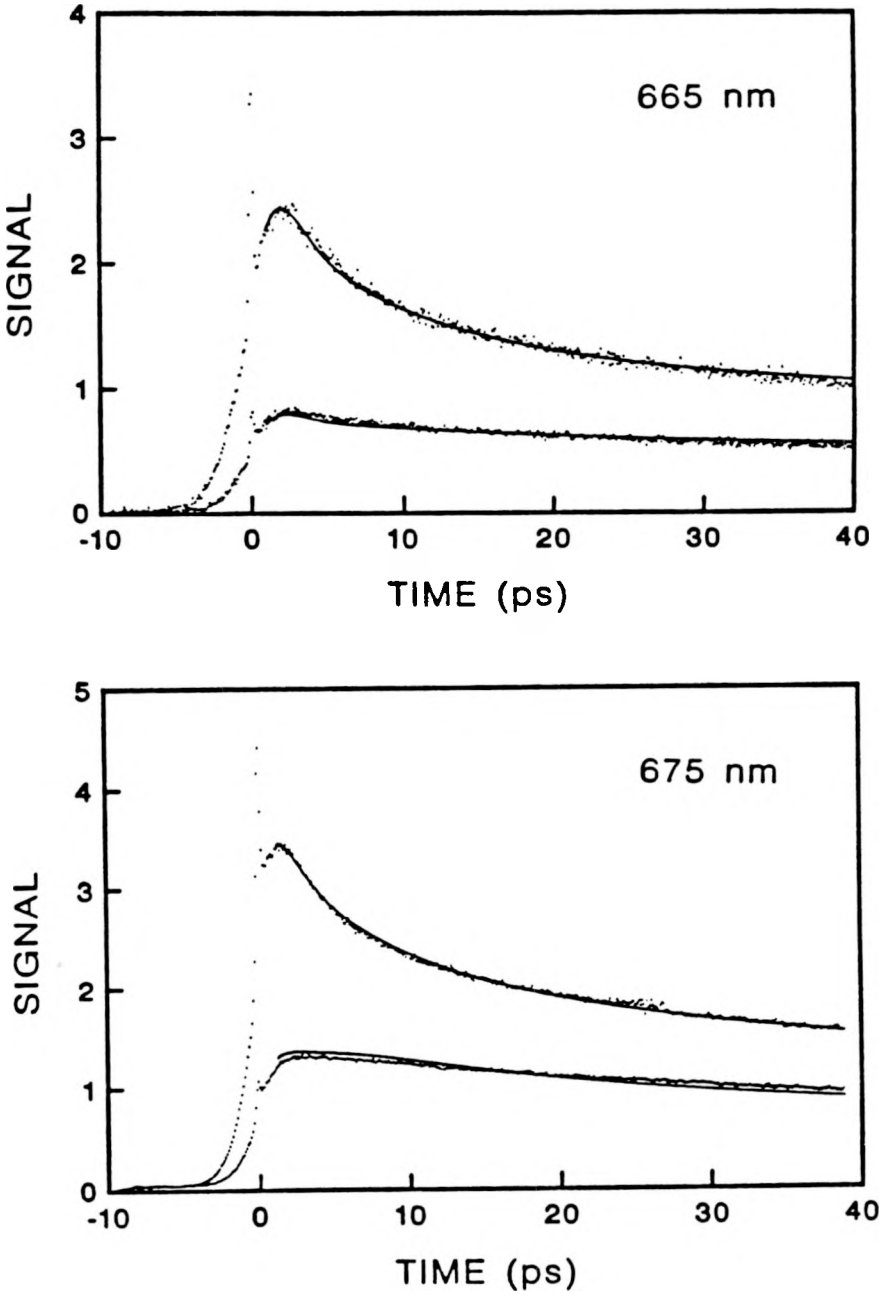

Figure 4.3 Anisotropic photobleaching transients for PS I-200 particles at 665 and 675 nm. At each wavelength, the upper (lower) profile was obtained using parallel (perpendicular) pump and probe polarizations. Continuous curves are optimized convolutions of Eqs. 8.1 with the laser pulse autocor-relation functions. At 665 nm, τ = 11.1 ps and a = 0.469; at 675 nm, τ = 4.87 ps and a = 0.429.

$$A_{\parallel}(t) = P(t)\{1 + 0.8[(1-a)r(t) + a]\}$$

$$A_{\perp}(t) = P(t)\{1 - 0.4[(1-a)r(t) + a]\} \qquad (4.1)$$

Here $P(t)$ is the magic-angle photobleaching decay measured with pump and probe polarizations separted by 54.7°. $r(t)$ is an anisotropy decay function, initialized to unity at zero time, which tends to zero at long times. The presence of the residual anisotropy parameter $\underline{a} \neq 0$ is necessitated by the fact that $A_{\parallel}/A_{\perp}$ does not approach unity at long times (cf., Fig. 4.3)

$$A_{\parallel}(\infty)/A_{\perp}(\infty) = (1 + 0.8a)/(1-0.4a) \qquad (4.2)$$

or

$$a = 2.5[A_{\parallel}(\infty) - A_{\perp}(\infty)]/[A_{\parallel}(\infty) + 2A_{\perp}(\infty)] \qquad (4.3)$$

Pairs of anisotropic profiles $A_{\parallel}(t)$, $A_{\perp}(t)$ were deconvoluted from the laser pulse autocorrelation function using a linked convolute-and-compare scheme [44] in which the six triexponential parameters in the isotropic decay function $P(t)$ were frozen at the values found in the magic-angle profile analyses (Table 4.1). The anisotropy decay function $r(t)$ was phenomenologically modeled as single-exponential, although some evidence for nonexponentiality surfaced in the anisotropic profiles with higher S/N (e.g., bottom half of Fig. 4.3) and such nonexponentiality can be expected theoretically (see Discussion). The final depolarization lifetimes τ (based on $r(t) = \exp(-t/\tau)$) and residual anisotropy

Table 4.2 Anisotropic fitting parameters for anisotropic profiles for PS I-200 particles from spinach

$$A_{\parallel}(t) = P(t)\{1 + 0.8[(1-a)\exp(-t/\tau) + a]\}$$

$$A_{\perp}(t) = P(t)\{1 - 0.4[(1-a)\exp(-t/\tau) + a]\}$$

Wavelength, nm	τ, ps	a
660	13.3	0.612
	15.8	0.342
	11.3	0.605
	11.9	0.369
665	8.79	0.468
	7.81	0.413
	11.1	0.469
	10.7	0.523
670	3.82	0.336
	6.34	0.321
	7.48	0.293
675	4.50	0.337
	4.26	0.366
	6.37	0.620
681	6.99	0.528
	7.82	0.556
	5.67	0.476

parameters a yielded by the linked deconvolutions are listed in Table 4.2. These depolarization lifetimes are plotted in Fig. 4.4 (open circles), along with their averages (closed circles), as a function of pump-probe wavelength. Other symbols represent calculations which will be discussed below. The depicted trend, hinted at in our earlier PS I-60 work in which our DCM dye lasing bandwidth was limited to wavelengths greater than 665 nm, clearly shows that the depolarization lifetime increases from ~4 ps to ~13 ps as the pump-probe wavelength is tuned toward the blue from 675 to 660 nm.

At the three shortest wavelengths (645, 650, and 655 nm) where the isotropic decay is dominated by components with <5 ps lifetime (Table 4.1), no evidence was found for depolarization on the timescale of several ps. Gillbro et al. [45] recently observed polarized photobleaching decays in the light-harvesting Chl a/b complex from photosystem II. They found that rapid energy transfer occured from Chl b to Chl a (6 ± 4 ps), and that no depolarization appeared in the Chl b photobleaching during the lifetime of Chl b excitation. However, they found evidence for excitation redistribution (~20 ps timescale) between differently oriented Chl a chromophores. Since the Chl b absorption in PS I is concentrated at the shorter wavelengths studied here (645-655 nm) and the antenna Chl a absorption system is centered at 670-680

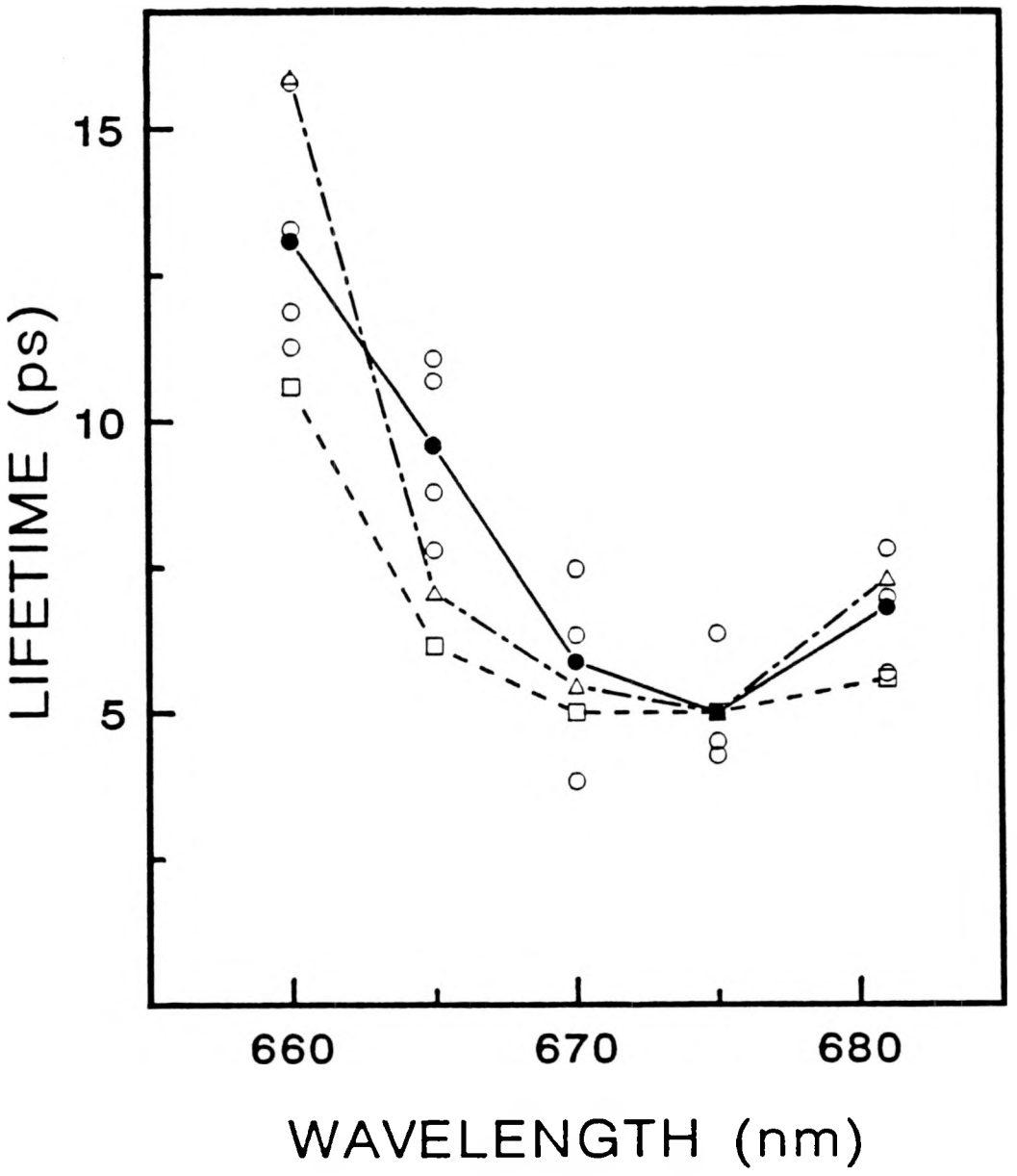

Figure 4.4 Pump-probe wavelength variation of depolarization lifetimes τ from deconvolution of anisotropic transients using Eqs. 8.1 with $r(t) = \exp(-t/\tau)$. Open circles are lifetimes derived from single pairs of profiles $A_{\parallel}(t)$, $A_{\perp}(t)$; filled circles are averaged values. Calculated lifetimes from deconvolution of PS I-13 and PS I-200 absorption spectra are given by squares and triangles, respectively.

nm (Discussion section), the LHC II depolarization behavior reported by Gillbro et al. qualitatively parallels that observed here in PS I-200.

Photobleaching action spectra

The wavelength dependence of the pump-probe signals between 655 and 692 nm was evaluated by measuring the signals at 100 ps and 7 ps and normalizing them to the square of the incident laser power at the pertinent wavelength. In Fig. 4.5, we show the action spectrum of the 100 ps signal (which is a measure of the intensity of the third photobleaching component with lifetime τ_3 ~ 200-250 ps), the 7 ps signal, and the difference between the 7 ps signal and the 100 ps signal extrapolated back to 7 ps using the lifetimes τ_3 in Table 4.1. The latter difference yields an estimate of the action spectrum of the second photobleaching component, with lifetime τ_2 in the tens of ps. For comparison, the PS I-200 steady-state absorption spectrum [46] is also shown. The action spectra peak well to the red (~680 nm) of the PS I-200 Chl *a* steady-state absorption band maximum at ~670 nm. This situation contrasts with fluorescence excitation spectra reported for a PS I preparation with Chl *a*/P700 = 33 [8], which closely approximate the steady-state absorption spectrum.

DISCUSSION

Many of the PS I-200 pump-probe phenomena reported here have been anticipated in earlier accounts of PS I time-resolved fluorescence experiments [8-15] and in our polarized pump-probe studies of PS I-60 particles [31]. Aside from an ultrafast component (τ_1 ~ 1-3 ps) which overlaps the coherent spike, the multiexponential isotropic decays at 660-681 nm are dominated by components with lifetimes τ_2 = 25-40 ps and τ_3 = 200-250 ps. These coincide with the "fast" and "intermediate" fluorescence lifetime components observed by Owens et al. [8] for PS I particles with Chl *a*/P700 ratios ≥65. No isotropic photobleaching component with lifetime $\gtrsim$ 20 ps was found in our PS I-60 work [31], in agreement with earlier reports [8, 9] that the "intermediate" component is absent in PS I particles with Chl *a*/P700 < 65. The pump-probe depolarization timescales found between 665 and 681 nm (Fig. 4.4) are commensurate with those seen in PS I-60 [31]. All of these correspondences between our data and the earlier time-resolved PS I experiments confirm that while these pump-probe studies are potentially subject to artifacts from long-lived excited state buildup, exciton annihilation, and variations in PS I fractionation techniques, they do furnish

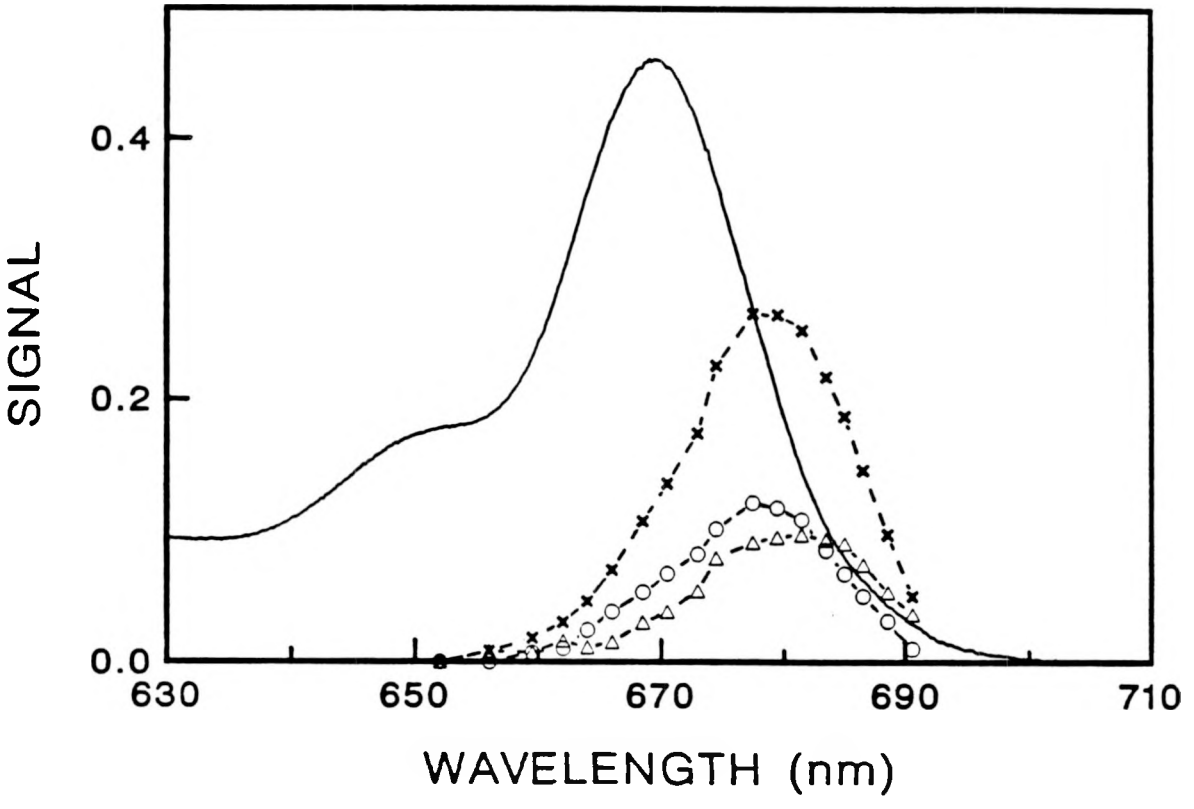

Figure 4.5 Photobleaching signal normalized to the square of incident laser power at 7 ps (crosses), 100 ps (circles), and the difference between the 7 ps normalized signal and the 100 ps normalized signal extrapolated back to 7 ps using the life-times τ_3 in Table 4.1 (triangles). Continuous curve is low temperature steady-state absorption spectrum of PS I-200.

an accurate probe of antenna excited state dynamics in particles kinetically similar to those studied by other groups.

Several investigators have analyzed the static absorption spectra of PS I core antennae by simulating them as sums of Gaussian components [7, 8]. Owens et al. decomposed the Chl *a* Q_y spectrum of particles with Chl *a*/P700 = 43 into three components centered at 667, 677, and 685 nm with ~20 nm (450 cm^{-1}) bandwidth [8]; Ikegami and Itoh simulated the Q_y spectrum of highly enriched PS I particles as a sum of six Gaussians at 650, 660, 669, 675, 684, and 698 nm, with 1/e bandwidths of 400-600 cm^{-1} [7]. Proposed models for the nature of EET between the different spectral forms of Chl *a* have included the "funnel model" [28], in which excitation migrates sequentially downhill and becomes concentrated in the long-wavelength Chl *a* species, and a more recent model [8] in which excitation becomes rapidly "homogenized" among the different spectral forms. We are unaware of published time-resolved data which support the funnel model for PS I antennae. The PS I fluorescence spectra reported by Owens et al. [8] lend considerable support to the homogenization scenario, because substantial fluorescence is emitted by Chl *a* spectral forms other than the lowest-energy form. An unequivocal test of these models would be a dual-wavelength pump-probe experiment in which antenna Chl *a* absorption is probed at ~660 nm

following excitation at ~685 nm: resolvable uphill EET from the 685 to 660 nm spectral forms in a "homogenization" process would be signalled by a 685 nm photobleaching risetime if excited state absorption is absent. We now analyze whether such risetime behavior would be detectable in the present single-wavelength pump-probe experiments as well. In particular, we consider photobleaching monitored at some wavelength λ_m in a region of spectral overlap between adjacent forms of Chl a, such as Chl a-684 and Chl a-675 in the simulation of ref. [7]. The ratio N^0_{675}/N^0_{684} of initial excited state populations in the two spectral forms will be given by the ratio $\varepsilon_{675}/\varepsilon_{684}$ of their absorption coefficients at λ_m in the Beer's law limit of low excitation power. At early times where negligible excitation trapping has occurred at P700, equilibration of excitation between the spectral forms with uphill and downhill rates k_u and k_d yields the time-dependent excited state populations

$$N_{675}(t) = \frac{k_u(N^0_{675} + N^0_{684})}{k_u + k_d} \left[1 - e^{-(k_u+k_d)t}\right] + N^0_{675} e^{-(k_u+k_d)t} \tag{4.4}$$

$$N_{684}(t) = \frac{k_d(N^0_{675} + N^0_{684})}{k_u + k_d} \left[1 - e^{-(k_u+k_d)t}\right] + N^0_{684}\, e^{-(k_u+k_d)t}$$

The observed photobleaching signal at λ_m is then proportional to

$$D(t) = \Delta\varepsilon_{675}N_{675}(t) + \Delta\varepsilon_{684}N_{684}(t)$$

$$\equiv A[1 - e^{-(k_u + k_d)t}] + Be^{-(k_u + k_d)t} \tag{4.5}$$

where $\Delta\varepsilon_{675}$ and $\Delta\varepsilon_{684}$ are the (ground state - Q_y) differential absorption coefficients at the respective wavelengths. In view of Eqs. 4.4, the difference between the coefficients A and B for the rise and decay contributions to D(t) is then

$$A - B = k_d\varepsilon_{675}\Delta\varepsilon_{684} + k_u\varepsilon_{684}\Delta\varepsilon_{675} - k_u\varepsilon_{684}\Delta\varepsilon_{684} - k_d\varepsilon_{675}\Delta\varepsilon_{675} \tag{4.6}$$

If the excited state absorption is small ($\Delta\varepsilon \simeq \varepsilon$) the condition for observation of risetime behavior (A - B > 0) becomes

$$1 < \frac{\varepsilon_{684}}{\varepsilon_{675}} < \frac{k_d}{k_u} \tag{4.7}$$

The funnel model arises in the special case of essentially irreversible downhill EET, $k_d >> k_u$. In this limit, risetime behavior will be observed in single-wavelength pump-probe experiments at virtually all wavelengths λ_m for which $\varepsilon_{684} > \varepsilon_{675}$. In the contrasting limit where $k_d/k_u = 1$, the excited state populations of the two spectral forms tend toward parity ("homogenization") at equilibrium, and no risetime will be

observed at any wavelength according to Eq. 4.7. No risetime components are in fact observed in any of the isotropic profiles at the wavelengths of strong Chl *a* absorption (660-681 nm) in Table 4.1, and hence we find no evidence of funnel-type EET in the photosystem I core antenna. However, we cannot rule out unresolvably fast irreversible downhill EET (<< 1 ps) on the basis of our data alone; dual-wavelength femtosecond pump-probe studies will help to resolve this question. Gaussian simulations of the Chl *a* Q_y core antenna absorption spectrum predict that the absorption peaks of the various spectral forms are spaced ~150-200 cm^{-1} apart, irrespective of how many Gaussian components are used [7, 8]. This spacing is considerably narrower than the bandwidths (typically 400 cm^{-1}) of the fitted absorption [7, 8] and fluorescence [8] components. Consequently, while the Förster formulation of the EET transition rates between two adjacent Chl *a* spectral forms in terms of an overlap integral involving their absorption and fluorescence spectra [47] predicts that the downhill transition rate will exceed the uphill rate, it does not project that $k_d >> k_u$ in the spirit of irreversible downhill transport.

The rapid (<5 ps) isotropic decays observed at 645-655 nm (Fig. 4.1) indicate that the excited state probed at these wavelengths is dynamically different from the state(s) probed at

660-681 nm, where the isotropic decay is found to be fairly uniform with components of 25-40 ps and 200-250 ps. Since the Chl *b* Q_y transition begins to dominate in this wavelength regime, these ultrafast decays may be associated with excitation migration from Chl *b* to the lower-energy Chl *a* species. Such decays are not readily resolved by time-correlated photon counting ($\gtrsim$ 45 ps instrument function); the fluorescence decay kinetics in *C. reinhardtii* mutants without the PS II reaction center were reported to be insensitive to excitation wavelength even when 95% of the absorption occurred in Chl *b* [12]. Similarly, the fluorescence decay was indistinguishable under 652 and 680 nm excitation of PS I particles containing Chl *b* [8]. Hence, EET from Chl *b* to the core antenna is much more rapid than core antenna excitation decay. Our ultrafast 645 nm isotropic decays (Fig. 4.1 and Table 4.1) serve to lower the upper time limit on excitation migration from Chl *b* to ~2 ps. Furthermore, while the 645-655 nm decays are fast, they are not laser pulse-limited, as is clear from the asymmetry of the profiles (Fig. 4.1); the Chl *b* deexcitation timescale does not appear to be much less than the laser pulse width.

The depolarization lifetimes derived from anisotropic profiles (Fig. 4.4) shows that while excitation may equilibrate rapidly over all of the Chl *a* spectral forms as suggested by

Owens et al. [7], such equilibration does not extend spatially over the entire core antenna. In a scenario consistent with this observation, the core antenna chlorophylls are organized into (nearly) identical subunits, each containing a full complement of spectral forms of Chl a. Rapid equilibration of excitation occurs among the Chl a species inside a subunit, causing the antenna chlorophyll fluorescence spectrum and dynamics to be essentially independent of excitation wavelength [8]. Slower EET (manifested by the depolarization lifetimes in Fig. 4.4 and Table 4.2) occurs between spectrally similar subunits with different orientations. The subunit orientations cannot be random, because the measured anisotropy parameters a in Table 4.2 are nonzero. This model is consistent with the conclusion of Shubin et al. [6] that the PS I core antenna contains several identical clusters of six to eight Chl a pigments each.

The wavelength dependence of the depolarization lifetime was phenomenologically modeled by applying Förster theory [47] to the problem of incoherent EET between like subunits. For definiteness, six Chl a spectral forms were assumed, having Gaussian absorption bands $\varepsilon_i(\omega)$ with positions, bandwidths, and peak heights listed in ref. [7]. The fluorescence spectrum $f_i(\omega)$ of each Chl a species i was similarly modeled as Gaussian, with peak height and bandwidth proportional to and identical to the

peak height and bandwidth respectively of the corresponding absorption component $\varepsilon_i(\omega)$. The fluorescence peak in $f_i(\omega)$ was arbitrarily shifted 3 nm to the red from the absorption peak in $\varepsilon_i(\omega)$. The rate R_{ij} of excitation migration from spectral component i in a subunit to spectral component j in a different subunit was evaluated using [47]

$$R_{ij} = \int f_i(\omega)\varepsilon_j(\omega)\,d\omega/\omega^4 \tag{4.8}$$

and the resulting excitation decay from component i was computed as

$$P_i(t) = \exp[-t\sum_{j=1}^{6} R_{ij}] \tag{4.9}$$

For each pump-probe wavelength $\lambda_m \equiv 1/\omega$, the overall excitation migration rate from the initially pumped subunit then assumes the multiexponential form

$$P(\omega,t) = \sum_{i=1}^{6} \varepsilon_i(\omega) P_i(t) \tag{4.10}$$

These computed decays were then fitted with the single-exponential model function $A\exp(-t/\tau)$ to compute a theoretical depolarization lifetime τ. The results are represented by squares

in Fig. 4.4, where the theoretical lifetime at 675 nm has been normalized to the average experimental lifetime at that wavelength. Similar calculations using parameters resulting from a deconvolution of the PS I-200 absorption spectrum are represented by triangles in Fig. 4.4. The theoretical lifetimes reproduce the qualitative trend of slower depolarization at shorter wavelengths, principally because the absorption coefficients of the components absorbing at the shorter wavelengths (650, 660 nm) are considerably smaller than those of the components absorbing at the longer wavelengths (669, 675, 684 nm). Excessive significance should not be attached to this calculation, owing to the crude assumptions made. The unknown dipole-dipole orientational factors [47] were not considered; the use of Eqs. 4.8-4.10 implicitly assumed that each pigment species i in one subunit is spatially equidistant from all of the pigment species j in the other subunit, so that the transition rates R_{ij} depend only on the pertinent absorption and fluorescence spectra. The physical nature of the Chl a spectral forms (exciton states versus spectrally distinct monomers with different conformations, etc.) was also ignored. Nevertheless, this phenomenological calculation does mimic the essential features of Fig. 4.4, in which the average depolarization lifetime at each wavelength

correlates inversely with the static absorption coefficient at that wavelength (Fig. 4.5).

ACKNOWLEDGEMENTS

We are grateful to W. E. Catron for supporting one of us (T.P.C.) through a Research Fellowship. We thank Professor John Golbeck for isolating the PS I-200 preparations, and we thank Mr. J. Kevin Gillie for evaluating the PS I-200 absorption spectrum in Fig. 4.5. We are indebted to Professors Gerald Small, Kenneth Sauer, John Golbeck, and Graham Fleming for valuable discussions. The Ames Laboratory is operated for the U. S. Department of Energy by Iowa State University under Contract No. W-7405-Eng-82. This work was supported by the Office of Basic Energy Sciences.

REFERENCES

1. Green, B. R. Photosyn. Res. 1988, 15, 3.

2. Golbeck, J. H. Biochim. Biophys. Acta, submitted to reviews in Bioenergetics

3. Wollman, F.-A.; Bennoun, P. Biochim. Biophys. Acta 1982, 680, 352.

4. Haworth, P.; Watson, J. L.; Arntzen, C. J. Biochim. Biophys. Acta 1983, 724, 151.

5. Anderson, J. M.; Brown, J. S.; Lam, E.; Malkin, R. Photochem. Photobiol. 1983, 38, 205.

6. Shubin, V. V.; Karapetyan, N. V.; Krasnovsky, A. A. Photosyn. Res. 1986, 9, 3.

7. Ikegami, I.; Itoh, S. Biochim. Biophys. Acta 1986, 851, 75.

8. Owens, T. G.; Webb, S. P.; Alberte, R. S.; Mets, L.; Fleming, G. R. Biophys. J. 1988, 53, 733.

9. Owens, T. G.; Webb, S. P.; Mets, L.; Alberte, R. S.; Fleming, G. R. Proc. Natl. Acad. Sci. USA 1987, 84, 1532.

10. Gulotty, R. J.; Mets, L.; Alberte, R. S.; Fleming, G. R. Photochem. Photobiol. 1985, 41, 487.

11. Kyle, D. J.; Baker, N.; Arntzen, C. J. Photobiochem. Photobiophys. 1983, 5, 11.

12. Owens, T. G.; Webb, S. P.; Eads, D. D.; Alberte, R. S.; Mets, L.; Fleming, G. R., In "Progress in Photosynthesis Research"; Biggins, J., Ed.; Martinus Nijhoff: The Hague, 1987; Vol. I, p. 83.

13. Lotshaw, W. T.; Alberte, R. S.; Fleming, G. R. Biochim. Biophys. Acta 1982, 682, 75.

14. Searle, G. F. W.; Tamkivi, R.; van Hoek, A.; Schaafsma, T. J. J. Chem. Soc., Far. Trans. 1988, 84, 315.

15. Wittmershaus, B. P.; Berns, D. S.; Huang, C. Biophys. J. 1987, 52, 829.

16. V. A.; Nuijs, A. M.; van Gorkum, H. J.; Smit, J. W. J.; Duysens, L. M. N. Biochim. Biophys. Acta 1986, 850, 319.

17. Il'ina, M. D.; Kravsauskas, V. V.; Rotomskis, R. J.; Borisov, A.-Y. Biochim. Biophys. Acta 1984, 767, 501.

18. Borisov, A.-Y.; Darelius, P. V.; Il'ina, M. D.; Kravsauskas, V. V.; Piskarskas, A. S.; Razjuim, A. P.; Rotomskis, R. J. Mol. (Moscow) 1985, 19, 636.

19. Nuijs, A. M.; Shuvalov, V. A.; van Gorkum, H. J.; Plijter, J. J.; Duysens, L. N. M. Biochim. Biophys. Acta 1986, 850, 310.

20. Bengis, C.; Nelson, N. J. Biol. Chem. 1975, 250, 2783.

21. Takahashi, Y.; Hirota, K.; Katoh, S. Photosyn. Res. 1985, 6, 183.

22. Mullet, J. E.; Burke, J. J.; Arntzen, C. J. Plant Physiol. 1980, 65, 814.

23. Ish-Shalom, D.; Ohad, I. Biochim. Biophys. Acta 1983, 722, 498.

24. Matthews, B. W.; Fenna, R. E. Acc. Chem. Res. 1980, 13, 309.

25. Tronrud, D. E.; Schmid, M. F.; Matthews, B. W. J. Mol. Biol. 1986, 188, 443.

26. Shiozawa, J. A.; Alberte, R. S.; Thornber, J. P. Arch. Biochem. Biophys. 1974, 165, 388.

27. Ikegami, I. Biochim. Biophys. Acta 1976, 449, 245.

28. Seely, G. R. J. Theor. Biol. 1973, 40, 189.

29. Pearlstein, R. M. Photochem. Photobiol. 1982, 35, 835.

30. Hemenger, R. P.; Lakatos-Lindenberg, K.; Pearlstein, R. M. J. Math. Phys. 1972, 13, 1056.

31. Causgrove, T. P.; Yang, S.; Struve, W. S. J. Phys. Chem. 1988, 92, 0000.

32. Philipson, K. D.; Sauer, K. Biochemistry 1972, 11, 1880.

33. Golbeck, J. H., J. Membrane Sci. 1987, 33, 151.

34. Malkin, R.; Ortiz, W.; Lam, E.; Bonnerjea, J. Physiol. Veg. 1985, 23, 619.

35. Lam, E.; Ortiz, W.; Mayfield, S.; Malkin, R. Plant Physiol. 1984, 74, 650.

36. Golbeck, J. H. Methods Enzymol. 1980, 69, 129.

37. Anfinrud, P., Struve, W. S., Rev. Sci. Instrum. 1986, 57, 380.

38. Fleming, G. R. "Chemical Applications of Ultrafast Spectroscopy"; Oxford University Press: London, 1986; p. 66.

39. Geacintov, N. E.; Breton, J.; CRC Crit. Rev. Plant Sci. 1987, 5, 1.

40. Holzwarth, A. R.; Haehnal, W.; Wendler, J.; Suter, G.; Ratajczak, R. In "Advances in Photosynthesis Research"; Sybesma, C., Ed.; Martinus Nijhoff: The Hague, 1984; p. 73.

41. Kamagawa, K.; Morris, J. M.; Takagi, Y.; Nakashima, N.; Yoshihara, K.; Ikegami, I. Photochem. Photobiol. 1983, 37, 207.

42. van Grondelle, R.; Amesz, J. In "Light Emission by Plants and Bacteria"; Govindjee; Amesz, J.; Fork, D. C., Eds.; Academic Press: New York, 1986; p. 213.

43. Causgrove, T. P.; Bellefeuille, S. M.; Struve, W. S.; J. Phys. Chem. 1988, 92, 0000.

44. Anfinrud, P. A.; Hart, D. E.; Hedstrom, J. F.; Struve, W. S. J. Phys. Chem. 1986, 90, 2374.

45. Gillbro, T.; Sandstrom, A.; Spangfort, M.; Sundstrom, V.; van Grondelle, R. "Technical Digest", Sixth International Conference on Ultrafast Phenomena, Mt. Hiei, Kyoto, Japan, July 1988.

46. Gillie, J. K.; Small, G. J.; Golbeck, J. H. J. Phys. Chem., in press.

47. Shipman, L. L.; Housman, D. L. Photochem. Photobiol. 1979, 29, 1163.

SECTION V. REVIEW OF CRYSTAL AND MOLECULAR STRUCTURES OF PORPHYRINS

INTRODUCTION

The biological functions of porphyrins and their derivatives are so important that the study of porphyrin complexes has become a research field in itself. Structures of porphyrins and metalloporphyrins are reviewed in this chapter.

Since 1963, a large number of crystal and molecular structures of porphyrins and metalloporphyrins has been determined by three-dimensional x-ray diffraction. Based on the coordination number of the central metal, they can be grouped into four categories: four-coordinate, five-coordinate, six-coordinate, and eight-coordinate metal porphyrins[1-23]. The structures of the porphyrins themselves can be subdivided into two parts: the porphinato core and the peripheral substituents. The porphinato core is common to all porphyrin compounds, while the peripheral substituents are different from one compound to another. Most of the discussion in this chapter will be concentrated on a comparision of structures of the porphinato cores.

Figure 5.1 gives a diagram of the carbon-nitrogen skeleton in the porphinato core of a metalloporphyin. The metal is centered at Ct. The notation C_a, C_b and C_m for the three chemically distinctive classes of carbon atoms is employed throughout this chapter.

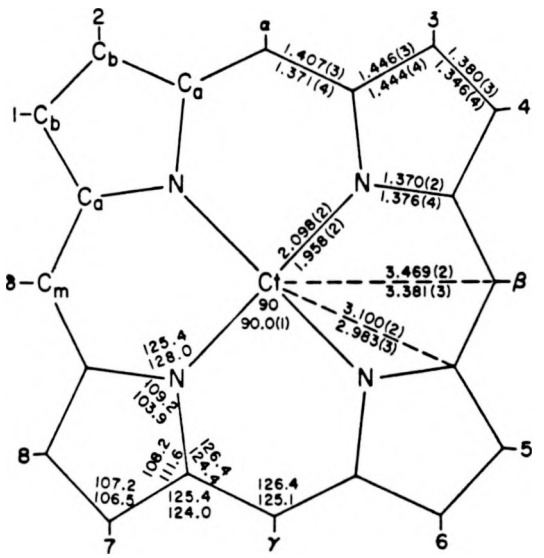

Figure 5.1 Diagram of the carbon-nitrogen skeleton in the porphinato core of a metalloporphyrin which retains real or effective D_{4h} geometry. Values of the principal radii (Å), bond lengths (Å), and angles (°) in $(Cl_2)Sn(TPP)$ and in the planar form of Ni(OEP) are centered on the diagram; the upper datum in each pairing is the value in $(Cl_2)Sn(TPP)$.

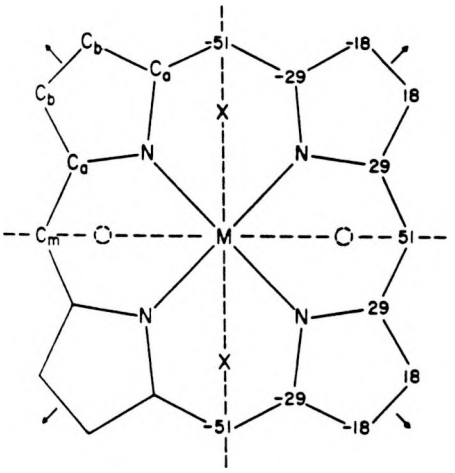

Figure 5.2 Diagram in projection of the porphinato core in the ruffled form of the Ni(OEP) molecules a slightly idealized to D_{2d} symmetry. The pair of vertical mirror planes are indicated by broken lines,the equatorial two-fold axes by arrows. In the right-hand half of the diagram, the symbol for each carbon atom is replaced by the displacement of the atom, in units of 0.01 Å, from the mean plane of the core.

STRUCTURES OF METALLOPORPHYRINS

1. Four-coordinate metalloporphyrins

Table 5.1 summarizes the structural parameters for four-coordinate metalloporphyrins. The conformation of the four-coordinate porphinato core can be characterized as either planar or S_4-ruffling. The planar conformation is required in the highest symmetry case, D_{4h} (Fig. 5.1). A D_{2d} (S_4) ruffling of the core can be defined by the rotation of the planar pyrrole ring and its attached pair of C_a-C_m bridging bonds through an angle ϕ around the twofold axis along the M-N bond (Fig. 5.2). The C_m carbon atoms are displaced alternately above and below the mean plane of the core in agreement with S_4 symmetry. A D_{2d} ruffling of the core could allow a shortening of the M-N bonds (metal-nitrogen) while not necessarily requiring substantial alteration in other bond distances in the core. See, for example, NiEOP in Table 5.1.

2. Five-coordinate metalloporphyrins

Table 5.2 summarizes the structural parameters for five-coordinate metalloporphyrins. Square-pyramidal coordination (C_{4v} symmetry) is a characteristic of the five-coordinate

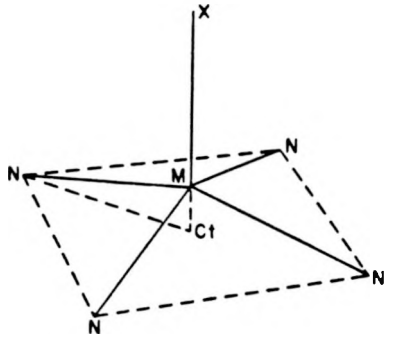

Figure 5.3 A diagram of the square-pyramidal coordination group for five-coordinate metalloporphyrins.

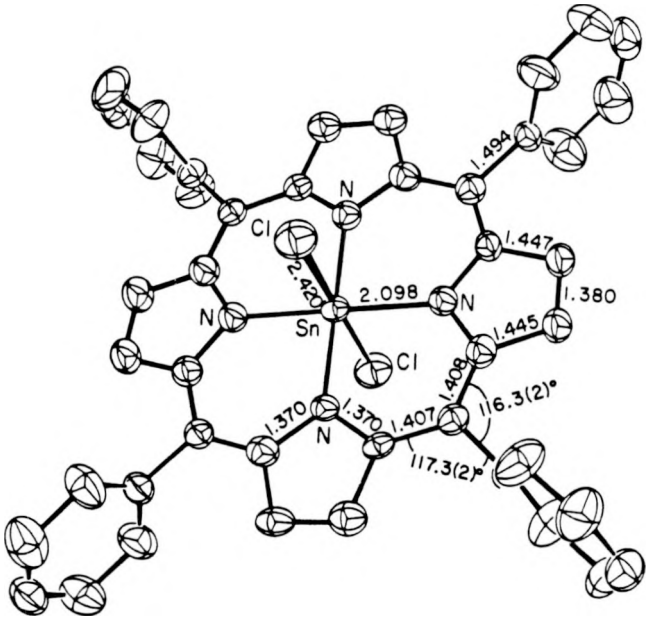

Figure 5.4 Computer-drawn model of $(Cl)_2Sn(TPP)$, a six-coordinate porphyrin molecule.

metalloporphyrins. The coordinated atom (X) of the axial ligand is positioned at the apex of the square-pyramidal coordination group (Fig. 5.3). The net doming (the deviation from planar symmetry) of the porphinato core can be specified by the separation of the mean plane of the porphinato nitrogen atoms (P_N) from the mean plane of the porphine skeleton (P_C). This separation is generally small with $P_N...P_C \leq 0.05$ Å.

3. Six-coordinate metalloporphyrins

Table 5.3 summarizes the structural parameters for six-coordinate metalloporphyrins. The basic coordination group of the six-coordinate metalloporphyrin is that of an octahedron with an axial ligand on either side of the porphinato plane (Fig. 5.4). The conformation of the six-coordinate porphinato core is similar to the four-coordinate: either planar or S_4-ruffling. The metal-axial ligand bond distance is influenced by the steric interaction of the axial ligand atoms with atoms of the porphinato core. Also steric interations can cause a stretching of the M-N bond.

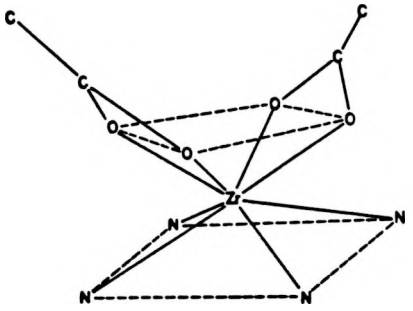

Figure 5.5a A schematic diagram of the square antiprism in $(OAc)_2ZrOEP$.

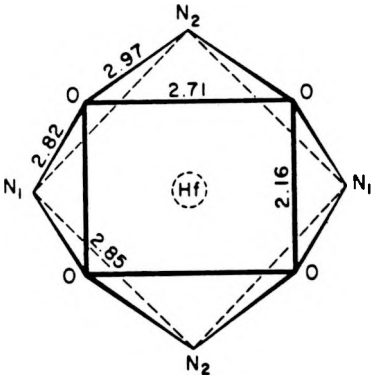

Figure 5.5b Diagram illustrating the C_{2v} geometry of the coordination group in the $(OAc)_2Hf$-(OEP) molecule. Hf-P_N: 1.012(3) Å; Hf-P_O: 1.480(3) Å. $(Hf\text{-}N)_{av}$=2.257(3), and Hf-O=2.278(3) Å.

Table 5.1 Structure parameters for four-coordinate metalloporphyrins

			M-N	N-C_a	C_a-C_m	C_a-C_b	C_b-C_b	M-C_m
Ruffle								
FeTPP	d^6Fe	1	1.972(4)	1.382(6)	1.392(6)	1.436(6)	1.353(6)	3.395
NiOEP	d^8Ni	0	1.929(3)	1.387(4)	1.373(5)	1.449(5)	1.362(5)	3.355(4)
CuTPP	d^9Cu	1/2	1.981(1)	1.383(12)	1.358(13)	1.461(13)	1.337(14)	
PdTP	d^8Pd	0	2.009(9)	1.369(13)	1.386(20)	1.440(14)	1.346(16)	
NiDeut	d^8Ni	0	1.960	1.383	1.375	1.446	1.350	
$AuTPP^+$	d^8Au	0	2.00(2)					
CoTPP	d^7Co	1/2	1.949					
NiTPP	d^8Ni	0	1.928					
Planar								
NiOEP	d^8Ni	0	1.958(2)	1.376(4)	1.371(4)	1.443(4)	1.346(4)	
CuTPrP	d^9Cu	1/2	2.005	1.383	1.382	1.449	1.345	
AgTPP	d^9Ag	1/2	2.082	1.368	1.410	1.447	1.350	
MnTPP	d^5Mn	5/2	>2.08					
CrTPP	d^4Cr	2	2.033					
ZnTPP	d^{10}Zn	0	2.036					

Angles	NMN	C_aNC_a	MNC_a	NC_aC_m	NC_aC_b	$C_bC_aC_m$	$C_aC_mC_a$	$C_aC_bC_b$
FeTPP	90.01(4)	105.4(3)	127.3(3)	127.3(4)	110.2(3)	124.5(3)	123.5(3)	107.1(4)
NiOEP	90.0(0)	105.1(3)	127.4(2)	124.0(2)	110.6(2)	125.0(2)	124.1(2)	106.8(3)
AuTPP	90.275							
CuTPP	90.0	107.8(7)	125.9(6)	127.3(8)	107.9(8)	124.8(8)	123.1(8)	108.1(9)
PdTPP	90.0	106.4(10)	126.8(8)	124.9(11)	109.5(10)	125.1(11)	125.0(11)	107.3(10)
NiDeut	90.0	104.4	127.8	125.3	111.0	123.7	123.9	106.6
NiOEP	90.0(1)	103.9(2)	128.0(2)	124.4(3)	111.6(3)	124.1(3)	125.1(3)	106.5(3)
Cu(TPrP)		106.5		126.6	109.3		122.8	107.4
Ag(TPP)		108.7		126.5	108.2		125.6	107.5

Table 5.2 Structure parameters for five-coordinate metalloporphyrins

	M-N	N-Ca	C_a-C_m	C_a-C_b	C_b-C_b	M-P_N	M-X
$ZnTTPClO_4$	2.076(9)	1.35(1)	1.40(1)	1.43(1)	1.35(2)		2.079(8)
H_2OZnTPP	2.05(0.01)	1.38(1)	1.42(1)	1.43(1)	1.37	0.20	2.20(6)
CO(1-Me-Im)(OEP)	1.96(1)	1.37(2)	1.39(2)	1.45(3)	1.34(1)	0.13	2.15(1)
CoFeTPP	2.049(9)	1.38(1)	1.40(1)	1.45(1)	1.38(1)	0.383	2.19(1)
PyZnTPyP	2.073(2)	1.369(2)	1.406(2)	1.447(2)	1.355(3)	0.33	
(2-Me(M)FeTPP	2.086(4)	1.377(7)	1.403(7)	1.447(7)	1.347(7)	0.42	2.143(4)
ONCoTPP	1.978(4)	1.376(4)	1.394(3)	1.430(1)	1.360		1.833
ONFeTPP	2.001	1.379(3)	1.388(4)	1.434(4)	1.345(4)	0.21	1.717
(H_2O)MgTPP	2.072(1)	1.376(1)	1.415	1.431(1)	1.360(1)	0.273	2.099
(H_2O)MgT(OME)P	2.086(7)	1.373	1.406	1.440	1.364	0.39	2.078
$ZnTPPClO_4$	2.076(9)	1.35(1)	1.40	1.43(1)	1.35(2)		

	NMN	MNC_a	C_aNC_a	NC_aC_m	NC_aC_b	$C_bC_aC_m$	$C_aC_mC_a$	$C_aC_bC_b$
$ZnTPPClO_4$	88.4	125.5(7)	107.6(5)	126.1(8)	109.4(10)	124.4(12)	124.7(4)	106.9(13)
H_2OZnTPP	90.0	127.7(6)	105.4(7)	124.4(9)	110.5(8)	125.5(9)		107.8(8)
PyZnTPyP	88.5(1)	126.3(2)	106.7(2)	125.7(2)	109.8(3)	124.5(3)	125.5(3)	106.9(3)
ClFeTPP	90.0	126.5(8)	105.6(9)	126.0(11)	110.7(10)	123.8(12)		106.8(12)
ONFeTPP	92.75	127.1(2)	105.3	126.0(2)	110.1(2)		123.5(2)	107.2(2)
ONCoTPP	91.3	127.7(2)	104.6(2)	126.0(3)	111.2(3)	122.6(3)	122.6	106.6(3)
Co(1-Me-Im)OEP	89.7		103.0(1)	126.0(2)	112.0(2)	122.0(2)	122.0(1)	106.0(2)
(H_2O)MgTPP	89.0		106.1		110.0	125.3		107.1
(H_2O)MgT(OME)P	88.1	126.4(6)	106.3	126.0(6)	109.3(8)	124.7(8)		108.3(8)

Table 5.3 Structure parameters for six-coordinate metalloporphyrins[a]

	M-N	$N-C_a$	C_a-C_m	C_a-C_b	C_b-C_b	M-X	
$(Cl)_2SnTPP$	2.098(2)	1.370(2)	1.407(3)	1.446(3)	1.380(3)	2.420(1)	
$(Cl)_2SnOEP$	2.082(5)	1.379(7)	1.386(8)	1.437(8)	1.368(8)	2.453(2)	
$[(Im)_2Fe(TPP)]Cl$	1.989(4)	1.378(7)	1.392(8)	1.437(8)	1.350(9)	1.957(4)	~ 1.991(5)
$(Pip)_2Fe(TPP)$	2.004(3)	1.384(4)	1.396(5)	1.444(5)	1.347(6)	2.127(3)	
$(Pip)_2Co(TPP)$	1.987(2)	1.381(2)	1.392(2)	1.444(3)	1.345(3)		
$[(Pip)_2Co(TPP)]NO_3$	1.979(3)	1.384(4)	1.389(5)	1.435(5)	1.356(5)	2.060(3)	
$(3\text{-}Pic)_2Co(OEP)$	1.992(1)	1.374(2)	1.381(2)	1.449(2)	1.355(3)	2.386(2)	
$[(Im)_2Co(TPP)]OAC$	1.982(11)	1.390(6)	1.378(8)	1.433(5)	1.340(8)	1.93(2)	

	NMN	MNC_a	C_aNC_a	NC_aC_m	NC_aC_b	$C_bC_aC_m$	$C_aC_mC_a$	$C_aC_bC_b$
$(Cl)_2SnTPP$	90	125.4(1)	109.2(2)	126.4(2)	108.2(2)	125.4(2)	126.4(2)	107.2(2)
$(Cl)_2SnOEP$	90.0(2)	125.9(3)	108.2(5)	124.4(5)	108.3(5)	127.3(6)	129.5(6)	107.6(5)
$[(Im)_2Fe(TPP)]Cl$	90.0(2)	126.9(2)	106.1(4)	126.0(5)	109.7(5)	124.2(5)	123.1(5)	106.7(5)
$(Pip)_2Fe(TPP)$	90.0(1)	127.2(2)	105.2(3)	125.6(3)	110.2(3)	124.1(3)	124.1(3)	107.2(3)
$(Pip)_2Co(TPP)$	90.0(1)	127.4(1)	104.8(1)	125.8(2)	110.5(2)	123.6(2)	123.4(2)	107.0(2)
$[(PrP)_2Co(TPP)]NO_3$	90.0(1)	127.5(2)	104.9(3)	125.9(3)	110.5(3)	123.6(3)	123.0(3)	107.0(3)
$(3\text{-}Pic)_2Co(OEP)$	90.0(1)	127.5(1)	105.0(1)	124.5(2)	111.0(2)	124.5(2)	125.8(2)	106.5(2)
$[(Im)_2Co(TPP)]OAc$		127.3(5)	105.3(14)		109.7(9)	124.6(7)	123.9(6)	

[a]The figure in parentheses following each datum is the usual estimated standard deviation given by the structure analysis for each individual parameter within the chemical class.

4. Eight-coordinate metalloporphyrins

The coordinate polyhedron in eight-coordinate metalloporphyrins is approximately a square antiprism (Fig. 5.5). The doming of the core closes to C_{2v} geometry. The amount of the doming is measured by the perpendicular displacement between the mean plane P_N and the mean plane of the β-carbons of the pyrrole rings P_{cb}.

From the above discussion, we can see that the conformation of porphinato core could be: planar, ruffling (S_4) or doming. Quite a few factors effect the stereochemistry of the metalloporphyrin core: spin state of the central metal ion, mutual interactions of the metal atom, porphinato core, and any axial ligand or ligands which may be present, and packing constraints in the crystal.

STRUCTURES OF CHLOROPHYLLS

The chlorophylls have many structural features similar to porphyrins, and yet they contain structural entities unique only to this class of compounds.

The most important structural difference between chlorophylls and porphyrins is the presence of an alicycle Ring V (Fig. 5.6), which has an enormous effect upon the solubility and sorbability of chlorophylls as compared to the porphyrins.

Several crystal structures of chlorophyll derivatives[24-28] have been determined by x-ray diffraction. In all of these structures, the central magnesium is bonded to the four nitrogen atoms and also to a water molecule as a fifth ligand in approximately square-pyramidal co-ordination. This water molecule is hydrogen-bonded to the ring V carbonyl oxygen of a translationally equivalent molecule, leading to the formation of characteristic one-dimensional stacks of partially overlapping chlorin rings (Fig. 5.7). The summary of the structural parameters for these compounds is shown in Table 5.4.

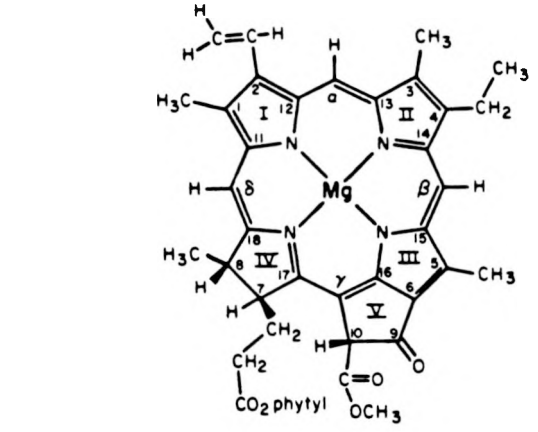

Chlorophyll a

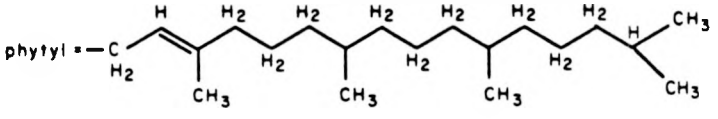

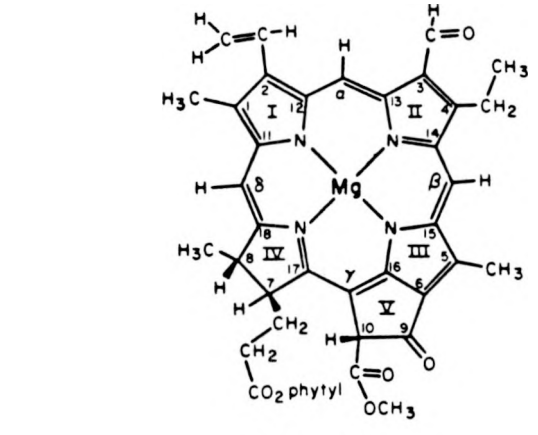

Chlorophyll b

Figure 5.6 Molecular structures of chlorophyll a and chlorophyll b with designations of the carbon atoms (nemerals and Greek letters).

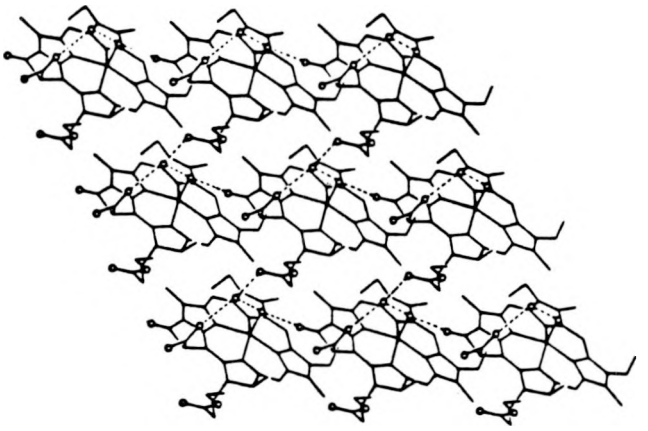

Figure 5.7a The packing of one layer in the structure of ethyl chlorophyllide a dihydrate view down the 3_1 axis.

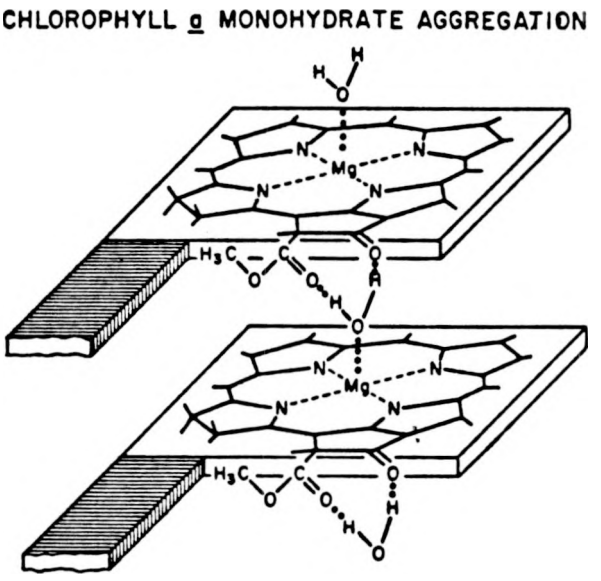

Figure 5.7b Structure illustrating the chlorophyll-water-chlorophyll interaction. The dimensions of the ring and the phytyl chain are not to scale.

Table 5.4 Crystal data of chlorophyllides

Compound	Space group	Cell dimensions	$Mg-P_N$	$Mg-OH_2$
Methyl chlorophyllide dihydrate[26]	$P2_1$	a = 8.76 Å b = 25.86 Å c = 8.47 Å β = 119.2° z = 2	0.34 Å	2.03 Å
Ethyl chlorophyllide dihydrate[28,24]	$P3_1$	a = b = 8.87 Å c =38.05 Å z = 3	0.39 Å	2.035 Å
Methyl pyrochlorophyllide monohydrate[27]	$P2_12_12_1$	a = 23.01 Å b = 19.08 Å c = 8.42 Å z = 4	0.4 Å	2.03 Å

The x-ray crystal structure of bacteriochlorophyll (Bchl.) a-proteins from green photosynthetic bacterium Prosthecochloris aestuarii has been determined by Fenna and Matthew[30]. Each subunit of the Bchl-protein contains a core of seven bacteriochlorophyll a molecules enclosed within an envelope of protein (Fig. 5.8). The central magnesium ion of each Bchl is five-coordinated and about 0.4 Å out of plane toward the liganting group, as found in the crystal structure of ethyl chlorophyllide a. For Bchls 1,3,4,6, and 7 the magnesium ligand appears to be a histidine side chain; for Bchl 5 the ligand seems to be peptide oxygen of the protein backbone;

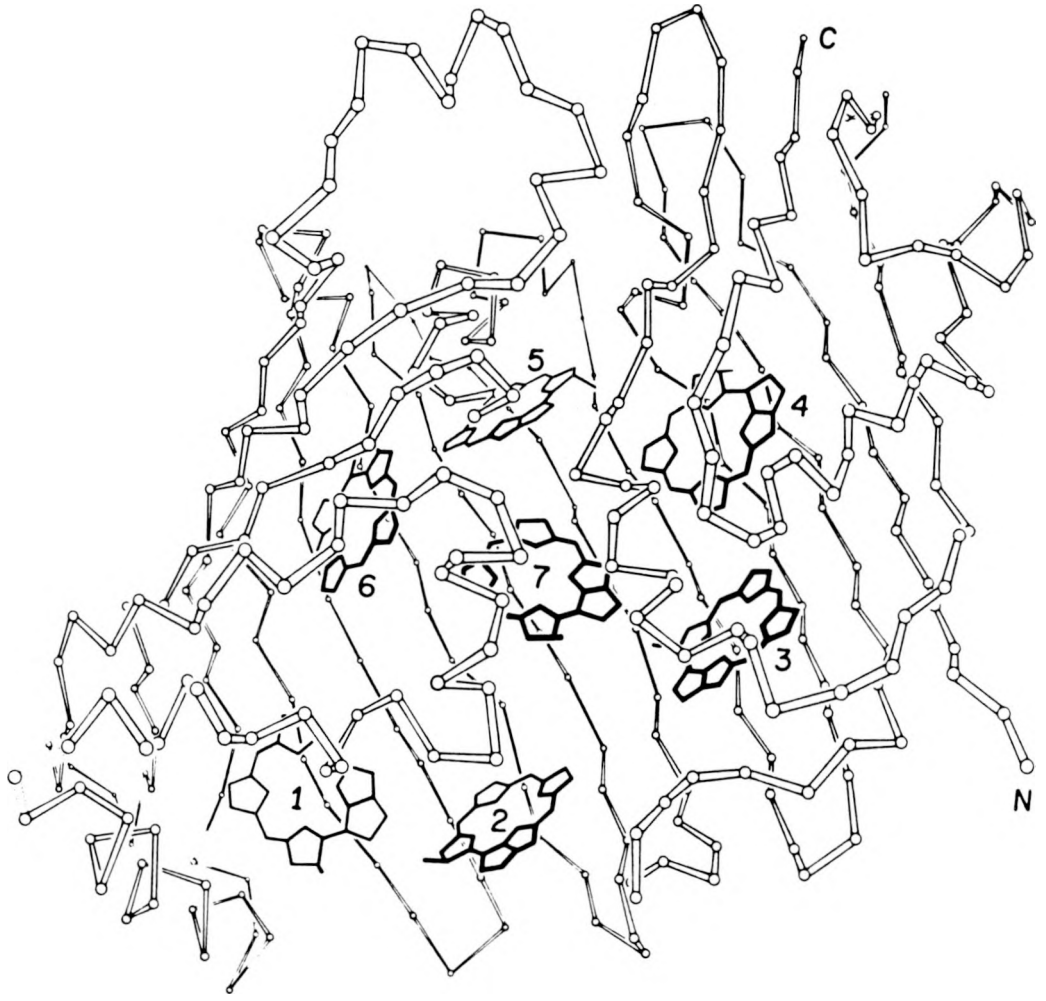

Figure 5.8 One subunit of the bacteriochlorophyll protein showing the seven bacteriochlorophylls enclosed within an envelope of protein. The phytyl tails of each bacteriochlorophyll have been omitted for clarity.

and for Bchl 2 the ligand appears to be a water molecule. The seven phytyl chains make extensive van der Waals interactions with each other and tend to cluster together to form an inner hydrophobic core in the center of the subunit.

AGGREGATION OF PORPHYRINS AND CHLOROPHYLLS

The aggregation of porphyrins and metalloporphyrins has been studied for several decades[31]. Basically three types of aggregation in these compounds are proposed: face to face (Fig. 5.9), μ-oxo oligomers (Fig. 5.10), and metal-metal bonds. Why do porphyrins readily form oligomers? The unsaturation of the central metal, the large porphinato plane which can provide appreciable contact area between porphyrin molecules, and π-π interaction seem to be the most important factors.

The aggregation of chlorophylls has special significance in photosynthesis[32]. It is responsible for the anomalous red shift of chlorophyll in vivo, and probably provides a structural model for energy transfer in photosynthesis. Several aggregation models for Chl/Bchl have been proposed. They are mainly devided into two categories depending on electron donation to Mg from H_2O or from Chl itself. Fischer et al[29] and Strouse[24] have suggested that chlorophyll aggregation in photosynthetic organism is a chlorophyll-water adduct based on the X-ray structures of chlorophyllides.

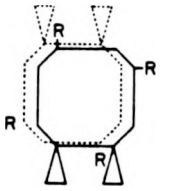

Figure 5.9 Schematic representation of dicarboxylic acid porphyrin dimer. Triangles represent propionic acid side chains; R represents at the 2,4-positions.

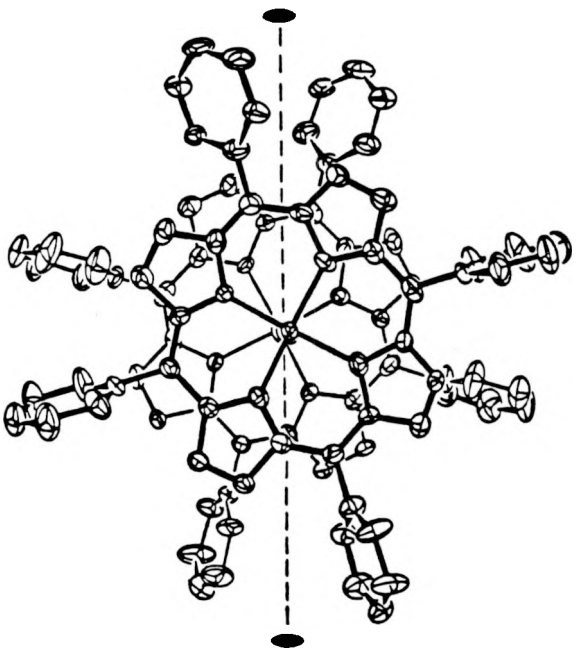

Figure 5.10 Computer-drawn model in perspective of the $O(FeTPP)_2$ molecule. The twofold axis passes through the bridging oxo oxygen atom, requires structural equivalence of the upper and lower halves of the oligomer.

In their model, Chl. molecules are linked together via a water molecule that simultaneously coordinates to the Mg of one of the Chl a molecules and forms hydrogen bonds to both the ring V keto C=O and the carbomethoxy C=O of the other Chl a. Katz, Shipmen et al[32,33] proposed that Chl aggregation in vivo is caused by interactions between central Mg of a Chl and O in the ring V keto C=O group of a neighboring Chl. (self-aggregation). Which model is true in vivo? We think it appears to be dependent on the environment of the Chl in vivo and the availability of an electron donor. Recently more evidence shows that the Chl-protein complex is the basic model for Chl arrangement in photosynthetic organisms, only in the chlorosome of some bacteria (e.g. green, brown bacteria), dose Bchl aggregation play an important role in arrangement of Bchl. In the Chl-protein complexes, the electron donors could be from side chains or/and from the backbone of the protein, and solvent molecules. At the moment it appears that more investigators prefer the Chl/Bchl-water adduct as a model for the dimer in the photo reaction center, and Bchl self aggregation as an antenna model in chlorosome of bacteria.

REFERENCES

1. Collman, J. P.; Hoard, J. L.; Lang, G.; Radonovich, L. J.; Reed, C. A. J. Amer. Chem. Soc. 1975, 97, 2676.

2. Meyer Jr., E. F. Acta Crystallogr. 1972, B28, 2162.

3. Fleischer, E. B.; Miller, C. K.; Webb, L. E. JACS. 1964, 86, 2342.

4. Hamor, T. A.; Caughey, W. S.; Hoard, J. L. JACS. 1965, 87, 2305.

5. Cullen, D. L.; Meyer Jr., E. F. JACS. 1974, 96, 2095.

6. Moustakali, I.; Tulinsky, A. JACS. 1973, 95, 6811.

7. Spaulding, L. D.; Eller, P. G.; Bertrand, J. A.; Felton, R. H. JACS., 1974, 96, 982.

8. Glick, M. D.; Cohen, G. H.; Hoard, J. L. JACS. 1967, 89, 1996.

9. Collins, D. M.; Hoard, J. L. JACS. 1970, 92, 3761.

10. Hoard, J. L.; Cohen, G. H.; Glick, M. D. JACS. 1967, 89, 1992.

11. Little, R. G.; Ibers, J. A. JACS. 1974, 96, 4452.

12. Timkovich R.; Tulinsky, A. JACS. 1969, 91, 4430.

13. Yang, S.; Jacobson, R. A. to be submitted

14. Scheidt, W. R.; Frisse M. E. JACS. 1975, 97, 17.

15. Scheidt, W. R.; Hoard, J. L. JACS. 1974, 96, 8281.

16. Collins, D. M.; Scheidt, W. R.; Hoard, J. L. JACS. 1972, 94, 6689.

17. Cullen, D. L.; Meyer Jr., E. F. Acta Crystallogr. 1973, B29, 2507.

18. Countryman, R.; Collins, D. M.; Hoard, J. L. JACS. 1969, 91, 5166.

19. Radonovich, L. J.; Bloom, A.; Hoard, J. L. JACS. 1972, 94, 2066.

20. Scheidt, W. R. JACS. 1974, 96, 84.

21. Scheidt, W. R.; Cunnigham, J. A.; Hoard, J. L. JACS. 1973, 95, 8289.

22. Little, R. G.; Ibers, J. A. JACS. 1974, 96, 4440.

23. Lauher, J. W.; Ibers, J. A. JACS. 1974, 96, 4447.

24. Chow, H.; Serlin, R.; Strouse, C. E. JACS. 1975, 97, 7230.

25. Serlin, R.; Chow, H.; Strouse, C. E. JACS. 1975, 97, 7237.

26. Kratky, C.; Dunitz, J. D. Acta Cryst. 1977, B33, 545.

27. Kratky, C. Isenring, H. P.; Dunitz, J. D. Acta Cryst. 1977, B33, 547.

28. Kratky, C.; Dunitz, J. D. Acta Cryst. 1975, B31, 1586.

29. Fischer, M. S.; Templeton, D. H.; Zalkin, A.; Calvin, M. JACS. 1972, 94, 3613.

30. Matthews, B. W.; Fenna, R. E.; Bolognesi, M. C.; Schmid, M. F. J. Mol. Biol. 1979, 131, 259.

31. The Porphyrins; Dolphin Ed.; V.5, P. 303

32. The Porphyrins; Dolphin Ed.; V.5, P. 401

33. Shipman, L. L.; Cotton, T. M.; Norris, J. R.; Katz, J. J. Proc. Natl. Acad. Sci. 1976, 1976, 73, 1791.

SECTION VI. SYNTHESIS, CRYSTAL STRUCTURE AND MOLECULAR MODELING OF AQUO MAGNESIUM TETRA-(METHOXYPHENYL)PORPHYRIN

SYNTHESIS, CRYSTAL STRUCTURE AND MOLECULAR MODELING OF AQUO MAGNESIUM TETRA-(METHOXYPHENYL)PORPHYRIN

Shumei Yang and Robert A. Jacobson

Department of Chemistry and Ames Laboratory-USDOE

Iowa State University, Ames, Iowa 50011

INTRODUCTION

The structures of magnesium-containing porphyrins are of considerable interest because of their relationship to chlorophyll and its related compounds; detailed knowledge of such structures can aid in the understanding of photosynthesis spectroscopy and its relation to pigment arrangement. The structure of ethyl chlorophyllide *a* dihydrate has been used as a model for the different spectral forms of chlorophyll[1]. It has been proposed that bacteriochlorophyll *c* oligomers (extracted from Chlorobiaceae) are a good model for BChl *c* in the antennae of green bacteria (Bystrova[2] et al., 1979; Smith[3] et al., 1983; Brune[4] et al., 1987). In order to obtain further structural data on Mg-porphyrin compounds which can be used to provide additional insight on chlorophyll aggregation in vivo, we chose H_2T(OME)PP, an oxygen containing porphyrin, as a ligand, synthesized (H_2O)MgT(OME)PP, and determined the crystal and molecular structure of 5,10,14,20-tetrakis(4-methoxyphenyl)porphyrin magnesium(II)monohydrate. The intermolecular hydrogen bonding observed in this structure gives further insight to help explain the chlorophyll aggregation <u>in vivo</u>.

EXPERIMENTAL

5,10,14,20-tetrakis(4-methoxyphenyl)-21H,23H-porphine(97%), $H_2T(OME)PP$, was purchased from Aldrich Chemical Company. All other reagents were of analytical grade.

The magnesium(II) complex was prepared by using Adler's method[5]. Approximately 100 ml of N,N'-dimethylformamide was brought to reflux temperature in a flask on a stirring hot plate. Then 0.238 g of $H_2T(OME)PP$ was added. After the porphyrin had dissolved completely, ten times the stoichiometric amount of $MgCl_2$ (0.3 g) was added. Three hours later, the reaction was checked by UV spectrometer. In contrast to Alder's earlier findings with other porphyrins, the free porphyrin's red fluorescence was still significant. Another 0.1 $MgCl_2$ was added and the reaction proceeded overnight. The completion of reaction was then verified spectrophotometrically. After concentrating the solution's volume to 10 ml, 200 ml of water was added. The suspension was filtered through a celite pad, washed with water, and dried. The product was washed from the celite with $CHCl_3$ and evaporated to dryness. Finally the product was purified by column chromatography on Al_2O_3 with $CHCl_3$; removal of the solvent under reduced pressure yielded 0.17 g purple solid. Purity of the complex was checked by its ^1H NMR spectrum.

A single crystal of $(H_2O)MgT(OME)PP.HCCl_3$ suitable for X-ray structure determination was grown by slow diffusion of octane into saturated $CHCl_3$ solution of $(H_2O)MgT(OME)PP$.

A purple crystal having approximate dimensions of 0.35 x 0.30 x 0.30 mm was mounted on a glass fiber using epoxy cement and attached to a standard goniometer head. X-ray intensity data were collected at -80 °C on a four-circle RIGAKU X-ray diffractometer using graphite- monochromated Mo K_α radiation from a rotating anode source. Three standard reflections were monitored every 150 reflections measured, and their intensities showed good stability of the complex throughout data collection. The unit cell was found to be monoclinic, and lattice constants were determined to be a = 15.966(5), b = 9.192(1), c = 14.882(4) Å, β = 100.38(2)° from least-squares refinement of the positions of 15 high angle reflections. A total of 4614 intensities were measured, corresponding to those in the two octants (hkl, hk$\bar{l}$) with $2\theta \geq 50°$, and 1297 unique "observed" reflections having $I > 3\sigma(I)$ were used in the structure determination and refinement. Further details are given in Table 6.1.

Table 6.1 Crystallographic data for $(H_2O)MgT(OMe)PP$

Empirical Formula	$MgO_{12}N_4C_{48}H_{38}Cl_3$
Formula Weight	773.14
Crystal Color, Habit	purple, platelet
Crystal Dimensions (mm)	0.350 X 0.300 X 0.300
Crystal System	monoclinic
No. Reflections Used for Unit Cell Determination (2θ range)	25 (22.5 - 39.3°)
Omega Scan Peak Width at Half-height	0.41
Lattice Parameters:	a = 15.966 (5)Å b = 9.192 (1)Å c = 14.882 (4)Å β = 100.38 (2)° V = 2148.2 (9)Å^3
Space Group	I2 (#5)
Z value	2
D_{calc}	1.195 g/cm 3
F_{000}	808
$\mu_{(MoK\alpha)}$	0.86 cm^{-1}
Diffractometer	Rigaku AFC6R
Radiation	MoKα (λ = 0.71069 Å)
Temperature	-80°C
Crystal to Detector Distance	40 cm
Scan Type	ω-2θ
Scan Rate	16.0°/min (in omega) (2 rescans)
Scan Width	(1.31 + 0.30 tanθ)°
$2\theta_{max}$	65.2°
No. of Reflections Measured	Total: 4614 Unique: 4454 (R_{int} = .102)
Corrections	Lorentz-polarization Absorption (trans. factor: 0.96~1.00)
Structure Solution	Direct Methods
Refinement	Full-matrix least-squares
Function Minimized	$\Sigma w (\|Fo\| - \|Fc\|)^2$
Least-squares Weights	$4Fo^2/\sigma^2(Fo^2)$
p-factor	0.03
Anomalous Dispersion	All non-hydrogen atoms
No. Observations (I>3.00σ(I))	1297
Residuals: R; R_w	0.068; 0.070
Maximum, Minimum Peak in Final Diff. Map	0.37 e$^-$/Å^3, -0.37 e$^-$/Å^3

STRUCTURE ANALYSIS

The only observed extinctions were: hkl, h+k+l=2n+1; this is consistent with space groups I2, Im or I2/m. Since two molecules per cell is indicated by density considerations, choice of one of those three space groups would require C_2, C_s or C_{2h} molecular symmetry. A direct method program[6] was used to determine the structure in each of the three space groups. The best result was obtained in space group I2, as the positions of the phenyl groups were found to deviate appreciably from the plane of the porphyrin and the position of the magnesium was found to be displaced above the porphyrin plane.

The structure was then refined using successive least-squares computations with intermediate difference electron density calculations. Full-matrix least-squares refinement with all atoms isotropic yielded a crystallographic residual of R=0.17. A subsequent structure factor and electronic density map calculation showed additional atom peaks which appeared to result from the inclusion of a $CHCl_3$ solvent molecule (disordered) in the crystal. Addition of these atoms reduced R to 0.11. Anisotropic refinement brought R value down to 0.08. Hydrogen atoms were partially located on a difference map and partially included from ideal position calculations. The final value of R was 0.068 and R_w 0.070, with shifts to parameter ratio less than 0.11. The maximum peak in the final electron density map was

0.37 $e^-/Å^3$. Neutral atom scattering factors were taken from the International Tables for X-ray Crystallography and modified for the real and imaginary parts of anomalous scattering[7-9]. All calculations were performed on a VAX computer using the programs TEXSAN for structure solution, refinement and least squares plane calculations, and ORTEP for drawing molecular diagrams.

MOLECULAR MECHANICS CALCULATIONS

An independent calculation of the molecular structure was carried out using a molecular mechanics program[10]. The porphyrin moiety was sketched in on the computer screen and the magnesium atom was placed at the center of the ligand, albeit with a small out of plane displacement. A water molecule was placed above the magnesium to complete the square pyramid geometry around the metal. The atomic positions were then allowed to adjust using essentially an MM2 algorithm[11] to minimize the energy. In order to be reasonably confident that the result did not correspond to merely a local minimum, the process was repeated a number of times using different starting configurations.

Two alternate starting conformations were also tested. The first had the same atomic configuration as noted above but with the omission of the water molecule. The other conformation also omitted the water molecule and placed the magnesium atom in the plane of the porphyrin ring. In both cases the minimized energy was significantly higher than for the five-coordinate model.

DISCUSSION

Crystal structure

The molecular structure of (H_2O)MgT(OME)PP as determined from the X-ray diffraction analysis is shown in Figure 6.1; the fractional coordinates are given in Table 6.2 and selected bond distances and angles are given in Table 6.3. The complex has crystallographic C2 symmetry. The porphyrin core is nonplanar. The average dihedral angle between the mean planes of adjacent pyroles is 2.9°. The five-coordinate magnesium atom is displaced 0.39 Å out of the plane of the central nitrogen atoms toward the water molecule, which is typical in chlorophyll derivatives, a little longer than the 0.23 Å found in (H_2O)MgTPP. The bond distance between Mg and the water O is 2.08 Å, and the Mg-N bond distance is also 2.08 Å, similar to those found in (H_2O)MgTPP[12]. The average N-Mg-N bond angle is 88°, while the O-Mg-N bond angles range from 99.1 to 103.0°, all of which indicate an essentially square-pyramidal environment about the Mg. The two phenyl rings are not perpendicular to the porphyrin ring, the dihedral angle being approximately 69°, in contrast to (H_2O)MgTPP in which the phenyl plane is found to be perpendicular to the porphyrin plane.

The oxygen (O1) in the coordinated water is hydrogen bonded to the methoxyl oxygens (O2) in adjacent molecules (O1 being on the two-fold axis with O1 - O2 distance of 2.86 Å). The

intermolecular hydrogen bonds result in the formation of a two-dimensional polymer sheet (Figure 6.2). These hydrogen-bonded porphyrins are related by translational symmetry. Porphyrin macrocycles typically stack at separations of 3.4 Å to 3.6 Å in crystals, this distance being the optimum van der Waals contact between the π-systems of adjacent molecules. In this structure, there is no significant overlap between porphinato planes, although some π-π interaction may exist between the porphinato plane and the phenol plane (distance ~ 3.6 Å). This hydrogen bonding aggregation system is somewhat similar to that found in the X-ray structure of ethyl chlorophyllide *a* dihydrate[1] where a one-dimensional polymer results from the formation of a hydrogen bond between the coordinated water molecule and the ketone oxygen atom of an adjacent molecule, and a two-dimensional net results from the cross-linked one-dimensional polymer caused by a hydrogen bond between the interstitial water molecule and the carbonyl oxygen atom of the ethyl ester. Fischer[13] et al., Strouse[1] and recently Olson[14] have suggested that these chlorophyll-water adducts could be used as a model for aggregation of chlorophyll in vivo. Katz[15] et al. prefer to use it as a model for a dimer in the photoreaction center. Further evidence is needed to show what is most appropriate in vivo. So far, crystal structures of most of the magnesium porphyrins and chlorophyll derivatives have revealed that they contain water adducts.

Molecular modeling

Modeling of an isolated H_2OMgT(OMe)PP via molecular mechanics gave distances and angles which were in good general agreement with those obtained from the crystal structure investigation (Table 6.3). The primary difference was in the orientation of the phenyl groups; in the molecular mechanics case, the dihedral angle between the phenyl rings and the porphyrin rings were found to be ~35° as opposed to the ~69° found in the crystal structure. Such a difference is not surprising since packing effects in the crystalline state might well be expected to influence the orientation of these phenyl groups.

Molecular mechanics calculations also indicate that the hydrated form of the molecule is more stable; it is the bonding of Mg and O which plays a key role in aggregation process.

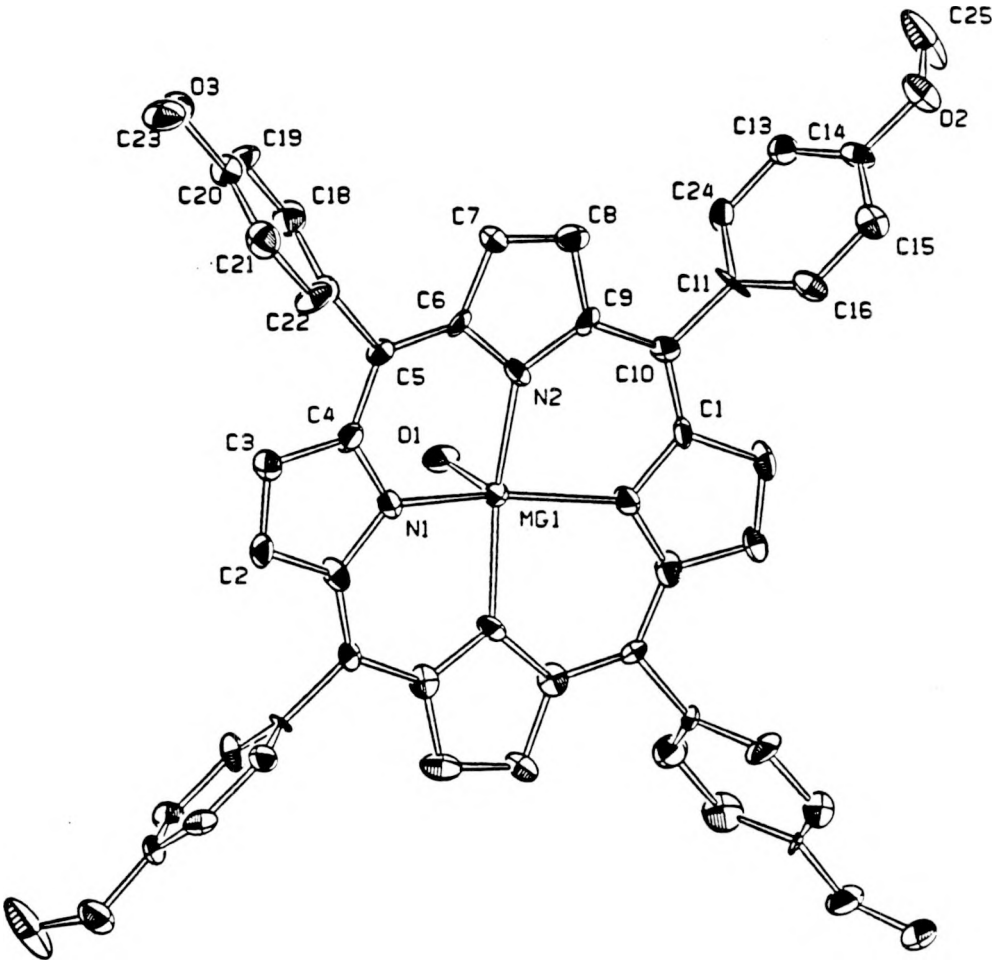

Figure 6.1 The molecular structure of $(H_2O)MgT(OME)PP$. Thermal ellipsoids are drawn at the 50% probability level.

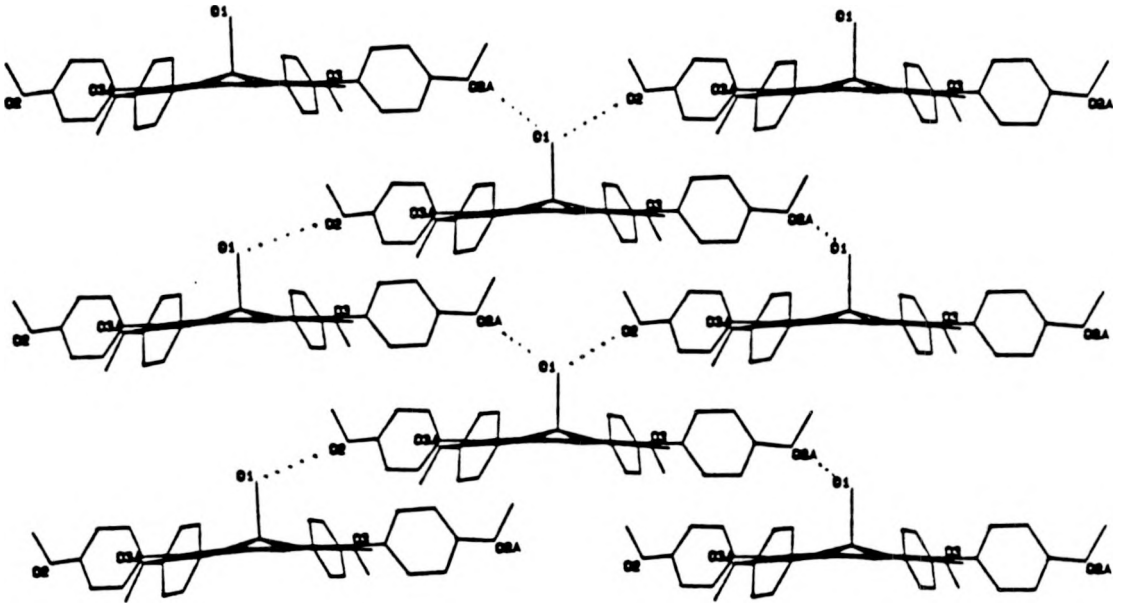

Figure 6.2 Illustration of the two-dimensional polymer sheet in the structure of (H_2O)MgT(OME)PP.

Table 6.2. Positional parameters and B(eq) for $(H_2O)MgT(OMe)PP$

atom	x	y	z	B(eq)[a]
Mg(1)	0	0.6403	0	1.3(2)[b]
O(1)	0	0.866(1)	0	2.3(5)
O(2)	-0.5214(4)	0.584(1)	-0.3690(4)	2.6(3)
O(3)	0.2447(4)	0.581(1)	-0.5073(4)	2.7(3)
N(1)	0.1215(4)	0.589(1)	-0.0233(5)	1.7(3)
N(2)	-0.0448(4)	0.604(1)	-0.1389(5)	1.4(3)
C(1)	-0.1945(6)	0.583(2)	-0.0417(7)	1.7(4)
C(2)	0.2672(6)	0.569(2)	-0.0030(7)	2.1(5)
C(3)	0.2392(6)	0.575(2)	-0.0952(7)	1.8(4)
C(4)	0.1471(6)	0.584(2)	-0.1064(6)	1.9(4)
C(5)	0.0926(5)	0.593(1)	-0.1924(5)	1.2(4)
C(6)	0.0042(6)	0.598(1)	-0.2065(6)	1.5(4)
C(7)	-0.0504(6)	0.591(2)	-0.2943(6)	1.9(4)
C(8)	-0.1316(6)	0.596(2)	-0.2778(6)	2.1(4)
C(9)	-0.1276(6)	0.599(1)	-0.1813(6)	1.4(4)
C(10)	-0.1989(5)	0.592(1)	-0.1365(6)	1.4(4)
C(11)	-0.2854(5)	0.592(2)	-0.1955(6)	1.8
C(12)	0.1332(5)	0.585(2)	-0.2749(6)	1.4(4)
C(13)	-0.3951(6)	0.720(1)	-0.3043(7)	1.9(5)
C(14)	-0.4443(6)	0.596(2)	-0.3099(6)	1.8(4)
C(15)	-0.4173(7)	0.473(1)	-0.2611(7)	1.9(5)
C(16)	-0.3380(7)	0.471(1)	-0.2033(7)	2.0(5)
C(18)	0.1288(7)	0.706(1)	-0.3341(7)	2.4(5)
C(19)	0.1661(8)	0.697(1)	-0.4100(7)	2.8(6)
C(20)	0.2094(6)	0.574(2)	-0.4298(6)	1.6(4)
C(21)	0.2139(7)	0.453(1)	-0.3727(8)	2.5(5)
C(22)	0.1746(7)	0.462(1)	-0.2959(7)	2.3(5)
C(23)	0.2842(7)	0.452(2)	-0.5327(7)	2.8(6)
C(24)	-0.3159(6)	0.715(1)	-0.2454(7)	1.8(5)
C(25)	-0.5640(7)	0.716(2)	-0.397(1)	5.3(7)
C(28)	0.529(2)	0.701(4)	0.026(2)	5(2)

[a] $$B(eq) = \frac{8\pi^2}{3} \sum_{i=1}^{3} \sum_{j=1}^{3} U_{ij} a_i^* a_j^* \vec{a}_i \cdot \vec{a}_j .$$

[b] Estimated standard deviations in the least significant figure are given in parentheses in this and succeeding tables.

Table 6.3 Selected intramolecular distances and angles for (H_2O)MgT(OMe)PP from X-ray and molecular mechanics studies

(a) Distances (Å)

atom	atom	X-ray distance	MM distance
Mg(1)	O(1)	2.078(12)	2.141
Mg(1)	N(1)	2.084(7)	2.200
Mg(1)	N(2)	2.088(7)	2.212
O(2)	C(14)	1.382(11)	1.367
O(2)	C(25)	1.419(16)	1.412
O(3)	C(20)	1.373(10)	1.367
O(3)	C(23)	1.431(14)	1.412
N(1)	C(1)	1.375(11)	1.380
N(1)	C(4)	1.371(11)	1.379
N(2)	(6)	1.383(11)	1.386
N(2)	C(9)	1.360(11)	1.386
C(1)	C(2)	1.445(12)	1.408
C(1)	C(10)	1.402(12)	1.422
C(2)	C(3)	1.365(13)	1.394
C(3)	C(4)	1.452(12)	1.408
C(4)	C(5)	1.415(11)	1.422
C(5)	C(6)	1.388(11)	1.423
C(5)	C(12)	1.490(11)	1.432
C(6)	C(7)	1.436(12)	1.406
C(7)	C(8)	1.363(13)	1.395
C(8)	C(9)	1.426(12)	1.406
C(9)	C(10)	1.420(11)	1.423
C(10)	C(11)	1.497(12)	1.431
C(11)	C(16)	1.392(16)	1.414
C(11)	C(24)	1.387(15)	1.411
C(12)	C(18)	1.409(15)	1.414
C(12)	C(22)	1.378(15)	1.411
C(13)	C(14)	1.373(15)	1.404
C(13)	C(24)	1.403(14)	1.404
C(14)	C(15)	1.375(15)	1.405
C(15)	C(16)	1.397(14)	1.404
C(18)	C(19)	1.371(14)	1.404
C(19)	C(20)	1.388(16)	1.405
C(20)	C(21)	1.394(16)	1.404
C(21)	C(22)	1.401(14)	1.405
Average absolute difference		0.028 Å	

Table 6.3 (continued)

(b) Angles (°)

atom	atom	atom	X-ray angle	MM angle
O(1)	Mg(1)	N(1)	103.0(3)	97.0
O(1)	Mg(1)	N(2)	99.1(3)	96.2
N(1)	Mg(1)	N(1)	154.1(6)	167.3
N(1)	Mg(1)	N(2)	88.1(3)	88.9
N(2)	Mg(1)	N(2)	161.8(6)	167.6
C(14)	O(2)	C(25)	116.2(10)	123.3
C(20)	O(3)	C(23)	116.7(10)	123.3
Mg(1)	N(1)	C(1)	126.1(6)	121.5
Mg(1)	N(1)	C(4)	126.6(6)	121.5
C(1)	N(1)	C(4)	106.3(7)	115.4
Mg(1)	N(2)	C(6)	126.1(6)	122.2
Mg(1)	N(2)	C(9)	126.6(6)	122.2
C(6)	N(2)	C(9)	107.0(7)	115.4
N(1)	C(1)	C(2)	109.3(8)	102.6
N(1)	C(1)	C(10)	126.0(8)	132.0
C(2)	C(1)	C(10)	124.7(8)	124.7
C(1)	C(2)	C(3)	108.3(8)	109.4
C(2)	C(3)	C(4)	105.0(8)	109.5
N(1)	C(4)	C(3)	111.1(8)	102.5
N(1)	C(4)	C(5)	125.4(8)	132.4
C(3)	C(4)	C(5)	123.5(8)	124.3
C(4)	C(5)	C(6)	125.6(7)	122.0
C(4)	C(5)	C(12)	117.0(7)	117.2
C(6)	C(5)	C(12)	117.3(7)	12(8)
N(2)	C(6)	C(5)	125.7(8)	13(10)
N(2)	C(6)	C(7)	109.5(8)	102.6
C(5)	C(6)	C(7)	124.7(8)	126.3
C(6)	C(7)	C(8)	106.0(8)	109.7
C(7)	C(8)	C(9)	108.1(8)	109.6
N(2)	C(9)	C(8)	109.3(8)	102.5
N(2)	C(9)	C(10)	125.3(8)	131.3
C(8)	C(9)	C(10)	125.3(8)	126.1
C(1)	C(10)	C(9)	125.2(8)	122.2
C(1)	C(10)	C(11)	117.7(8)	117.2
C(9)	C(10)	C(11)	117.2(8)	12(6)
C(10)	C(11)	C(16)	121.7(11)	122.0
C(10)	C(11)	C(24)	120.9(11)	125.0
C(16)	C(11)	C(24)	117.4(8)	112.9
C(5)	C(12)	C(18)	119.9(10)	121.5

Table 6.3 (b) (continued)

C(5)	C(12)	C(22)	121.7(10)	125.6
C(18)	C(12)	C(22)	118.5(8)	112.9
C(14)	C(13)	C(24)	116.9(10)	122.5
O(2)	C(14)	C(13)	122.7(10)	120.2
O(2)	C(14)	C(15)	115.2(11)	124.7
C(13)	C(14)	C(15)	122.0(9)	115.1
C(14)	C(15)	C(16)	119.9(10)	121.8
C(11)	C(16)	C(15)	120.5(10)	124.1
C(12)	C(18)	C(19)	119.5(10)	124.3
C(18)	C(19)	C(20)	121.8(10)	121.7
O(3)	C(20)	C(19)	115.7(11)	124.6
O(3)	C(20)	C(21)	124.5(10)	12(3)
C(19)	C(20)	C(21)	119.7(9)	115.0
C(20)	C(21)	C(22)	118.0(11)	122.6
C(12)	C(22)	C(21)	122.5(11)	123.5
C(11)	C(24)	C(13)	123.3(10)	123.5
Average absolute difference			4.3°	

Table 6.4 Anisotropic thermal parameters for $(H_2O)MgT(OME)PP$

ATOM	U11	U22	U33	U12	U13	U23
Mg(1)	0.015(3)	0.018(3)	0.015(3)	0	0.004(2)	0
O(1)	0.036(6)	0.036(7)	0.016(5)	0	0.006(5)	0
O(2)	0.026(4)	0.030(5)	0.036(4)	-0.001(5)	-0.009(3)	-0.006(5)
O(3)	0.039(4)	0.044(5)	0.020(4)	-0.002(5)	0.012(3)	-0.006(5)
Cl(1)	0.058(6)	0.085(7)	0.064(6)	-0.022(6)	0.018(5)	-0.031(6)
Cl(2)	0.055(8)	0.017(6)	0.24(2)	0	0.09(1)	0
Cl(*)	0.07(1)	0.29(3)	0.10(1)	-0.02(1)	0.021(8)	0.10(2)
C(28)	0.02(1)	0.09(3)	0.09(3)	0.01(1)	0.00(1)	-0.01(2)
Cl(3)	0.07(3)	0.20(3)	0.06(2)	0.05(2)	-0.00(2)	-0.04(3)
N(1)	0.012(4)	0.029(5)	0.022(4)	-0.003(5)	0.001(3)	-0.001(5)
N(2)	0.016(4)	0.018(6)	0.018(4)	-0.004(4)	-0.004(3)	-0.002(4)
C(1)	0.014(5)	0.021(6)	0.028(5)	-0.007(6)	0.002(4)	0.004(6)
C(2)	0.011(5)	0.035(8)	0.034(6)	0.001(6)	0.008(4)	0.009(6)
C(3)	0.016(5)	0.021(7)	0.029(6)	0.004(6)	0.002(4)	0.005(6)
C(4)	0.019(5)	0.029(6)	0.026(5)	0.003(6)	0.010(4)	0.010(6)
C(5)	0.021(5)	0.014(6)	0.013(5)	-0.001(6)	0.006(4)	-0.002(6)
C(6)	0.022(5)	0.018(6)	0.021(5)	-0.003(6)	0.009(4)	0.010(6)
C(7)	0.018(5)	0.032(6)	0.021(5)	-0.002(6)	-0.004(4)	0.005(6)
C(8)	0.038(6)	0.022(6)	0.017(5)	-0.006(7)	-0.002(5)	0.001(6)
C(9)	0.019(5)	0.011(6)	0.023(5)	-0.002(6)	0.005(4)	0.007(6)
C(10)	0.018(5)	0.013(6)	0.020(5)	0.007(6)	0.002(4)	0.003(6)
C(11)	0.0108					
C(12)	0.009(4)	0.028(6)	0.015(5)	0.004(6)	0.005(4)	-0.005(6)
C(13)	0.026(6)	0.022(7)	0.023(6)	-0.001(5)	0.004(5)	0.001(5)
C(14)	0.018(5)	0.028(7)	0.022(5)	0.014(6)	0.000(4)	-0.003(6)
C(15)	0.031(6)	0.018(6)	0.023(6)	-0.004(5)	0.004(5)	-0.012(5)
C(16)	0.025(6)	0.026(7)	0.022(6)	0.006(5)	-0.003(5)	-0.006(5)
C(18)	0.027(6)	0.037(8)	0.027(6)	-0.003(6)	0.008(5)	-0.005(6)
C(19)	0.044(8)	0.037(8)	0.029(7)	0.001(6)	0.012(6)	0.019(6)
C(20)	0.017(5)	0.030(7)	0.019(5)	0.011(6)	0.010(4)	-0.007(6)
C(21)	0.028(7)	0.036(8)	0.034(7)	0.003(6)	0.009(5)	-0.002(6)
C(22)	0.036(7)	0.038(8)	0.019(6)	0.001(6)	0.017(5)	-0.001(6)
C(23)	0.040(7)	0.05(1)	0.020(6)	0.008(7)	0.010(5)	-0.001(6)
C(24)	0.013(6)	0.025(7)	0.031(6)	-0.000(5)	0.003(5)	0.006(5)
C(25)	0.028(8)	0.04(1)	0.12(1)	-0.002(7)	-0.034(8)	0.00(1)

[a]The coefficients U_{ij} of the anisotropic temperature factor expression are defined as follows:

$$\exp(-2\pi^2(a^{*2}U_{11}h^2+b^{*2}U_{22}k^2+c^{*2}U_{33}l^2+2a^*b^*U_{12}hk+2a^*c^*U_{13}hl+2b^*c^*U_{23}kl))$$

Table 6.5 Least-squares planes for $(H_2O)MgT(OME)PP$

Plane number 1		
Atoms Defining Plane	Distance	esd
C(1)	-0.0868	0.0138
C(2)	-0.0710	0.0144
C(3)	-0.0676	0.0138
C(4)	-0.0187	0.0145
C(5)	0.0110	0.0126
C(6)	0.0298	0.0130
C(7)	-0.0944	0.0148
C(8)	-0.0618	0.0142
C(9)	0.0154	0.0124
C(10)	-0.0514	0.0128
N(1)	0.0649	0.0113
N(2)	0.1048	0.0101
Additional Atoms	Distance	
Mg(1)	0.5099	

Mean deviation from plane is 0.0565 angstroms

Plane number 2		
Atoms Defining Plane	Distance	esd
C(11)	0.0072	0.0094
C(15)	0.0004	0.0106
C(16)	-0.0059	0.0105
C(14)	0.0001	0.0093
C(13)	0.0035	0.0103
C(24)	-0.0084	0.0101

Mean deviation from plane is 0.0042 angstroms

Dihedral angles between least-squares planes

plane	plane	angle
2	1	110.04

Plane number 3		
Atoms Defining Plane	Distance	esd
C(12)	0.0059	0.0092
C(18)	-0.0012	0.0109
C(19)	-0.0093	0.0121
C(20)	0.0058	0.0100
C(21)	-0.0003	0.0114
C(22)	-0.0090	0.0110

Mean deviation from plane is 0.0052 angstroms

Dihedral angles between least-squares planes

plane	plane	angle
3	1	67.43
3	2	94.93

Table 6.5 (continued)

Plane number 4

Atoms Defining Plane	Distance	esd
C(1)	-0.0495	0.0138
C(2)	-0.0773	0.0144
C(3)	-0.0281	0.0138
C(4)	0.0311	0.0144
N(1)	0.0763	0.0113

Mean deviation from plane is 0.0525 angstroms

Dihedral angles between least-squares planes

plane	plane	angle
4	1	1.92
4	2	108.64
4	3	68.68

Plane number 5

Atoms Defining Plane	Distance	esd
C(6)	0.0016	0.0130
C(7)	0.0117	0.0148
C(8)	-0.0200	0.0142
C(9)	0.0158	0.0124
N(2)	-0.0058	0.0101

Mean deviation from plane is 0.0110 angstroms

Dihedral angles between least-squares planes

plane	plane	angle
5	1	175.24
5	2	73.23
5	3	109.21
5	4	177.15

ACKNOWLEDGEMENT

We would like to acknowledge our indebtedness for assistance in the synthesis of the $(H_2O)MgT(OME)PP$ to Donald J. Czapla. We thank Dr. Mannar R. Maurya and W. S. Struve for valuable discussion. The Ames Laboratory is operated for the U.S. Department of Energy by Iowa State University under contract No. W-7405-Eng-82.

REFERENCES

1. Chow, H.; Serlin, R.; Strouse, C. E. JACS, 1975, 97, 7230

2. Bystrova, M. I.; Malgosheva, I. N.; Krasnovskii, A. A. Mol. Biol. 1979, 13, 582.

3. Smith, K. M.; Kehrers, L. A.; Fajer, J. JACS, 1983a, 105, 1387.

4. Brune, D. C.; Nozawa, T.; Blankenship, R. E. Biochemistry 1987, 26, 8644.

5. Adler, A. D.; Longo, F. R.; Kampas, F.; Kim, J. J. Inorg. Nucl. Chem. 1970, 32, 2443.

6. Gilmore, C. J. MITHRIL - an integrated direct methods computer program, J. Appl. Cryst. 17(42-46), University of Glasgow, Scotland, 1984. P. T. Beurskens, DIRDIF: Direct Methods for Difference Structure-- an automatic procedure for phase extension and refinement of difference structure factors. Technical Report 1984/1 Crystallography Laboratory, Toernooiveld, 6525 Ed Nijmegen, Netherlands.

7. Cromer, D. T.; Waber, J. T. International Tables for X-ray Crystallography Vol. IV, The Kynoch Press, Birmingham, England, 1974, Table 2.2 A.

8. Ibers, J. A.; Hamilton, W. C. Acta Crystallogr. 1964, 17, 781.

9. Cromer, D. T. International Tables for X-ray Crystallography Vol. IV, The Kynoch Press, Birmingham, England, 1974, Table 2.3.1

10. Gilbert, K. E.; Gajewski, J. J. PCMODEL--Molecular Modeling Software. Version 3.0. Serenna Software, Box 3076, Bloomington, IN 47402-3076.

11. Burkert U.; Allinger, N. L. ACS Monograph Services, No. 175.

12. Timkovich R.; Tulinsky, A. J. Am. Chem. Soc. 1969, 91(16), 4430.

13. Fischer, M. S.; Templeton, D. H.; Zalkin, A.; Calvin, M. JACS, 1972, 94, 3613.

14. Olson, J. M.; Van Brakel, G. H.; Gerola, P. D.; Pedersen, J. P. Progress in Photosynthesis Research. Biggens, J. (ed.), Vol. 1, ISBN 90-247-34509.

15. Shipman, L. L.; Cotton, T. M.; Norris, J. R.; Katz, J. J. Proc. Natl. Acad. Sci. 73, 1976, 1791

SECTION VII. SYNTHESIS AND CHARACTERIZATION OF A NEW BIS-ALANYL-APPENDED PORPHYRIN AND ITS MONONUCLEAR CU(II),NI(II)AND ZN(II) COMPLEXES. CRYSTAL STRUCTURE OF THE NI(II) COMPLEX.

SYNTHESIS AND CHARACTERIZATION OF A NEW BIS-ALANYL-APPENDED PORPHYRIN AND ITS MONONUCLEAR CU(II), NI(II) AND ZN(II) COMPLEXES. CRYSTAL STRUCTURE OF THE NI(II) COMPLEX.

Shumei Yang, Robert A. Jacobson

and

L. Keith Woo, Mannar R. Maurya, Connie J. Tolppi

Department of Chemistry and Ames Laboratory-USDOE

Iowa State University, Ames, Iowa 50011

INTRODUCTION

The importance of porphyrins and porphyrin derivatives is evident from the prominence of metalloporphyrins in many biological functions [1]. The use of synthetic metalloporphyrins to model the activities of natural systems has stimulated the preparation of a variety of functionalized porphyrins with specially designed cavities for selective substrate binding and/or ligating appendages for binding additional metals. A partial list of these porphyrins includes elegant molecules such as picket-fence porphyrins [2], pincer-porphyrins [3], basket-handle porphyrins [4], gyroscope porphyrins [5], triple-decker porphyrins [6], and bis-pocket porphyrins [7]. In addition, a number of binucleating porphyrins have been prepared for use in modelling the active sites of multi-metal proteins [8-10]. The accessibility of multi-chelating porphyrin ligands should allow for the preparation of oligomeric metal complexes and capitalization of the chemistry that is unique to multi-metal systems. Of interest is the possibility of designing and preparing linear arrays of transition metals as a means of producing new materials with desired optical, magnetic, or conductivity properties. However, the majority of the multi-chelating porphyrins such as those reported by Reed [3], Elliot

[11], Gunter [9], and Chang [10] have sufficiently bulky appendages or have structures that limit these ligands to binding two metals. We have designed a more flexible ligand system in order to promote the formation of oligomeric complexes.

In this paper, we report the simple synthesis of a new multi-chelating ligand, cis-5,15-bis (o-[ß-alanylamido]phenyl)-2,8,12,18-tetraethyl-3,7,13,17-tetramethylporphyrin, cis-$(ala)_2$-DPE. This ligand consists of two chemically distinct metal binding sites @ the porphyrin unit and the terminal amines of the alanyl groups. As a means of preparing molecular building blocks for multi-nuclear metal arrays, we have metallated the porphyrin core of this ligand to form mononuclear complexes with Ni(II), Cu(II), and Zn(II). A single crystal X-ray structure determination has been carried out for the nickel complex.

EXPERIMENTAL

Preparations

All reagents were of analytical grade. THF was freshly distilled from purple solutions containing sodium and benzophenone. 5,15-bis(o-aminophenyl)-2,8,12,18-tetraethyl-3,7,13,17-tetramethylporphyrin, (NH2)2DPE, was synthesized according to the method reported elsewhere [12].

cis-Bis-(o-aminophenyl)-2,8,12,18-tetraethyl-3,7,13,17-tetramethylporphyrin, 1

The cis and trans mixture of bis-(o-aminophenyl)-2,8,12,18-tetraethyl-3,7,13,17-tetramethylporphyrin, $(NH_2)_2$DPE, prepared by the Chang procedure [12], was converted to the cis isomer by following Lindsey's procedure with some modifications [13]. A mechanically stirred mixture of toluene (1.5 L, dried over molecular sieves) and 300 g silica gel was heated at reflux for two hours under nitrogen. A cis/trans mixture of $(NH_2)_2$DPE (8.5 g) was added and heating at reflux was continued for 4 - 7 days. After cooling to room temperature, the slurry was poured in to a 15 cm diameter coarse glass frit and rinsed with toluene until the washings were clear, to remove the trans isomer. cis-$(NH_2)_2$DPE was eluted from the silica gel with benzene/ether (1:1)

and isolated by removing the solvent under reduced pressure to yield 5.1 g (60%) of purple solid. Purity of the cis and trans isomers were checked by analytical TLC (SiO_2, CH_2Cl_2-CH_3OH; 98:2) and ^1H NMR spectroscopy. The ^1H NMR spectra agree well with literature values [12].

N-t-butoxycarbonyl-ß-alanine (BOC-ß-alanine)

This compound was prepared following a modified literature method [15]. BOC-ON (2-(t-butoxycarbonyloxyimino)-2-phenylacetonitrile) (30.0g, 0.12 mol) dissolved in 66 ml 1,4-dioxane was added to a stirred solution of ß-alanine (9.87g, 0.11 mol) and triethylamine (24 ml) followed by a subsequent addition of 66 ml H_2O. After stirring the reaction mixture for 2.5 hrs, 80 ml saturated NaCl and 20 ml ethyl acetate were added. The aqueous layer was separated and washed several times with ethyl acetate. When the water solution became clear, it was acidified with 1N HCl to pH 1 and was extracted with CH_2Cl_2 (4 x 100 ml). The CH_2Cl_2 fractions were combined and evaporated to yield a viscous oil. After addition of 20 ml hexane, the flask was cooled to -30°C. The precipitate was filtered and dried under vacuum at ambient temperature to yield 20.4 g (88%) of white solid. ^1H NMR ($CDCl_3$): 6.30(s, 1H, OH), 5.08(s, 1H, NH), 3.36(t, 2H, CH_2), 2.54(t, 2H, CH_2) and 1.41(s, 9H, t-butyl).

cis-Bis-(o-[N-t-butoxycarbonyl-ß-alanylamido]phenyl)-2,8,12,18-tetraethyl-3,7,13,17-tetramethylporphyrin, 2

The method used to attach amino acid side chains to cis-$(NH_2)_2$DPE is based on the strategy described by Rose [16]. Under nitrogen, N-methyl piperidine (1.98g, 20 mmol) and isobutylchloroformate (2.10g, 15.4 mmol) were added to a cold (-30°C) solution of N-t-butoxycarbonyl-ß-alanine (3.78g, 20 mmol) dissolved in 300 ml THF. cis-$(NH_2)_2$DPE (1.32g, 4 mmol) in 200 ml THF (cooled to -30°C) was added to this solution through a cannula. The reaction mixture was stirred at -30°C for an hour and the temperature was slowly increased to ambient temperature over 10 hrs. The solution was filtered and the residues were washed with THF. The combined filtrates were evaporated to dryness, redissolved in 200 ml CH_2Cl_2 and washed successively with H_2O, 1% $NaHCO_3$, H_2O, 0.1 N HCl and H_2O. After drying the organic layer over $MgSO_4$ and filtering, the solvent was removed under reduced pressure. The crude product was purified on a silica gel column (30 x 4 cm) eluting with CH_2Cl_2/ether (95:5 to 90:10). Removal of the solvent under reduced pressure yielded 1.8 g of purple solid (90%). Trace amounts of free BOC-ß-alanine were always present in the final product, but were readily removed in the subsequent deprotection step. UV/VIS ($CHCl_3$):

408 (soret), 508, 542, 574, 626 nm. FAB MS (MH^+): Found, 1003.4; Calc., 1003.0. IR (nujol mull): ν_{CO} = 1680 and 1710 cm^{-1}. ^1H NMR ($CDCl_3$): -2.49(s, 2H, $NH_{pyrrole}$), 1.19(s, 18H, t-butyl), 1.45(s, free BOC-ß-alanine), 1.49 (t, $-C\underline{H}_2CH_2$), 1.77(t, 12H, $CH_2C\underline{H}_3$), 2.52(s, 12H, CH_3), 2.85(t, 4H, $-CH_2C\underline{H}_2-$), 4.04(q, 8H, $C\underline{H}_2CH_3$), 4.87 (s, 2H, N<u>H</u>BOC), 6.84(s, 2H, NH aryl), 7.53(t, 2H, aryl), 7.85(m, 4H, aryl), 8.75(d, 2H, aryl), 10.27(s, 2H, meso H).

<u>cis-5,15-bis(o-[ß-alanylamido]phenyl)-2,8,12,18-tetraethyl-3,7,13,17-tetramethylporphyrin, 3</u>

The BOC-protected porphyrin, **2**, (0.5g, 0.50 mmol) was dissolved in 40 ml 1:1 CH_2Cl_2/trifluoroacetic acid (TFA) and the resulting green solution was stirred at ambient temperature for one hr. After removing the solvent under reduced pressure, the resulting solid was washed with diethyl ether until no green color in the washing was evident. The residues were dissolved in a minimum of acetone and poured in to 400 ml of 1:1 CH_2Cl_2/water. The solution was neutralized to pH 7 with 1% $NaHCO_3$ and extracted with CH_2Cl_2. After removing the solvent under reduced pressure, the crude product was purified by chromatography on a 35 x 4 cm silica gel column eluting successively with 95:5, 90:10 to 80:20 CH_2Cl_2/MeOH solvent mixtures. The second band, a dark, slow

moving component, (90:10 to 80:20 fractions) was collected and evaporated to dryness to yield 0.2 g of purple solid (50%). UV/VIS ($CHCl_3$): 408 (soret), 510, 544, 575, 625 nm. FAB MS (MH^+): Found, 803.2; Calc., 803.0. IR(nujol mull): ν_{CO} = 1680 cm^{-1}. ^1H NMR ($CDCl_3$): -2.48(s, 2H, $NH_{pyrrole}$), -1.35(s, 4H, NH_2), 9.48(s, 2H, NH aryl), 1.63(t, 8H, $-C\underline{H}_2C\underline{H}_2-$), 1.78(t, 12H, $-CH_2C\underline{H}_3$), 2.55(s, 12H, CH_3), 4.02(q, 8H, $C\underline{H}_2CH_3$), 7.49(t, 2H, aryl), 7.73(m, 4H, aryl), 8.76(d, 2H, aryl), and 10.22(s, 2H, meso-H).

Nickel and Copper Porphyrin Complexes

To a stirred solution of cis-(ala)2DPE (0.20g, 0.25 mmol) in 10 ml CHCl3/MeOH (9:1) was added a solution of the respective metal acetate (0.25 mmol) in 5 ml MeOH with stirring. The resulting reaction mixture was heated at reflux for 4 hrs. After evaporating the solvent to dryness, 200 ml water and 20 ml 1 N HCl were added to the flask and the suspension was stirred for 4 hrs, before extracting the suspension with CH2Cl2. The CH2Cl2 solution was dried over MgSO4, filtered, and concentrated to 2 ml. The solution was layered with 8 ml of n-hexane and cooled to 12°C for 4 hrs. The precipitated solid was filtered, washed with n-hexane and dried in vacuo at ambient temperature.

[cis-(Ala)2DPE]Ni(II)

Yield: 0.18 g, 84.1% of red solid. UV/VIS ($CHCl_3$): 408 (soret), 530, 566 nm. FAB MS (MH^+): Found, 859.2; Calc., 858.9. ^1H NMR ($CDCl_3$): 5.69(s, 2H, NH), 7.01(s, 4H, NH_2), 1.28(t, 4H, $-CH_2CH_2-$), 2.77(t, 4H, $-CH_2CH_2-$), 1.59(t, 12H, $CH_2C\underline{H}_3$), 2.19(s, 12H, CH_3), 3.67(q, 8H, $C\underline{H}_2CH_3$), 7.56(t, 2H, aryl), 7.69(t, 2H, aryl), 8.33(d, 4H, aryl) and 9.39(s, 2H, meso-H). [cis-$(Ala)_2$DPE]Cu(II). Yield: 0.16 g, 74.4% of brown solid. UV/VIS ($CHCl_3$): 410 (soret), 534, 570 nm. FAB MS (MH^+): Found, 864.3; Calc., 864.5.

[cis-(Ala)2DPE]Zn(II)

Zinc acetate (0.056g, 0.25 mmol) in 5 ml methanol was added to a stirred solution of cis-$(ala)_2$DPE (0.20g, 0.25 mmol) in 10 ml $CHCl_3$/MeOH (9:1) and the mixture was heated at reflux for 4 hrs. After evaporating the solvent to dryness, 4 ml toluene and 6 ml n-hexane were added to the flask and the mixture was cooled to 12°C for 4 hrs. The resulting light red solid was filtered, washed with n-hexane and dried in vacuo at ambient temperature to yield 0.14 g of product (67%). UV/VIS ($CHCl_3$): 420(soret), 546, 582 nm. FAB MS (MH^+): Found, 866.4; Calc., 866.4. ^1H NMR ($CDCl_3$): 7.09(s, 2H, NH), 2.95(s, 4H, NH_2), 1.03(t, 4H, $-CH_2CH_2-$), 1.42(t, 4H, $-CH_2C\underline{H}_2-$), 1.73(t, 12H, $CH_2C\underline{H}_3$), 2.46(s, 12H,

CH_3), 3.97(q, 8H, $C\underline{H}_2CH_3$), 7.69 (t, 2H, aryl), 7.84(t, 2H, aryl), 8.08(d, 4H, aryl) and 10.10(s, 2H, meso H).

Measurements

Visible spectra were recorded at room temperature on a HP 8452A diode array spectrophotometer using chloroform as solvent. IR spectra were run as nujol mulls on a IBM IR-98 Fourier Transform infrared spectrophotometer. ^1H NMR spectra were recorded on a Nicolet NIC 300 spectrometer using $CDCl_3$ as solvent. Chemical shifts δ (in ppm) are reported relative to $CDCl_3$ (7.24 ppm). FAB mass spectra were obtained on a Kratos MS-50 spectrometer. Magnetic susceptibility measurements were carried out on a Quantum Design superconducting quantum interference device. Diamagnetic corrections for the ligand and the copper complex were computed using Pascal's constants [17]. The susceptibility was corrected for the temperature independent paramagnetism term using 60×10^{-6} c.g.s. for the copper complex.

X-ray Crystal Structure Determination

A single crystal of [cis-(ala)2DPE]Ni(II)$\cdot CHCl_3 \cdot CH_3OH$ suitable for X-ray structure determination was grown by slow evaporation of $CHCl_3$/hexane/CH_3OH (3:2:1) solution of [cis-(ala)2DPE]Ni(II) at -15°C. A purple hexagonal crystal having

approximate dimensions of 0.18 x 0.20 x 0.30 mm was mounted on a glass fiber. A Rigaku AFC6R diffractometer with graphite monochromated Mo Kα radiation (= 0.71069 Å) and a 12 KW rotating anode generator was used to collect the data. Intensities exhibited a pronounced tendency to decrease rapidly with scattering angle, and even with a high intensity source, it was difficult to obtain a large number of observed ($I > 3.0\ \sigma\ (I)$) reflections. Based on systematic absences of: h0l: $h+1 \neq 2n$, 0k0: $k \neq 2n$ and the successful solution and refinement of the structure, the space group was determined to be $P2_1/n$ (# 14). The intensity data were collected at $-80 \pm 1°C$ using the ω scan technique to maximum 2θ value of 55.1°. Pertinent crystallographic parameters are presented in Table 7.1. Three standard reflections were monitored every 150 reflections measured, and their intensities showed good stability of the complex throughout the data collection. Reflection data were corrected for Lorentz-polarization and absorption. The structure was solved by direct methods [18]. All non-hydrogen atoms were refined anisotropically. All hydrogen atoms were included as fixed contributions at riding, idealized locations. Full-matrix least-squares refinement of positional and thermal parameters led to convergence with a final unweighted R factor of 0.085 and a weighted R factor of 0.089 for 604 variable refined against 3460

observed reflections. The maximum peak in the final electron density map was 0.71 $e^-/Å^3$. Neutral atom scattering factors were taken from Cromer and Waber [19]. Anomalous dispersion effects were included in F_{calc} [20]; the values for $\Delta F'$ and $\Delta F''$ were those of Cromer [21]. All calculations were performed using the TEXSAN cryatallographic software package of Molecular Structure Corporation [22].

Table 7.1 Crystallographic Parameters for $NiCl_3O_3N_8C_{52}H_{61}$

Empirical Formula	$NiCl_3O_3N_8C_{52}H_{61}$
Formula Weight (g mol^{-1})	1010.19
Crystal Color, Habit	purple, hexagonal
Crystal Dimensions (mm)	0.18 x 0.20 x 0.30
Crystal System	monoclinic
No. Reflections Used for Unit Cell Determination (2θ range)	15 (12.9 - 15.1°)
Omega Scan Peak Width at Half-height	0.48
Lattice Parameters:	a (Å) = 14.195 (5) b (Å) = 12.175 (6) c (Å) = 28.07 (1) ß (°) = 98.97 (3) V ($Å^3$)= 4792 (3)
Space Group	$P2_1/n$ (#14)
Z value	4
D_{calc} (g/cm^3)	1.367
F_{000}	2040
$\mu_{(MoK\alpha)}$ (cm^{-1})	10.65
Diffractometer	Rigaku AFC6R
Radiation	MoKα (λ = 0.71069 Å)
Temperature (°C)	-80
Scan Type	ω
Scan Rate (°/min)	16.0 (in omega) (2 rescans)
Scan Width (°)	(1.29 + 0.30 tanθ)
$2\theta_{max}$	55.1°
No. of Reflections Measured	Total: 12057 Unique: 11599(R_{int} = .087)
Corrections	Lorentz-polarization Absorption
Structure Solution	Direct Methods
Refinement	Full-matrix least-squares
Function Minimized	$\Sigma w (\|Fo\| - \|Fc\|)^2$
Least-squares Weights	$4Fo^2/\sigma^2(Fo^2)$
p-factor	0.03
Anomalous Dispersion	All non-hydrogen atoms
No. Observations (I > 3.00σ(I))	3460
Residuals: R; R_w	0.085; 0.089
Max. Peak left in Diff. Map($e/Å^3$)	0.71

RESULTS AND DISCUSSION

Synthesis

Ligand

The synthetic strategy for the preparation of the bis-alanyl appended porphyrin ligand is depicted in Scheme 1. The key ligand precursor, bis-(o-aminophenyl)-2,8,12,18-tetraethyl-3,7,13,17-tetramethylporphyrin, $(NH_2)_2$DPE, was obtained as a mixture of cis and trans isomers via the procedure given by Young and Chang [12]. Thermal atropisomerization of this mixture in a manner similar to that reported by Lindsey [13] and Elliott [14] allowed isolation of the pure cis isomer, **1**, in 60-80% yields. Attachment of ligating appendages to the o-amino substituents was accomplished with mixed anhydrides of N-t-butoxycarbonyl (BOC) protected amino acids. Thus, cis-5,15-bis-(o-[N-t-butoxycarbonyl-ß-alanylamido]phenyl)-2,8,12,18-tetraethyl-3,7,13,17-tetramethylporphyrin, **2**, was prepared by treating cis-$(NH_2)_2$DPE with the mixed anhydride derived from N-BOC-ß-alanine and isobutylchloroformate. Removal of the BOC protecting groups with CH_2Cl_2/TFA led to the formation of the desired binucleating ligand cis-5,15-bis(o-[ß-alanyl-amido]phenyl)-2,8,12,18-tetraethyl-3,7,13,17-tetramethylporphyrin, cis-$(ala)_2$DPE, **3**. The solid state IR spectrum of **3** exhibits an amide carbonyl stretch

at 1680 cm^{-1}. The ^1H NMR spectrum of **3** readily demonstrates the presence of the ß-alanyl groups attached to the o-aminophenyl substituents. Both sets of methylene protons of the alanyl fragment coincidentally resonate at 1.63 ppm. The amide proton signal is at 9.48 ppm and the terminal amine protons appear at -1.35 ppm. The high-field shift of the terminal amine proton signal indicates that the appended alanyl groups spend a significant time in the shielding porphyrin ring current. The assignments of the amide-NH and terminal-NH_2 resonances have been confirmed by observing the disappearance of these signals in a D_2O-exchanged sample. A particularly useful area in the NMR spectra of these types of compounds is the meso-proton region, which is typically well-separated from other signals. The chemical shift of the meso proton can be diagnostic of the type of complex, while the number of signals in this region gives an indication of the purity of the sample. In the free-base ligand, the meso-proton appears at 10.22 ppm. The UV/VIS spectrum of cis-$(ala)_2$DPE exhibits a Soret band at 408 nm and four visible bands at 510, 544, 575, and 625 nm.

Scheme 1

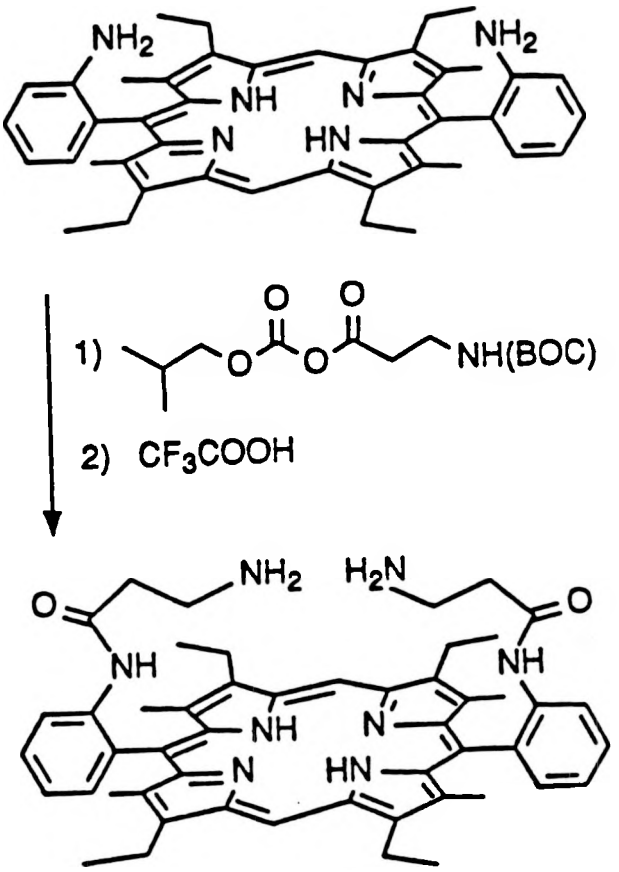

Metal complexes

Treatment of cis-$(ala)_2$DPE, **3**, in $CHCl_3$ with freshly prepared methanolic solutions of Ni(II), Cu(II) or Zn(II) ions afforded metallated complexes. After four hours of heating at reflux, UV/VIS spectra of the reaction mixtures showed that the four Q bands of the free ligand collapsed to a two-band pattern. This clearly indicated that a metal has inserted into the porphyrin core of the ligand. In the case of [cis-$(ala)_2$DPE]Cu(II) and [cis-$(ala)_2$DPE]Ni(II), it was necessary to hydrolyze the crude product with aqueous HCl to remove any possibility of formation of species of higher nuclearity [23]. In contrast, [cis-$(ala)_2$DPE]Zn(II) did not require an acid work-up as mononuclear complexes were always isolated under the reaction conditions employed. FAB mass spectra of the complexes exhibit the expected molecular ion peaks for mononuclear metal complexes. Further evidence for the insertion of Zn and Ni into the porphyrin core is derived from ^1H NMR. In both of these cases, the internal pyrrole NH proton resonances are no longer present in the NMR spectra of the isolated complexes and indicate that the pyrrole nitrogens are coordinated to metal ions. The purity of the diamagnetic metal complexes is readily ascertained by the presence of a single meso-proton resonance in the NMR spectrum. In [cis-$(ala)_2$DPE]Ni(II), this signal appears at 9.39 ppm. For

the corresponding Zn complex, it occurs at 10.10 ppm. The copper(II) complex is paramagnetic with a magnetic moment of 2.22 BM at ambient temperature as expected for magnetically dilute copper complexes.

X-ray Structure of the Ni(II) Complex

The molecular structure of [cis-$(ala)_2$DPE]Ni(II) is shown in Fig. 7.1 along with the atom numbering scheme. Table 7.2 presents a listing of fractional coordinates for non-hydrogen atoms and Table 7.3 gives selected bond distances and angles. The large thermal parameters associated with some of the atoms on the periphery of the molecule would explain the rapid fall-off in observed intensities. The average dihedral angle between the mean planes of adjacent pyrrole rings is 25.4° and indicates that the porphyrin core of this complex is ruffled in a manner similar to the S_4-ruffling of the tetragonal form of octaethylporphyrinato nickel(II), Ni(OEP) [22]. The average Ni-$N_{pyrrole}$ distance of 1.92 Å is at the lower limit for Ni-N distances in other Ni porphyrin structures [25-30]. The N-Ni-N bond angles range from 88.1(4)° to 92.3(4)° and indicate that the Ni environment is square planar. An unusual difference in the ruffled porphyrin core of [cis-$(ala)_2$DPE]Ni(II) relative to that of the tetragonal form of Ni(OEP) involves the displacement of

the meso carbons from the mean porphyrin plane. In Ni(OEP) these atoms are displaced alternately above and below the mean porphyrin plane by 0.51 Å. Although the meso carbons in [cis-$(ala)_2$DPE]Ni(II) are also positioned alternately above and below the mean porphyrin plane, one of the atoms, C_{20}, bearing a phenyl group, is only displaced 0.19 Å from the plane while the other three atoms show a more typical displacement averaging 0.55 Å. The smaller displacement of C_{20} does not appear to be due to any unusual nonbonding interactions involving the appended alanyl arm. There is clearly no intramolecular interappendage H-bonding as the two terminal nitrogen atoms, N_7 and N_8, are separated by 7.61 Å. This is in marked contrast to the structures of monometallic pincer-porphyrins in which the orientation of the benzimidazole arms is influenced by intramolecular H-bonding with an adjacent pivalamido group [3]. However, H-bonding does occur between the terminal amine (N_7) and the amido group (N_5) of the same appendage. The N_7-N_5 distance is 2.80 Å. The distance between the terminal amine, N_8, and the amide, N_6, of the other arm is 4.38 Å. A key feature to note is that the insertion of Ni into the porphyrin core has not caused atropisomerization of the alanyl appendages. Thus the chelating ability of the terminal amines is retained and further metallation is possible.

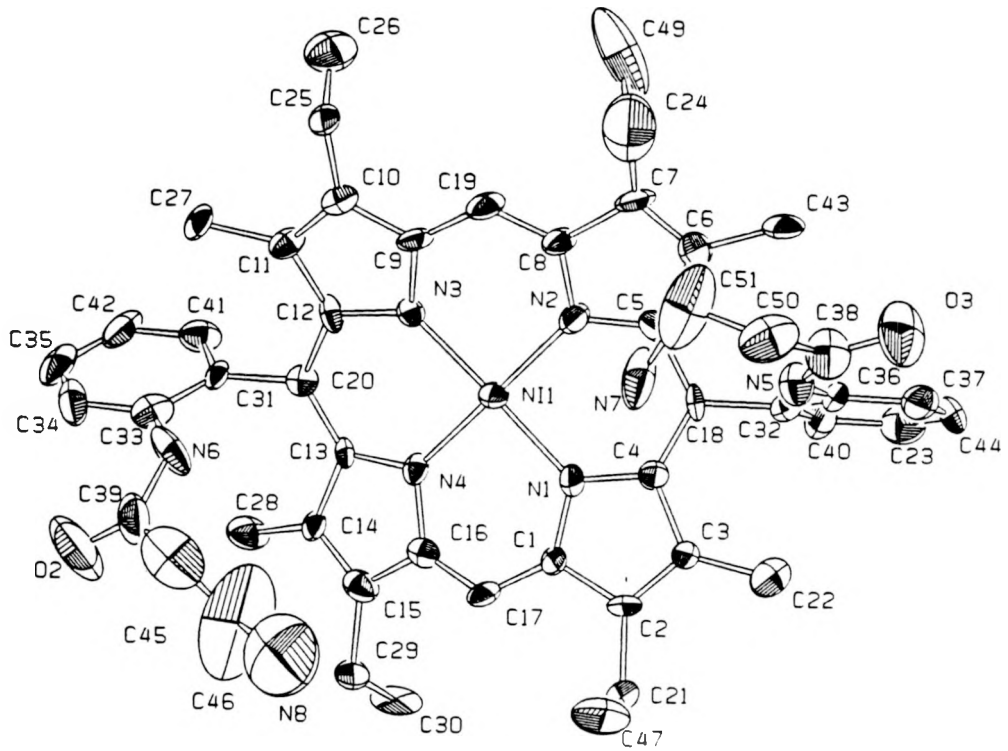

Figure 7.1 Molecular structure and atom numbering scheme for [cis-$(ala)_2$DPE]Ni(II). Note that the atom numbering scheme is unrelated to the numbering rules used for systematic nomenclature of the ligand. Hydrogen atoms and solvate molecules have been omitted for clarity.

Table 7.2 Positional parameters and B(eq) for $NiCl_3O_3N_8C_{52}H_{61}$

atom	x	y	z	B(eq)[a]
Ni(1)	0.2040(1)[b]	0.2075(1)	0.52757(6)	2.12(7)
Cl(1)	0.0229(3)	0.2223(5)	0.8162(2)	7.7(3)
Cl(2)	0.0759(4)	0.0988(5)	0.7384(2)	10.9(4)
Cl(3)	-0.1046(4)	0.0689(6)	0.7642(2)	10.4(4)
O(1)	-0.091(2)	0.497(3)	0.643(1)	34(3)
O(2)	-0.2735(9)	0.389(1)	0.4198(5)	11(1)
O(3)	0.7130(8)	0.378(1)	0.6621(4)	6.9(7)
C(52)	-0.096(1)	0.391(2)	0.6863(8)	10(1)
N(1)	0.2293(7)	0.2352(9)	0.5960(3)	2.4(5)
N(2)	0.3386(7)	0.197(1)	0.5278(3)	2.9(5)
N(3)	0.1772(6)	0.199(1)	0.4584(3)	2.1(5)
N(4)	0.0693(6)	0.2029(9)	0.5281(3)	1.9(4)
N(5)	0.5567(8)	0.330(1)	0.6428(4)	3.4(6)
N(6)	-0.1254(8)	0.331(1)	0.4172(5)	4.3(7)
N(7)	0.438(1)	0.451(1)	0.5725(4)	5.5(7)
N(8)	-0.098(2)	0.545(2)	0.5439(8)	14(2)
C(1)	0.1647(9)	0.277(1)	0.6221(4)	2.7(6)
C(2)	0.2125(8)	0.306(1)	0.6698(4)	2.6(6)
C(3)	0.3016(8)	0.274(1)	0.6735(4)	2.3(6)
C(4)	0.3145(8)	0.231(1)	0.6271(4)	2.1(6)
C(5)	0.410(1)	0.176(1)	0.5656(5)	3.1(7)
C(6)	0.499(1)	0.154(1)	0.5483(5)	4.0(8)
C(7)	0.482(1)	0.178(2)	0.5014(5)	6(1)
C(8)	0.3830(8)	0.206(2)	0.4876(4)	4.2(7)
C(9)	0.2421(9)	0.220(1)	0.4277(4)	2.4(6)
C(10)	0.197(1)	0.226(1)	0.3794(4)	2.5(6)
C(11)	0.1048(9)	0.204(1)	0.3776(4)	2.4(6)
C(12)	0.0916(8)	0.185(1)	0.4271(4)	2.1(6)
C(13)	-0.0030(8)	0.163(1)	0.4934(4)	1.7(5)

[a]the equivalent isotropic temperature factor is defined as follows:

$$B_{eq} = \frac{8\pi^2}{3} \sum_{i=1}^{3} \sum_{j=1}^{3} u_{ij} a^*_i a^*_j \vec{a}_i \cdot \vec{a}_j$$

[b]estimated standard deviations in the least significant figure are given in parentheses.

Table 7.2 (continued)

C(14)	-0.0914(8)	0.150(1)	0.5129(4)	2.1(6)
C(15)	-0.0755(9)	0.192(1)	0.5569(5)	2.8(6)
C(16)	0.0225(8)	0.225(1)	0.5671(4)	2.1(6)
C(17)	0.0678(9)	0.272(1)	0.6082(4)	2.6(6)
C(18)	0.3980(8)	0.189(1)	0.6136(4)	2.1(6)
C(19)	0.3391(9)	0.222(1)	0.4414(4)	3.6(7)
C(20)	0.0064(9)	0.160(1)	0.4448(4)	1.9(6)
C(21)	0.164(1)	0.367(1)	0.7056(4)	3.8(8)
C(22)	0.376(1)	0.290(1)	0.7173(5)	4.2(7)
C(23)	0.542(1)	0.027(1)	0.7123(5)	4.0(8)
C(24)	0.572(2)	0.227(2)	0.4608(9)	12(2)
C(25)	0.2474(9)	0.247(1)	0.3372(4)	3.2(7)
C(26)	0.272(1)	0.144(1)	0.3134(5)	5.0(9)
C(27)	0.0311(9)	0.203(1)	0.3327(4)	4.0(7)
C(28)	-0.1807(9)	0.093(1)	0.4911(5)	3.5(7)
C(29)	-0.1450(8)	0.204(1)	0.5910(4)	2.8(6)
C(30)	-0.149(1)	0.105(2)	0.6230(5)	6(1)
C(31)	-0.0819(8)	0.139(1)	0.4085(4)	2.3(6)
C(32)	0.4779(9)	0.159(1)	0.6534(4)	2.5(6)
C(33)	-0.146(1)	0.227(1)	0.3954(5)	2.9(7)
C(34)	-0.223(1)	0.212(2)	0.3602(5)	4.2(8)
C(35)	-0.243(1)	0.110(2)	0.3411(5)	4.4(9)
C(36)	0.5558(9)	0.229(1)	0.6670(4)	2.8(7)
C(37)	0.627(1)	0.198(1)	0.7043(5)	3.6(7)
C(38)	0.631(1)	0.397(1)	0.6406(6)	4.7(9)
C(39)	-0.190(1)	0.405(2)	0.4295(6)	5(1)
C(40)	0.474(1)	0.063(1)	0.6758(5)	3.4(7)
C(41)	-0.101(1)	0.039(1)	0.3882(5)	3.0(7)
C(42)	-0.180(1)	0.020(1)	0.3542(5)	3.9(8)
C(43)	0.592(1)	0.112(1)	0.5753(5)	4.7(8)
C(44)	0.620(1)	0.097(1)	0.7259(5)	3.8(8)
C(45)	-0.149(1)	0.503(2)	0.4593(9)	7(1)
C(46)	-0.143(2)	0.465(2)	0.514(1)	16(2)
C(47)	0.165(1)	0.491(2)	0.7018(6)	6(1)
C(48)	-0.009(2)	0.148(3)	0.767(1)	27(3)
C(49)	0.560(1)	0.127(2)	0.451(1)	11(2)
C(50)	0.611(1)	0.492(2)	0.6071(6)	6(1)
C(51)	0.546(2)	0.473(2)	0.5605(7)	10(1)

Table 7.3 Selected intramolecular distances and bond angles

(a) distances (Å)

atom	atom	distance	atom	atom	distance
Ni(1)	N(1)	1.93(1)	N(7)	C(51)	1.64(3)
Ni(1)	N(2)	1.91(1)	N(8)	C(46)	1.38(3)
Ni(1)	N(3)	1.922(9)	C(1)	C(2)	1.45(2)
Ni(1)	N(4)	1.914(9)	C(1)	C(17)	1.37(2)
Cl(1)	C(48)	1.65(2)	C(2)	C(3)	1.31(2)
Cl(2)	C(48)	1.65(2)	C(2)	C(21)	1.50(2)
Cl(3)	C(48)	1.66(2)	C(3)	C(4)	1.44(2)
O(1)	C(52)	1.80(4)	C(3)	C(22)	1.50(2)
O(2)	C(39)	1.19(2)	C(4)	C(18)	1.39(2)
O(3)	C(38)	1.25(2)	C(5)	C(6)	1.45(2)
N(1)	C(1)	1.36(1)	C(5)	C(18)	1.45(2)
N(1)	C(4)	1.38(1)	C(6)	C(7)	1.33(2)
N(2)	C(5)	1.37(2)	C(6)	C(43)	1.52(2)
N(2)	C(8)	1.38(1)	C(7)	C(8)	1.44(2)
N(3)	C(9)	1.38(1)	C(8)	C(19)	1.36(2)
N(3)	C(12)	1.40(1)	C(9)	C(10)	1.41(2)
N(4)	C(13)	1.39(1)	C(9)	C(19)	1.37(2)
N(4)	C(16)	1.39(1)	C(10)	C(11)	1.33(2)
N(5)	C(36)	1.41(2)	C(10)	C(25)	1.50(2)
N(5)	C(38)	1.34(2)	C(11)	C(12)	1.45(2)
N(6)	C(33)	1.41(2)	C(11)	C(27)	1.51(2)
N(6)	C(39)	1.37(2)	C(12)	C(20)	1.41(1)
C(13)	C(14)	1.45(2)	C(31)	C(33)	1.41(2)
C(13)	C(20)	1.39(1)	C(31)	C(41)	1.36(2)
C(14)	C(15)	1.32(2)	C(32)	C(36)	1.40(2)
C(14)	C(28)	1.49(2)	C(32)	C(40)	1.33(2)
C(15)	C(16)	1.43(2)	C(33)	C(34)	1.37(2)
C(15)	C(29)	1.48(2)	C(34)	C(35)	1.36(2)
C(16)	C(17)	1.36(2)	C(35)	C(42)	1.42(2)
C(18)	C(32)	1.51(2)	C(36)	C(37)	1.39(2)
C(20)	C(31)	1.51(2)	C(37)	C(44)	1.38(2)
C(21)	C(47)	1.51(2)	C(38)	C(50)	1.49(2)
C(23)	C(40)	1.37(2)	C(39)	C(45)	1.52(2)
C(23)	C(44)	1.39(2)	C(41)	C(42)	1.37(2)

Table 7.3 (continued)

(b) angles(°)

atom	atom	atom	angles	atom	atom	atom	angles
N(1)	Ni(1)	N(2)	88.7(4)	C(1)	C(2)	C(3)	108(1)
N(1)	Ni(1)	N(4)	91.7(4)	C(2)	C(3)	C(4)	107(1)
N(2)	Ni(1)	N(3)	92.3(4)	N(1)	C(4)	C(3)	110(1)
N(3)	Ni(1)	N(4)	88.1(4)	C(1)	C(17)	C(16)	126(1)
Ni(1)	N(1)	C(1)	124.5(8)	C(4)	C(18)	C(5)	123(1)
Ni(1)	N(1)	C(4)	129.3(8)	C(4)	C(18)	C(32)	117(1)
C(1)	N(1)	C(4)	106(1)	C(8)	C(19)	C(9)	124(1)
Ni(1)	N(2)	C(5)	129.0(8)	C(12)	C(20)	C(13)	124(1)
Ni(1)	N(2)	C(8)	125.1(8)	C(18)	C(32)	C(36)	122(1)
Ni(1)	N(3)	C(9)	125.1(8)	N(5)	C(36)	C(32)	118(1)
Ni(1)	N(3)	C(12)	131.2(8)	N(5)	C(36)	C(37)	123(1)
Ni(1)	N(4)	C(13)	129.4(8)	N(5)	C(38)	C(50)	116(1)
Ni(1)	N(4)	C(16)	126.9(8)	C(38)	C(50)	C(51)	117(2)
C(36)	N(5)	C(38)	129(1)	N(7)	C(51)	C(50)	109(2)
N(1)	C(1)	C(2)	109(1)				

Table 7.4 U values for $NiCl_3O_3N_8C_{52}H_{61}$

ATOM	U11	U22	U33	U12	U13	U23
Ni(1)	0.0218(8)	0.038(1)	0.0222(9)	-0.002(1)	0.0081(7)	0.000(1)
Cl(1)	0.066(3)	0.138(5)	0.086(4)	-0.027(3)	0.001(3)	-0.023(4)
Cl(2)	0.133(5)	0.119(6)	0.188(6)	0.035(4)	0.102(5)	0.022(5)
Cl(3)	0.138(5)	0.178(7)	0.088(4)	-0.087(5)	0.047(4)	-0.043(4)
O(1)	0.33(4)	0.38(5)	0.47(5)	0.21(3)	-0.23(3)	-0.27(4)
O(2)	0.054(8)	0.18(2)	0.17(1)	0.06(1)	-0.02(1)	-0.08(1)
O(3)	0.049(8)	0.11(1)	0.10(1)	-0.028(8)	-0.006(7)	0.023(9)
C(52)	0.02(1)	0.21(3)	0.13(2)	0.03(1)	-0.03(1)	-0.12(2)
N(1)	0.019(5)	0.048(9)	0.024(6)	0.001(6)	-0.001(5)	0.002(6)
N(2)	0.027(6)	0.06(1)	0.020(6)	-0.007(7)	0.004(5)	-0.001(7)
N(3)	0.015(5)	0.037(7)	0.027(6)	-0.004(6)	0.003(5)	-0.004(6)
N(4)	0.024(5)	0.028(7)	0.019(5)	-0.004(6)	0.001(5)	0.008(6)
N(5)	0.037(7)	0.045(9)	0.045(8)	-0.004(7)	-0.001(6)	0.002(7)
N(6)	0.032(7)	0.04(1)	0.09(1)	0.020(7)	0.010(7)	0.027(8)
N(7)	0.058(9)	0.09(1)	0.050(8)	-0.020(9)	-0.016(7)	0.037(8)
N(8)	0.19(2)	0.18(3)	0.16(2)	0.02(2)	0.04(2)	0.09(2)
C(1)	0.025(7)	0.06(1)	0.016(6)	0.011(8)	0.007(6)	0.017(8)
C(2)	0.033(7)	0.05(1)	0.024(7)	0.008(8)	0.013(6)	-0.010(7)
C(3)	0.029(7)	0.04(1)	0.020(6)	0.012(7)	0.004(6)	0.004(7)
C(4)	0.028(7)	0.03(1)	0.025(7)	0.003(7)	0.004(6)	-0.003(7)
C(5)	0.028(8)	0.05(1)	0.041(9)	0.006(8)	0.012(7)	0.001(8)
C(6)	0.023(8)	0.09(1)	0.04(1)	-0.004(9)	0.002(7)	-0.01(1)
C(7)	0.026(9)	0.16(2)	0.025(8)	-0.01(1)	0.011(7)	-0.04(1)
C(8)	0.018(7)	0.12(2)	0.023(7)	-0.01(1)	0.008(6)	-0.02(1)
C(9)	0.035(7)	0.04(1)	0.021(7)	-0.008(8)	0.011(6)	-0.015(8)
C(10)	0.043(8)	0.03(1)	0.024(7)	-0.000(8)	0.010(6)	-0.000(7)
C(11)	0.036(8)	0.034(9)	0.023(7)	-0.012(8)	0.009(6)	0.002(8)
C(12)	0.015(6)	0.03(1)	0.037(8)	-0.004(6)	-0.005(6)	0.009(7)

[a]The coefficients U_{ij} of the anisotropic temperature factor expression are defined as follows:

$$\exp(-2\pi^2(a^{*2}U_{11}h^2+b^{*2}U_{22}k^2+c^{*2}U_{33}l^2+2a^*b^*U_{12}hk+2a^*c^*U_{13}hl+2b^*c^*U_{23}kl))$$

Table 7.4 (continued)

C(13)	0.016(6)	0.024(8)	0.022(7)	0.004(6)	-0.004(6)	0.005(6)
C(14)	0.021(7)	0.04(1)	0.015(7)	-0.001(7)	0.001(6)	0.010(7)
C(15)	0.031(8)	0.04(1)	0.039(8)	0.006(8)	0.014(7)	0.012(8)
C(16)	0.030(7)	0.019(9)	0.032(8)	0.004(7)	0.009(6)	0.005(7)
C(17)	0.041(8)	0.04(1)	0.016(6)	0.010(8)	0.013(6)	0.007(7)
C(18)	0.016(6)	0.03(1)	0.028(7)	0.003(6)	-0.009(6)	0.004(7)
C(19)	0.028(7)	0.09(1)	0.023(7)	-0.02(1)	0.015(6)	-0.009(9)
C(20)	0.033(8)	0.015(8)	0.027(7)	0.002(6)	0.008(6)	0.008(6)
C(21)	0.040(9)	0.08(1)	0.023(8)	0.01(1)	0.005(7)	-0.004(9)
C(22)	0.06(1)	0.06(1)	0.035(8)	0.01(1)	0.007(7)	-0.00(1)
C(23)	0.06(1)	0.05(1)	0.05(1)	-0.00(1)	0.017(9)	0.007(9)
C(24)	0.16(2)	0.15(3)	0.12(2)	0.09(2)	-0.04(2)	-0.07(2)
C(25)	0.028(8)	0.08(1)	0.021(7)	0.002(8)	0.009(6)	0.013(7)
C(26)	0.07(1)	0.07(1)	0.06(1)	-0.01(1)	0.03(1)	0.00(1)
C(27)	0.035(8)	0.10(1)	0.015(6)	0.00(1)	0.003(6)	0.020(9)
C(28)	0.028(8)	0.06(1)	0.05(1)	-0.012(8)	0.015(7)	-0.012(8)
C(29)	0.026(7)	0.05(1)	0.030(7)	0.001(8)	0.013(6)	0.008(8)
C(30)	0.06(1)	0.11(2)	0.05(1)	0.03(1)	0.054(9)	0.04(1)
C(31)	0.018(7)	0.06(1)	0.011(6)	-0.005(7)	0.002(6)	0.008(7)
C(32)	0.031(8)	0.05(1)	0.021(7)	-0.000(8)	0.007(6)	0.000(7)
C(33)	0.04(1)	0.04(1)	0.036(8)	-0.013(9)	0.020(7)	0.013(8)
C(34)	0.023(8)	0.09(1)	0.04(1)	-0.00(1)	-0.000(7)	0.03(1)
C(35)	0.04(1)	0.11(2)	0.019(8)	-0.02(1)	0.007(7)	0.01(1)
C(36)	0.027(8)	0.06(1)	0.017(7)	0.007(8)	-0.000(6)	-0.003(8)
C(37)	0.033(8)	0.07(1)	0.036(8)	-0.00(1)	0.002(7)	-0.02(1)
C(38)	0.05(1)	0.06(1)	0.07(1)	-0.01(1)	0.01(1)	0.01(1)
C(39)	0.04(1)	0.09(2)	0.05(1)	0.02(1)	-0.01(1)	0.03(1)
C(40)	0.041(9)	0.06(1)	0.027(8)	-0.001(9)	-0.001(7)	0.004(8)
C(41)	0.039(9)	0.04(1)	0.043(9)	-0.005(8)	0.014(8)	-0.013(8)
C(42)	0.05(1)	0.08(1)	0.020(8)	-0.02(1)	0.005(7)	-0.007(9)
C(43)	0.032(9)	0.12(2)	0.034(9)	-0.00(1)	0.021(7)	-0.01(1)
C(44)	0.034(9)	0.07(1)	0.04(1)	0.03(1)	-0.001(8)	0.00(1)
C(45)	0.09(1)	0.05(1)	0.14(2)	-0.00(1)	0.03(1)	0.02(1)
C(46)	0.30(4)	0.06(2)	0.20(3)	-0.07(2)	-0.10(3)	-0.06(2)
C(47)	0.09(1)	0.09(2)	0.08(1)	0.02(1)	0.04(1)	-0.02(1)
C(48)	0.30(4)	0.39(5)	0.40(4)	-0.29(4)	0.34(4)	-0.36(4)
C(49)	0.02(1)	0.11(2)	0.26(3)	-0.02(1)	-0.02(1)	0.03(2)
C(50)	0.09(1)	0.07(1)	0.07(1)	-0.03(1)	0.03(1)	-0.01(1)
C(51)	0.19(3)	0.06(2)	0.09(2)	-0.02(2)	-0.05(2)	0.01(1)

Table 7.5 Least-squares planes $NiCl_3O_3N_8C_{52}H_{61}$

Plane number 1

Atoms Defining Plane	Distance	esd
N1	-0.1064	0.0199
N2	0.1313	0.0231
N3	-0.1107	0.0203
N4	0.0862	0.0197
Additional Atoms	Distance	
NI1	0.0182	

Mean deviation from plane is 0.1087 angstroms

Plane number 2

Atoms Defining Plane	Distance	esd
N1	-0.1025	0.0199
N2	0.1526	0.0231
N3	-0.1304	0.0204
N4	0.0499	0.0197
C1	-0.5223	0.0266
C2	-0.7245	0.0276
C3	-0.2995	0.0249
C4	0.0699	0.0256
C5	0.5270	0.0292
C6	0.7753	0.0344
C7	0.3284	0.0376
C8	-0.0357	0.0372
C9	-0.4761	0.0269
C10	-0.6894	0.0262
C11	-0.4615	0.0274
C12	-0.0877	0.0239
C13	0.3983	0.0217
C14	0.5916	0.0241
C15	0.2392	0.0273
C16	-0.1122	0.0236
C17	-0.5376	0.0268
C18	0.5695	0.0242
C19	-0.4535	0.0303
C20	0.2826	0.0245
Additional Atoms	Distance	
NI1	0.0105	

Mean deviation from plane is 0.3590 angstroms

Dihedral angles between least-squares planes

plane	plane	angle
2	1	0.92

Table 7.5 (continued)

Plane number 3

Atoms Defining Plane	Distance	esd
N1	0.0118	0.0195
C1	-0.0357	0.0259
C2	0.0408	0.0270
C3	-0.0226	0.0249
C4	0.0005	0.0256

Mean deviation from plane is 0.0223 angstroms

Dihedral angles between least-squares planes

plane	plane	angle
3	1	160.39
3	2	159.86

Plane number 4

Atoms Defining Plane	Distance	esd
N2	-0.0229	0.0228
C5	0.0463	0.0291
C6	-0.0493	0.0334
C7	0.0263	0.0355
C8	0.0160	0.0365

Mean deviation from plane is 0.0322 angstroms

Dihedral angles between least-squares planes

plane	plane	angle
4	1	161.41
4	2	160.64
4	3	26.91

Plane number 5

Atoms Defining Plane	Distance	esd
N3	-0.0082	0.0202
C9	0.0130	0.0268
C10	-0.0052	0.0262
C11	-0.0034	0.0274
C12	0.0085	0.0241

Mean deviation from plane is 0.0077 angstroms

Dihedral angles between least-squares planes

plane	plane	angle
5	1	16.45
5	2	16.08
5	3	144.07
5	4	157.64

Table 7.5 (continued)

Plane number 6

Atoms Defining Plane	Distance	esd
N4	0.0286	0.0191
C13	-0.0374	0.0213
C14	0.0325	0.0234
C15	-0.0095	0.0264
C16	-0.0232	0.0230

Mean deviation from plane is 0.0262 angstroms

Dihedral angles between least-squares planes

plane	plane	angle
6	1	17.66
6	2	16.87
6	3	152.80
6	4	143.78
6	5	24.96

Plane number 7

Atoms Defining Plane	Distance	esd
C32	0.0090	0.0217
C36	-0.0085	0.0223
C37	0.0022	0.0236
C44	0.0043	0.0241
C23	-0.0045	0.0268
C40	-0.0049	0.0248

Mean deviation from plane is 0.0056 angstroms

Dihedral angles between least-squares planes

plane	plane	angle
7	1	69.03
7	2	68.72
7	3	91.93
7	4	114.60
7	5	52.65
7	6	72.96

Table 7.5 (continued)

Plane number 8

Atoms Defining Plane	Distance	esd
C31	0.0112	0.0201
C33	-0.0302	0.0227
C34	0.0508	0.0261
C35	-0.0388	0.0251
C42	0.0149	0.0232
C41	-0.0048	0.0215

Mean deviation from plane is 0.0251 angstroms

Dihedral angles between least-squares planes

plane	plane	angle
8	1	109.25
8	2	108.88
8	3	51.55
8	4	75.33
8	5	92.80
8	6	110.16
8	7	40.38

CONCLUSIONS

The attachment of ligating appendages to porphyrins to form multichelating ligands is a relatively straightforward procedure using amino acid peptide coupling methods. It should be possible to vary the length of these ligating appendages by choosing amino acids with different numbers of methylene units between the amine and carbonyl group. The initial studies reported here indicate that molecular building blocks for multi-chelating arrays can be readily prepared and structurally characterized by x-ray crystallography. The extension of this study to form trinuclear complexes will be reported elsewhere [23].

ACKNOWLEDGEMENTS

We thank Dr. Eric Rose for helpful discussions with the amino acid coupling reactions and Jenny Evans Liras, Peter Langr, Ann Marie Dockstadter, Diana Hoganson, and John Tolppi for synthesizing porphyrin precursors. Financial support for this work was provided by the USDOE through the Ames Laboratory.

REFERENCES

1. The Porphyrins; Dolphin, D. Ed.; Vol. 7, Part B, Academic, New York, 1978.

2. Collman, J. P.; Gagne, R. R.; Reed, C. A.; Halbert, T. R.; Lang, G.; Robinson, W. T.; JACS. 1975, 97, 1427.

3. Rodgers, S. J.; Koch, C. A.; Tate, J. R.; Reed, C. A.; Eigenbrot, C. W.; Scheidt, W. R. Inorg. Chem. 1987, 26, 3647.

4. Momenteau, M.; Loock, B.; Mispelter, J.; Bisagni, E. Nouv. J. Chim. 1979, 3, 77.

5. Boitrel, B.; Lecas, A.; Renko, Z.; Rose, E.; New J. Chem. 1989, 13, 73.

6. Dubowchik G. M.; Hamilton, A. D.; J. Chem. Soc. Chem. Comm. 1986, 665

7. Suslick K. S.; Fox, M. M. JACS. 1983, 105, 3507.

8. Gunter, M. J.; McLaughlin, G. M.; Berry, K. J.; Murray, K. S.; Irving, M.; Clark, P. E. Inorg. Chem. 1984, 23, 283.

9. Gunter, M. J.; Mander, L. N.; Murray, K. S.; Clark, P. E. JACS. 1981, 103, 6784.

10. Chang, C. K.; Koo, M. S.; Ward, B. J. Chem. Soc. Chem. Comm. 1982, 716.

11. Elliott, C. M.; Krebs, R. R. JACS. 1982, 104, 4301.

12. Young, R.; Chang, C. K. J. Am. Chem. Soc. 1985, 107, 898.

13. Lindsey, J. J. Org. Chem. 1980, 45, 5215.

14. Elliott, C. M. Anal. Chem. 1980, 52, 666.

15. Aldrich Technical Information Bulletin #Al-125, Aldrich Chemical Company, Wisconsin, 1986.

16. Lecas, A. Renko, Z.; Rose, E. Tetrahedron Let. 1985, 26, 1019.

17. Drago, R. S. "Physical Methods in Chemistry"; Saunders, Philadelphia, 1977, P. 413.

18. Gilmore, C. J. MITHRIL - an integrated direct methods computer program, J. Appl. Cryst., 17 (42-46), University of Glasgow, Scotland, 1984. P. T. Beurskens, DIRDIF: Direct Methods for Difference Structures @ an automatic procedure for phase extension and refinement of difference structure factors. Technical Report 1984/1 Crystallography Laboratory, Toernooiveld, 6525 Ed Nijmegen, Netherlands.

19. Cromer, D. T.; Waber, J. T. International Tables for X-ray Crystallography, Vol. IV, The Kynoch Press, Birmingham, England, 1974, Table 2.2 A.

20. Ibers J. A.; Hamilton, W. C. Acta Crystallgr. 1964, 17, 781.

21. Cromer, D. T. International Tables for X-ray Crystallography, Vol. IV, The Kynoch Press, Birmingham, England, 1974, Table 2.3.1.

22. TEXSAN - TEXRAY Structure analysis package, Molecular Structure Corporation, 1985.

23. Woo L. K.; Maurya, M. R. manuscript in preparation.

24. Fischer, R. X.; Tillman, E. Acta Crystagr. 1988, C44, 775.

25. Meyer Jr., E. F. Acta Crystagr. 1972, 28B, 2162.

26. Hamor, T. A.; Caughey, W. S.; Hoard, J. L. J. Am. Chem. Soc. 1965, 87, 2305.

27. Fleischer, E. B. J. Am. Chem. Soc. 1963, 85, 146.

28. Gallucci, J. C.; Swepston, P. N.; Ibers, J. A. Acta Crystagr. 1982, 38B, 2134.

29. Cullen, D. L.; Meyer, E. F. J. Am. Chem. Soc. 1974, 96, 2095.

30. Pace, L. J.; Martinsen, J.; Ulman, A.; Hoffman B. M.; Ibers, J. A. J. Am. Chem. Soc. 1983, 105, 2612.

SECTION VIII. MINO AND DINUCLEAR COMPLEXES OF A NEW BINUCLEATING PORPHYRIN: CRYSTAL STRUCTURE OF MONONUCLEAR NICKEL(II) COMPLEX

MONO AND DINUCLEAR COMPLEXES OF A NEW BINUCLEATING PORPHYRIN: CRYSTAL STRUCTURE OF MONONUCLEAR NICKEL(II) COMPLEX

Shumei Yang, Robert A. Jacobson

and

Mannar R. Maurya, L. Keith Woo

Department of Chemistry and Ames Laboratory-USDOE

Iowa State University, Ames, Iowa 50011

INTRODUCTION

In the previous paper, a simple synthesis of a new pophyrin muti-chelating ligand, cis-$(ala)_2$DPE, and a single crystal structure of its Ni complex have been reported. The complex, [cis-$(ala)_2$DPE]Ni(II) exihibited two flexible arms which contain the metal binding sites. The terminal group, $-C_2H_2NH_2$, of the two arms were replaced by $-C_4H_4N$ in this paper and two structures containing the new compound, [Ni(DPE)]-$(py)_2.2CHCl_3$ and [Ni(DPE)]-$(py)_2.H_2O$, were determined by single crystal X-ray diffraction. The result indicates that these new arms have an enhanced coordination ability.

EXPERIMENTAL

Synthesis

All reagents used in these syntheses were purchased from Aldrich Chemical Co and used without further purifications. THF was freshly distilled over Na/benzophenone under nitrogen. cis-5,15-bis(o-aminophenyl)-2,8,12,18-tetraethyl-3,7,13,17-tetramethyl porphyrin, cis-[DPE]-$(NH_2)_2$ was synthesized according to the method reported elsewhere[1]. The cis and trans mixture of the porphyrin was converted to cis isomer as reported in our previous paper[2].

^1H NMR spectra were recorded on a Nicolet NIC 300 spectrometer using CD_2Cl_2 as solvent. Chemical shift δ(in ppm) are reported relative to CD_2Cl_3(7.24 ppm). FAB mass spectra were obtained on a Kratos Ms-50 spectrometer. Visible spectra were run at r.t. on a HP 8542A diode array spectrophotometer using CH_2Cl_2 as solvent. IR spectra were run as nujol mulls on an IBM IR-98 Fourier transform infrared spectrophotometer.

cis-5,15-bis-(o-nicatinamidophenyl)-2,8,12,18-tetraethyl-3,7,13,17-tetramethylporphyrin, [H2DPE]-$(py)_2$, **(1)**

To a suspension of HCl salt of nicotinoyl chloride (1.78g, 10mmol) in 450 mL THF was added 6.6 mL triethylamine and reaction

mixture was stirred under nitrogen for 3 h. A freshly prepared solution of cis-[DPE]-$(NH_2)_2$ (0.66g, 1mmol) in 250 mL THF under nitrogen was added to the above solution and reaction mixture was heated at reflux for 15 h under nitrogen with stirring. There after fused CH_3COONa was added to the reaction mixture and heating was continued for next 10 h. After cooling to ambient temperature it was filtered and washed with THF. The combined organic layers were evaporated to dryness. The obtained solid was redissolved in 400 mL CH_2Cl_2, washed successively with water (500 mL), saturated $NaHCO_3$ (500 mL) and water (2 x 500 mL), dried over $MgSO_4$ and concentrated to 10 ml. After addition of 300 mL hexanes, solution was kept in freezer (-10 °C) over night and the separated purple crystalline solid was filtered, washed with hexanes and dried under reduced pressure at ambient temperature. Yield 0.66g, 76%. Anal. Calcd.for $C_{56}H_{56}N_8O_3$: C, 75.68; H, 6.31; N, 12.61%. Found: C, 75.64; H, 6.27; N, 12.51%. UV-vis(CH_2Cl_2): 410(soret), 508, 542, 576 and 626 nm. Fab mass MH^+ = 871.4, calcd.: 871.0. ^1H NMR (CD_2Cl_2): 10.31(s, 2H, meso), 8.96(d, 2H, 2′py), 7.94(m, 6H, 4′py and aryl), 7.82(s ,2H, NH), 7.70(d, 2H, aryl), 7.63(t, 2H, aryl), 6.85(m, 2H, 6′py), 6.43(m, 2H, 5′py), 4.04(q, 8H, $\underline{CH_2}CH_3$), 2.60(s, 12H, CH_3), 1.76(t, 12H, $CH_2\underline{CH_3}$), -2.42(s, NH pyrrole).

[Ni(DPE)]-$(py)_2$ **(2)** and [Cu(DPE)]-$(py)_2$ **(3)**

To a stirred solution of [DPE]-$(py)_2$ (0.25g, 0.28 mmol) in 50 mL $CHCl_3$/MeOH (9:1) was added a freshly prepared solution of the respective metal acetate (0.29 mmol) in 10 ml MeOH with stirring. The resulting reaction mixture was heated at reflux for 10 h. After evaporating the solvent to dryness, the obtained solid was suspended in 250 mL water containing 8 mL 1M HCl and stirred for 2 h. The suspension was extracted with CH_2Cl_2 (2 x 100 mL), washed with water, dried over $MgSO_4$, filtered and concentrated to 5 mL. This solution was layered with 25 mL hexanes and cooled to -10 °C for 4 h. The precipitated colored solid was suction filtered, washed with hexanes and dried in vacuo at ambient temperature.

[Ni(DPE)]-$(py)_2$ Yield: 225mg, 84.2% of red solid. UV-vis(CH_2Cl_2): 408(soret), 530 and 566 nm. Fab mass MH^+ = 927.1, calcd.: 927.69. ^1H NMR (CD_2Cl_2): 9.45(s, 2H, meso), 8.88(d, 2H, 2'py), 8.16(m, 2H, 4'py), 8.09(s, 2H, NH), 7.96(d, 2H, aryl), 7.83(m, 2H, aryl), 7.48(m, 4H, aryl), 6.85(m, 2H, 6'py), 6.57(m, 2H, 5'py), 3.74(m, 8H, $\underline{CH_2}CH_3$), 2.34(s, 12H, CH_3), 1.55(t, 12H, $CH_2\underline{CH_3}$).

[Cu(DPE)]-$(py)_2$. Yield: 230mg, 85.9%. UV-vis(CH_2Cl_2): 410(soret), 534 and 570 nm. Fab mass MH^+ = 932.34, calcd.: 932.54.

X-ray Crystal Structure Determination

Deep purple [Ni(DPE)]-$(py)_2$.$2CHCl_3$ crystals were grown by slow evaporation of $CHCl_3$/hexanes (3:2) solution of [Ni(DPE)]-$(py)_2$ at -10 °C. Crystals of [Ni(DPE)]-$(py)_2$.H_2O were grown by crystallization of the solid, obtained by reacting [(DPE)]-$(py)_2$ with [$Zn(DMSO)_2Cl_2$][3] for 10 h in $CHCl_3$, from DMSO/CH_3OH.

[NI(DPE)]-$(py)_2$.$2CHCL_3$

a single crystal having approximate dimension of 0.40 x 0.40 x 0.35 mm was mounted on a glass fiber using epoxy cement and attached to a standard goniometer head. All measurements were made on a Rigaku AFC6R diffractometer with graphite monochromated Mo Kα radition(0.71069 Å) and a 12 KW rotating anode generator. The data were collected at a temperature of -60 ± 1 °C using the ω-2θ scan technique to a maximum of 2θ value of 55.1°. The cell constants and an orientation matrix for data collection, were obtained from a least-squares refinement of 25 reflections in the range $12.43 < 2\theta < 15.13°$. The unit cell was found to be triclinic with dimensions: a=14.3064, b=14.7195, c=14.296 Å, α=94.863, β=96.383, γ=63.452°. A total of 12582 intensities were measured, and 7581 unique "observed" reflection having $I > 3\sigma(I)$ were used in the structure determination and refinement. The intensities of

three representative reflections were monitored periodically throughout the data collection and show no decay. An empirical absorption correction, based on azimuthal scans of several reflections, was applied, and the data were corrected for Lorentz and polarization effects.

Two molecules per cell were indicated by density considerations. Based on the packing considerations, a statistical analysis of intensity distribution, and the successful solution and refinement of the structure, the space group was determined to be $P\bar{1}$. The position of Ni was located from the three-dimensional Patterson map. The positions of all of other non-hydrogen atoms were located from electron density map obtained after inclusion of the nickel atom, including two chloroform molecules; this yielded a residual index(R) of 0.258. Hydrogen positions were located from ED map and refined isotropically. Full-matrix least-squares refinement of positional and thermal parameters led to convergence with a final unweighted R factor of 0.049 and a weighted R factor of 0.064. Neutral atom scattering factors were taken from literature[4], and corrections for anamalous despersion effects were included[5]; the values for $\Delta f'$ and $\Delta f''$ were those of Cromer[6]. All calculations were done using the TEXSAN crystallographic software package[7], and a molecular diagram was drawed using ORTEP.

[Ni(DPE)]-$(py)_2$.H_2O

The instrumental details are similar to those mentioned above(see Table8.1). The unit cell was found to be monoclinic with dimensions: a=14.2402, b=25.4184, c=14.7255 Å, β=96.383°, and Z=4. A total of 22091(four octants) intensities were measured, and 5635 "observed" reflection having $I > 3\sigma(I)$ were used in the structure determination and refinement(a few reflection were excluded due to interference by beam stop). Patterson method was employed to determine the position of the nickel atom. The remaining atoms were eventually located on electron density maps or difference maps, including a water molecule. All of the hydrogen positions were calculated and included in the refinement. The final unweighted R factor is 0.081 and weighted R factor is 0.107 after full-matrix least-squares refinement of positional and thermal parameters.

Pertinent crystallographic parameters for [Ni(DPE)]-$(py)_2$.$2CHCl_3$ and [Ni(DPE)]-$(py)_2$.H_2O are shown in table 8.1.

Table 8.1 Crystal Data for [Ni(DPE)]-$(py)_2$.$2CHCl_3$ and [Ni(DPE)]-$(py)_2$.H_2O

Empirical Formula	$NiCl_6O_2N_8C_{58}H_{54}$	$NiO_3N_8C_{56}H_{54}$
F.W.	1071.61	945.79
Crystal System	triclinic	monoclinic
a, Å	14.306(4)	14.240(2)
b, Å	14.719(5)	25.418(4)
c, Å	14.296(5)	14.725(5)
α, °	94.86(3)	
β, °	96.38(3)	117.20(6)
γ, °	63.45(2)	
V, $Å^3$	2674(2)	4740(4)
Space Group	P $\bar{1}$	P $2_1/n$
Z value	2	4
ρ_{cal}, g/cm^3	1.331	1.325
Temperature, °C	-60	-50
Radiation, Å	MoKα(0.71069)	MoKα(0.71069)
μ, cm^{-1}	6.12	4.62
Scan Type	ω-2θ	ω
$2\theta_{max}$	55.1°	54.9°
$N_{collect}$	12582	22091
N_{obs}	7581	5645
$N_{variables}$	892	613
R, %	4.9	8.07
R_w, %	6.4	10.72
Max. Peak(ED. Map)	0.70 $e^-/Å^3$	0.98 $e^-/Å^3$

RESULTS AND DISCUSSION

Synthesis of ligand

The condensation of cis-[DPE]-$(NH_2)_2$ with nicotinoylchloride hydrochloride in presence of triethylamine and anhydrous sodium acetate in THF leads to the formation of a new binucleating porphyrin, $[H_2DPE]$-$(py)_2$, **(1)** in 76% yield. No thermal atropisomerization was noticed during coupling reaction though our procedure involves heating of the reaction mixture in THF for several hours. The purity of the crystallized product was established by TLC and ^1H NMR spectrum. The ^1H NMR spectrum of **(1)** readily demonstrates the presence of nicotinamido groups attached to the o-aminophenyl substituents. The 2′-, 6′- and 5′-pyridine protons signal appear at 8.96, 6.85 and 6.43 ppm, respectively, while 4′-pyridine proton signal overlaps with aromatic protons signals at 7.94 ppm. The down field shift of the 2′-H and upfield shift of the 4′-H, 5′-H and 6′-H signals (from those of nicotinamide) compare well with that of meso-tetra[a,a,a,a-(o-nicotinamidophenyl)]porphyrin and thus indicate outward orientation of pyridine nitrogen[8]. The single resonance at 10.26 ppm gives an indication of the purity of the ligand. Elemental analysis and FAB mass spectrum confirm the molecular formula and molecular weight of the ligand, respectively. The

UV/vis spectrum of **(1)** exhibits a soret band at 408 nm and four visible bands at 508, 542, 576 and 626 nm.

Mononuclear complexes

Metallation of the porphyrin core of **(1)** with Ni(II) and Cu(II) was acheived by treating **(1)** with freshly prepared solution of respective metal acetate in refluxing $CHCl_3/CH_3OH$. Completion of the reaction was followed by VU/vis spectrophotometer. The presence of only two Q bands at the completion of the reaction clearly indicated the insertion of metal into the porphyrin core. The possibility of the formation of higher nuclear species was eleminated by treating the crude product with aqueous HCl solution. Finally FAB mass spectra confirm the presence of mononuclear species. In case of Ni(II) ^1H NMR spectrum was also recorded. Absence of the resonance due to the internal pyrrole proton and upfield shift of the meso proton resonance indicate the deprotonation of the internal pyrrole NH groups and subsequent coordination to the nickel atom. Since there are no appreciable shifts of the pyridine protons resonances, one can conclude that the orientation of the N atoms in the pyridine are outward and are same as in free base porphyrin.

Crystal Structure of [Ni(DPE)]-$(py)_2$

The molecular structures of [Ni(DPE)]-$(py)_2.2CHCl_3$ and [Ni(DPE)]-$(py)_2.H_2O$ are shown in Fig. 8.1 and Fig. 8.2, respectively. The final fractional coordinates and temperature factors are collected in Table 8.2 and 8.3, and the least-squares planes are in Table 8.4 and 8.5. The intramolecular bond distances and angles are listed in Table 8.6 and 8.7, respectively. All bond distances and angles of the porphyrin core of the [Ni(DPE)]-$(py)_2$ molecule agree within experimental error with that of [Ni(DPE)]-$(ala)_2$ containing alanyl appended arms[2].

[Ni(DPE)]-$(py)_2.2CHCl_3$ The N-Ni-N bond angles range from 88.5(1) to 91.9(1)° and indicate that the environment around Ni is essentially square planar. The mean deviation from the best least-squares plane, defined by the Ni atom and its four coordinated pyrrole N atoms, is 0.11 Å. The porhyrin core is non-planar and ruffled in a manner similar to the S_4-ruffling of the tetragonal form of Ni(II)(OEP)[9] with an average dihedral angle of 28.6° between the mean planes of the adjacent pyrrole rings. The average $Ni-N_{pyrrole}$ distance of 1.92 Å is in lower limit of the range reported for a majority of a planar nickel(II) porphyrin complexes[9-14]. The meso carbon atoms are displaced alternatively above and below the mean porphyrin plane by +0.57 to -0.52 Å. In the complex [Ni(DPE)]-$(ala)_2$ which has the same

porphyrin core but alanyl appended arms, the C_{20} (meso carbon) bearing a phenyl group is displaced only by 0.19 Å while the other three atoms show a more typical displacement averaging 0.55 Å. The distance between N(7) and N(8) is 11.4 Å and the orientation of the N atoms of the pyridine are outwards. As noted above, the same orientation appears to be present in solution (see text). It is important to mention here that the insertion of the nickel into the porphyrin core has not caused atropisomerization of the appended nicotinamido groups.

[Ni(DPE)]-$(py)_2.H_2O$ The significant structural difference between [Ni(DPE)]-$(py)_2.H_2O$ and[Ni(DPE)]-$(py)_2.2CHCl_3$ is the orientation of N_7 and N_8. The two N atoms are outwards in [Ni(DPE)]-$(py)_2.2CHCl_3$, while inwards in [Ni(DPE)]-$(py)_2.H_2O$, which makes the N_7-N_8 distance is shorter in [Ni(DPE)]-$(py)_2.H_2O$(7.6 Å) than in [Ni(DPE)]-$(py)_2.2CHCl_3$ (11.4 Å). This result can be explained by a consideration of the formation of a dinuclear species, {[Ni(DPE)]-$(py)_2$}$ZnCl_2$. When NiNMP reacted with $Zn(DMSO)_2Cl_2$, N_7 and N_8 were oriented toward Zn(II) due to the coulomb attraction and formed a dinuclear complex. This dinuclear complex was decomposed to mononuclear complex [Ni(DPE)]-$(py)_2.H_2O$ with inwards nitrogen orientation when it is crystallized from DMSO/CH_3OH. Formation of dinuclear species {[Ni(DPE)]-$(py)_2$}$ZnCl_2$ and its decomposition to monomer

[Ni(DPE)]-$(py)_2$ have been confirmed by FAR IR spectra of these complexes(Fig. 8.3).

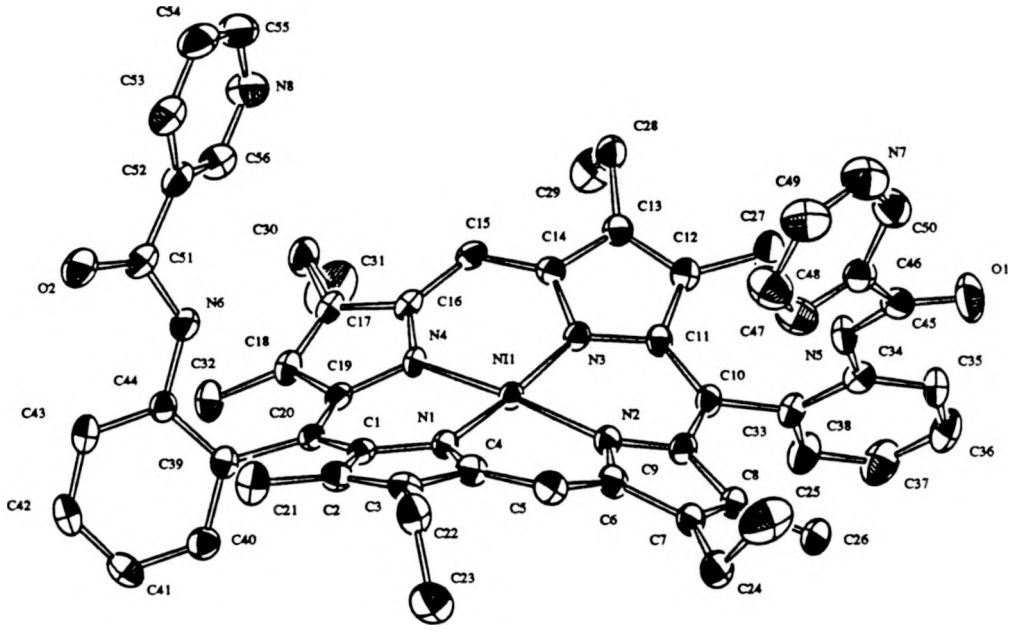

Figure 8.1 The molecular structure of [Ni(DPE)]-$(py)_2.2CHCl_3$. Hydrogen atoms and solvate molecules have been omitted for clarity. Thermal ellipsoids are down at the 50% probability level.

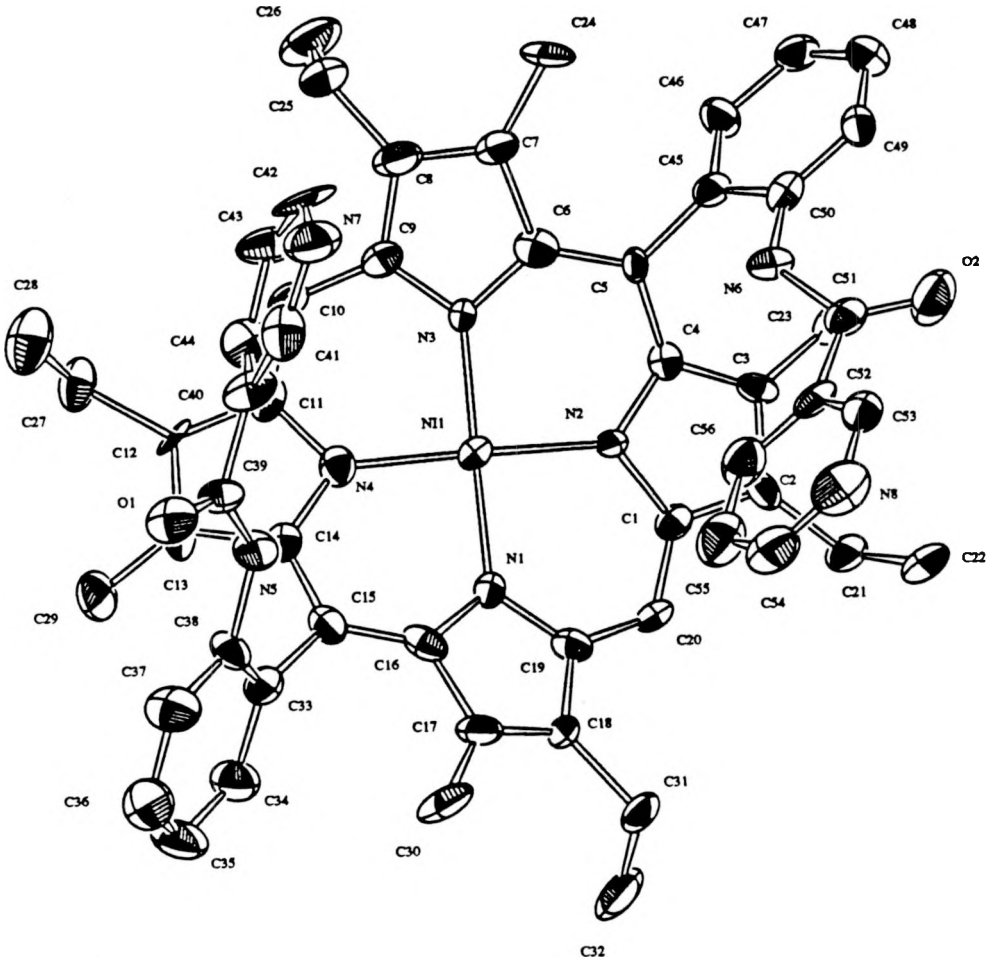

Figure 8.2a Molecular structure and atom numbering scheme for [Ni(DPE)]-$(py)_2.H_2O$. Water molecule and hydrogen atoms have been omitted.

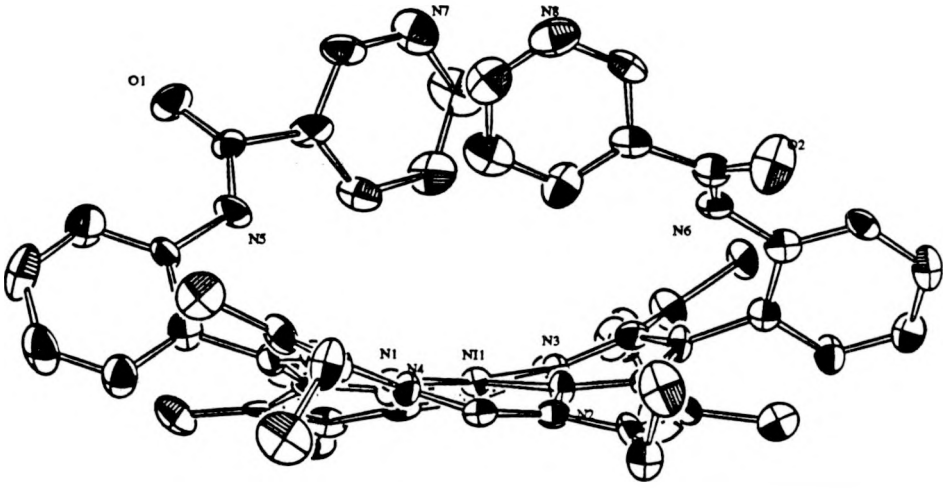

Figure 8.2b N_7 and N_8 are orientated inward by Zn(II) in [Ni(DPE)]-$(py)_2.H_2O$.

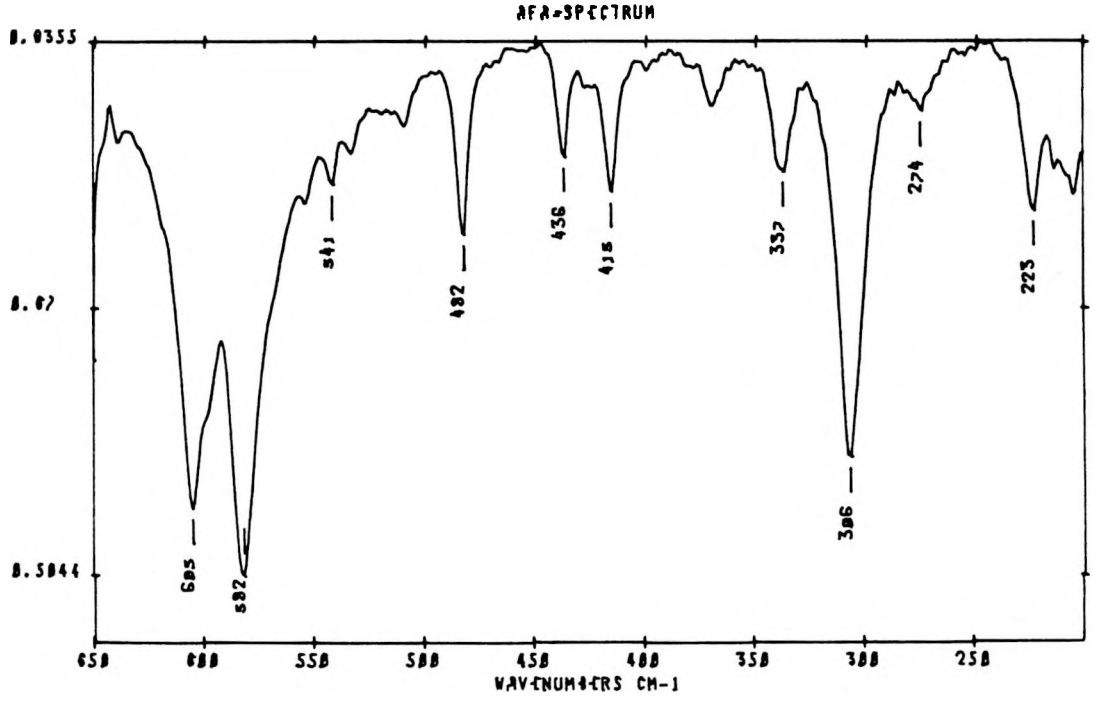

Figure 8.3a IR spectrum of $\{[Ni(DPE)]-(py)_2\}ZnCl_2$ in Nujol mull. υ(M-N) at 605 and 582 cm^{-1} and υ(Zn-Cl) at 306 cm^{-1}.

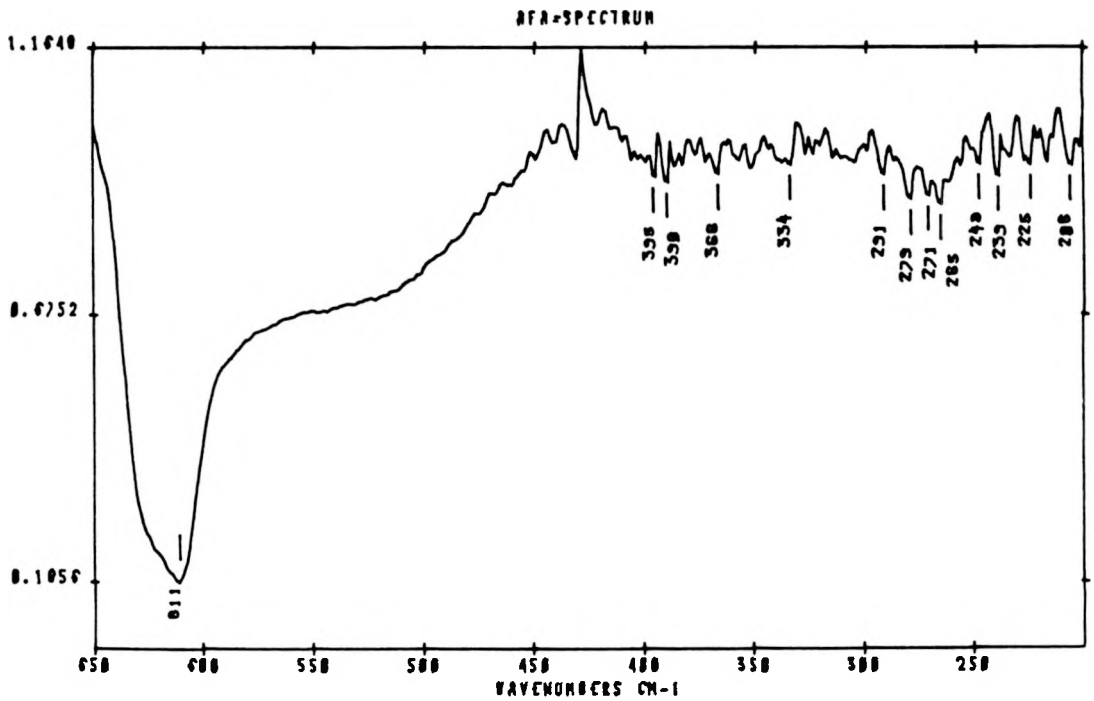

Figure 8.3b IR spectrum of $\{[Ni(DPE)]-(py)_2\}ZnCl_2$ in DMSO. υ(M-N) at 611 cm^{-1}. υ(Zn-Cl) and one of υ(M-N) peaks disappeared.

Table 8.2 Positional parameters and B(eq) for nonhydrogen atoms

(a) $[Ni(DPE)]\text{-}(py)_2.2CHCl_3$

atom	x	y	z	B(eq)[a]
NI1	0.18432(4)	0.07216(4)	0.18070(4)	1.57(3)[b]
CL1	0.6998(1)	0.4610(1)	0.3680(1)	4.6(1)
CL2	0.8560(1)	0.3462(1)	0.5129(1)	5.4(1)
CL3	0.6402(1)	0.4590(1)	0.5532(1)	4.8(1)
CL4	0.2563(1)	0.1915(1)	0.4092(1)	4.4(1)
CL5	0.3345(1)	0.2502(1)	0.5874(1)	5.9(1)
CL6	0.1580(2)	0.3970(1)	0.4835(1)	8.3(2)
O1	0.5337(3)	0.3553(3)	0.3317(3)	4.1(3)
O2	-0.0789(3)	-0.2224(3)	0.3691(2)	3.3(2)
N1	0.2380(3)	-0.0731(3)	0.1810(2)	1.7(2)
N2	0.3208(3)	0.0622(3)	0.1673(2)	1.9(2)
N3	0.1323(3)	0.2169(3)	0.1964(2)	1.8(2)
N4	0.0457(2)	0.0826(2)	0.1789(2)	1.6(2)
N5	0.4205(3)	0.2929(3)	0.2656(3)	2.5(3)
N6	-0.0399(3)	-0.1304(3)	0.2741(3)	2.4(2)
N7	0.5897(4)	0.1818(4)	0.5678(3)	4.0(3)
N8	-0.1851(3)	0.1245(3)	0.4579(3)	3.6(3)
C1	0.1840(3)	-0.1319(3)	0.1740(3)	1.7(2)
C2	0.2556(3)	-0.2366(3)	0.1989(3)	2.0(2)
C3	0.3520(3)	-0.2401(3)	0.2166(3)	2.1(3)
C4	0.3412(3)	-0.1399(3)	0.2018(3)	2.1(2)
C5	0.4233(3)	-0.1174(4)	0.1974(3)	2.3(3)
C6	0.4137(3)	-0.0251(3)	0.1717(3)	2.2(3)
C7	0.4964(3)	-0.0075(4)	0.1415(3)	2.4(3)
C8	0.4551(3)	0.0907(3)	0.1177(3)	2.3(3)
C9	0.3451(3)	0.1367(3)	0.1396(3)	2.0(2)
C10	0.2789(3)	0.2404(3)	0.1484(3)	1.9(2)
C11	0.1819(3)	0.2771(3)	0.1863(3)	1.8(2)
C12	0.1202(3)	0.3798(3)	0.2219(3)	2.1(3)
C13	0.0337(3)	0.3805(3)	0.2532(3)	2.1(3)
C14	0.0394(3)	0.2811(3)	0.2340(3)	1.9(2)

[a] $$B(eq) = \frac{8\pi^2}{3} \sum_{i=1}^{3} \sum_{j=1}^{3} U_{ij} a_i^* a_j^* \vec{a}_i \cdot \vec{a}_j \ .$$

[b] Estimated standard deviations in the least significant figure are given in parentheses in this and succeeding tables.

Table 8.2 (a) (continued)

C15	-0.0432(3)	0.2581(3)	0.2364(3)	2.0(2)
C16	-0.0436(3)	0.1685(3)	0.1991(3)	1.9(2)
C17	-0.1356(3)	0.1527(3)	0.1711(3)	2.0(3)
C18	-0.1024(3)	0.0575(3)	0.1316(3)	2.0(2)
C19	0.0114(3)	0.0108(3)	0.1450(3)	1.7(2)
C20	0.0771(3)	-0.0932(3)	0.1459(3)	1.7(2)
C21	0.2303(4)	-0.3230(4)	0.2105(5)	2.9(3)
C22	0.4537(4)	-0.3295(4)	0.2429(4)	2.9(3)
C23	0.5177(5)	-0.3805(5)	0.1606(5)	3.8(4)
C24	0.6080(4)	-0.0866(4)	0.1370(4)	3.0(3)
C25	0.6778(5)	-0.0818(7)	0.2231(5)	5.0(5)
C26	0.5139(4)	0.1371(5)	0.0756(4)	3.0(3)
C27	0.1459(5)	0.4682(4)	0.2308(5)	3.2(3)
C28	-0.0559(4)	0.4678(4)	0.2972(4)	2.9(3)
C29	-0.1452(5)	0.5265(5)	0.2273(5)	3.8(4)
C30	-0.2468(4)	0.2325(4)	0.1778(5)	3.0(3)
C31	-0.2893(5)	0.3033(6)	0.0965(6)	5.2(5)
C32	-0.1721(4)	0.0157(4)	0.0784(4)	2.7(3)
C33	0.3132(3)	0.3156(3)	0.1209(3)	2.2(3)
C34	0.3831(3)	0.3421(3)	0.1793(3)	2.2(3)
C35	0.4129(4)	0.4123(4)	0.1517(4)	2.8(3)
C36	0.3732(4)	0.4566(4)	0.0660(4)	3.5(4)
C37	0.3041(4)	0.4322(5)	0.0086(4)	3.7(4)
C38	0.2744(4)	0.3621(4)	0.0352(4)	2.9(3)
C39	0.0322(3)	-0.1681(3)	0.1228(3)	1.8(2)
C40	0.0470(4)	-0.2214(4)	0.0370(3)	2.4(3)
C41	0.0147(4)	-0.2967(4)	0.0159(4)	2.9(3)
C42	-0.0316(4)	-0.3207(4)	0.0828(4)	2.8(3)
C43	-0.0494(4)	-0.2680(4)	0.1681(4)	2.6(3)
C44	-0.0197(3)	-0.1903(3)	0.1889(3)	1.9(2)
C45	0.4955(4)	0.2962(4)	0.3315(3)	2.6(3)
C46	0.5282(3)	0.2197(4)	0.4055(3)	2.6(3)
C47	0.5383(4)	0.1217(4)	0.3872(4)	3.5(3)
C48	0.5770(5)	0.0544(5)	0.4600(4)	4.2(4)
C49	0.6014(5)	0.0874(5)	0.5476(4)	4.1(4)
C50	0.5553(4)	0.2455(5)	0.4966(4)	3.4(3)
C51	-0.0738(3)	-0.1448(4)	0.3539(3)	2.3(3)
C52	-0.1052(3)	-0.0563(4)	0.4235(3)	2.4(3)
C53	-0.0904(4)	-0.0740(4)	0.5198(4)	3.0(3)
C54	-0.1225(4)	0.0079(5)	0.5838(4)	3.5(4)
C55	-0.1690(4)	0.1052(5)	0.5499(4)	3.6(4)
C56	-0.1535(4)	0.0443(4)	0.3972(4)	2.9(3)
C57	0.7255(4)	0.3873(4)	0.4669(4)	3.7(4)
C58	0.2229(5)	0.2699(5)	0.5120(4)	3.7(4)

Table 8.2 (continued)

(b) $[Ni(DPE)]\text{-}(py)_2.H_2O$

atom	x	y	z	B(eq)
Ni(1)	0.4446(2)	0.32762(7)	0.3406(2)	1.57(6)
O(1)	0.7791(9)	0.5006(4)	0.7383(8)	3.0(5)
O(2)	0.136(1)	0.4785(5)	-0.094(1)	4.4(6)
N(1)	0.5751(9)	0.3295(5)	0.3296(8)	1.7(4)
N(2)	0.3626(9)	0.3261(5)	0.1939(9)	1.8(5)
N(3)	0.3163(9)	0.3337(4)	0.3522(8)	1.3(4)
N(4)	0.526(1)	0.3183(5)	0.485(1)	2.2(5)
N(5)	0.724(1)	0.4346(5)	0.623(1)	2.4(5)
N(6)	0.172(1)	0.4481(4)	0.069(1)	2.2(5)
N(7)	0.453(1)	0.5443(6)	0.601(1)	4.2(8)
N(8)	0.431(1)	0.5573(6)	0.050(1)	4.8(8)
C(1)	0.401(1)	0.3122(5)	0.125(1)	1.8(6)
C(2)	0.313(1)	0.3031(6)	0.024(1)	2.2(6)
C(3)	0.223(1)	0.3146(5)	0.032(1)	1.7(6)
C(4)	0.255(1)	0.3308(6)	0.136(1)	1.8(5)
C(5)	0.187(1)	0.3533(6)	0.173(1)	1.6(5)
C(6)	0.223(1)	0.3561(6)	0.281(1)	2.1(6)
C(7)	0.151(1)	0.3705(6)	0.325(1)	2.6(7)
C(8)	0.203(1)	0.3477(7)	0.423(1)	3.3(8)
C(9)	0.300(1)	0.3272(6)	0.435(1)	2.3(6)
C(10)	0.380(1)	0.3072(6)	0.530(1)	2.3(6)
C(11)	0.486(1)	0.3025(5)	0.552(1)	2.2(6)
C(12)	0.567(1)	0.2920(5)	0.649(1)	1.9(6)
C(13)	0.664(2)	0.3023(6)	0.652(1)	2.9(7)
C(14)	0.632(1)	0.3209(5)	0.547(1)	1.8(6)
C(15)	0.702(1)	0.3391(6)	0.510(1)	2.5(7)
C(16)	0.672(1)	0.3447(6)	0.406(1)	2.3(6)
C(17)	0.738(1)	0.3610(7)	0.356(1)	3.2(8)
C(18)	0.687(1)	0.3465(6)	0.261(1)	2.3(7)
C(19)	0.585(1)	0.3277(7)	0.242(1)	2.2(6)
C(20)	0.504(1)	0.3140(5)	0.149(1)	1.6(6)
C(21)	0.324(1)	0.2878(6)	-0.068(1)	2.6(7)
C(22)	0.320(1)	0.3344(8)	-0.135(1)	4.3(9)

Table 8.2 (b) (continued)

C(23)	0.113(1)	0.3088(6)	-0.055(1)	2.3(6)
C(24)	0.052(1)	0.4044(7)	0.283(1)	2.9(7)
C(25)	0.160(1)	0.3459(7)	0.500(1)	3.8(9)
C(26)	0.100(2)	0.2939(9)	0.492(2)	5(1)
C(27)	0.555(1)	0.2751(6)	0.742(1)	3.1(7)
C(28)	0.567(2)	0.3218(8)	0.811(1)	5(1)
C(29)	0.770(1)	0.2960(6)	0.737(1)	3.5(8)
C(30)	0.845(1)	0.3876(7)	0.406(1)	3.9(9)
C(31)	0.730(1)	0.3474(8)	0.184(1)	3.7(8)
C(32)	0.793(2)	0.2993(7)	0.190(1)	4(1)
C(33)	0.808(1)	0.3581(6)	0.589(1)	2.6(7)
C(34)	0.900(1)	0.3271(8)	0.608(1)	3.7(8)
C(35)	0.998(2)	0.3453(8)	0.677(2)	4(1)
C(36)	1.009(1)	0.3980(9)	0.728(1)	5(1)
C(37)	0.920(1)	0.4273(7)	0.711(1)	3.4(8)
C(38)	0.821(1)	0.4091(6)	0.643(1)	2.4(6)
C(39)	0.714(1)	0.4750(5)	0.677(1)	1.9(6)
C(40)	0.598(1)	0.4828(6)	0.645(1)	2.9(7)
C(41)	0.555(2)	0.5329(6)	0.629(1)	3.3(8)
C(42)	0.391(2)	0.5047(7)	0.591(2)	4(1)
C(43)	0.422(1)	0.4554(7)	0.607(2)	4.0(9)
C(44)	0.526(1)	0.4427(6)	0.630(1)	3.3(8)
C(45)	0.083(1)	0.3739(6)	0.098(1)	2.2(6)
C(46)	-0.010(1)	0.3454(6)	0.076(1)	2.6(7)
C(47)	-0.106(1)	0.3622(7)	-0.002(1)	2.9(7)
C(48)	-0.113(1)	0.4079(7)	-0.060(1)	3.3(8)
C(49)	-0.021(1)	0.4364(6)	-0.036(1)	2.4(7)
C(50)	0.076(1)	0.4215(7)	0.039(1)	2.7(7)
C(51)	0.199(1)	0.4724(6)	-0.002(1)	2.4(7)
C(52)	0.311(1)	0.4900(6)	0.044(1)	2.2(7)
C(53)	0.328(1)	0.5391(5)	0.014(1)	2.4(6)
C(54)	0.512(2)	0.5275(7)	0.113(2)	3.9(9)
C(55)	0.498(2)	0.4823(7)	0.146(1)	4.0(9)
C(56)	0.396(1)	0.4632(7)	0.111(1)	3.2(8)
O(3)	0.198(2)	0.499(1)	0.743(2)	8(2)

Table 8.3 Anisotropic thermal parameters

(a) [Ni(DPE)]-$(py)_2$.2CHCl3

ATOM	U11	U22	U33	U12	U13	U23
NI1	0.0153(3)	0.0231(3)	0.0220(3)	-0.0093(2)	0.0016(2)	0.0008(2)
CL1	0.063(1)	0.065(1)	0.057(1)	-0.0348(8)	0.0049(8)	0.0103(8)
CL2	0.0436(9)	0.051(1)	0.103(1)	-0.0130(7)	-0.0022(9)	0.0145(9)
CL3	0.057(1)	0.071(1)	0.058(1)	-0.0291(8)	0.0178(8)	-0.0067(8)
CL4	0.070(1)	0.0501(8)	0.0459(9)	-0.0257(8)	0.0007(7)	-0.0018(7)
CL5	0.061(1)	0.091(1)	0.065(1)	-0.033(1)	-0.0118(8)	-0.007(1)
CL6	0.140(2)	0.056(1)	0.061(1)	0.001(1)	-0.017(1)	-0.0055(9)
O1	0.058(2)	0.066(3)	0.052(2)	-0.050(2)	-0.009(2)	0.007(2)
O2	0.053(2)	0.043(2)	0.039(2)	-0.026(2)	0.010(2)	0.010(2)
N1	0.017(2)	0.024(2)	0.023(2)	-0.009(1)	0.002(1)	0.001(1)
N2	0.019(2)	0.026(2)	0.029(2)	-0.011(2)	0.003(2)	-0.002(2)
N3	0.017(2)	0.025(2)	0.025(2)	-0.010(2)	0.003(1)	0.001(1)
N4	0.016(2)	0.023(2)	0.023(2)	-0.011(1)	0.000(1)	0.004(1)
N5	0.032(2)	0.035(2)	0.037(2)	-0.024(2)	-0.002(2)	0.004(2)
N6	0.035(2)	0.028(2)	0.033(2)	-0.018(2)	0.011(2)	0.000(2)
N7	0.048(3)	0.059(3)	0.038(3)	-0.019(2)	-0.006(2)	0.003(2)
N8	0.046(3)	0.044(3)	0.410(3)	-0.016(2)	0.011(2)	-0.004(2)
C1	0.023(2)	0.024(2)	0.018(2)	-0.010(2)	0.004(2)	0.000(2)
C2	0.024(2)	0.025(2)	0.025(2)	-0.009(2)	0.002(2)	0.000(2)
C3	0.027(2)	0.025(2)	0.023(2)	-0.007(2)	-0.001(2)	0.000(2)
C4	0.020(2)	0.028(2)	0.026(2)	-0.008(2)	-0.001(2)	0.000(2)
C5	0.014(2)	0.030(2)	0.035(3)	-0.004(2)	-0.002(2)	-0.002(2)
C6	0.018(2)	0.034(3)	0.032(3)	-0.013(2)	-0.001(2)	-0.003(2)
C7	0.019(2)	0.036(3)	0.039(3)	-0.014(2)	0.006(2)	-0.009(2)
C8	0.022(2)	0.036(3)	0.034(3)	-0.018(2)	0.006(2)	-0.007(2)
C9	0.018(2)	0.033(2)	0.027(2)	-0.013(2)	0.001(2)	-0.000(2)
C10	0.020(2)	0.032(2)	0.025(2)	-0.016(2)	-0.002(2)	0.003(2)
C11	0.020(2)	0.026(2)	0.025(2)	-0.013(2)	-0.003(2)	0.003(2)
C12	0.025(2)	0.026(2)	0.029(2)	-0.012(2)	0.001(2)	0.004(2)
C13	0.025(2)	0.027(2)	0.026(2)	-0.012(2)	0.002(2)	0.000(2)
C14	0.025(2)	0.027(2)	0.023(2)	-0.012(2)	0.003(2)	-0.002(2)
C15	0.021(2)	0.024(2)	0.027(2)	-0.007(2)	0.008(2)	0.000(2)

[a]The coefficients U_{ij} of the anisotropic temperature factor expression are defined as follows:

$$\exp(-2\pi^2(a^{*2}U_{11}h^2+b^{*2}U_{22}k^2+c^{*2}U_{33}l^2+2a^*b^*U_{12}hk+2a^*c^*U_{13}hl+2b^*c^*U_{23}kl))$$

Table 8.3 (a) (continued)

C16	0.020(2)	0.028(2)	0.025(2)	-0.010(2)	0.005(2)	0.005(2)
C17	0.020(2)	0.031(2)	0.029(2)	-0.013(2)	0.004(2)	0.007(2)
C18	0.021(2)	0.029(2)	0.028(2)	-0.013(2)	-0.002(2)	0.009(2)
C19	0.021(2)	0.031(2)	0.017(2)	-0.014(2)	0.002(2)	0.003(2)
C20	0.022(2)	0.026(2)	0.018(2)	-0.013(2)	0.003(2)	-0.000(2)
C21	0.027(3)	0.027(3)	0.054(4)	-0.009(2)	0.001(3)	0.010(2)
C22	0.023(3)	0.030(3)	0.052(4)	-0.009(2)	-0.002(2)	0.002(3)
C23	0.034(3)	0.037(3)	0.063(4)	-0.006(3)	0.006(3)	-0.007(3)
C24	0.021(2)	0.038(3)	0.054(4)	-0.013(2)	0.009(2)	-0.009(3)
C25	0.027(3)	0.089(6)	0.058(4)	-0.010(4)	0.001(3)	0.008(4)
C26	0.027(3)	0.047(3)	0.048(3)	-0.022(3)	0.012(2)	-0.009(3)
C27	0.029(3)	0.028(3)	0.065(4)	-0.013(2)	0.011(3)	0.001(3)
C28	0.034(3)	0.028(3)	0.051(3)	-0.017(2)	0.016(2)	-0.007(2)
C29	0.035(3)	0.038(3)	0.060(4)	-0.004(3)	0.008(3)	0.012(3)
C30	0.023(3)	0.038(3)	0.054(4)	-0.016(2)	0.009(2)	-0.004(3)
C31	0.030(3)	0.058(4)	0.089(6)	0.003(3)	0.003(3)	0.032(4)
C32	0.024(3)	0.040(3)	0.044(3)	-0.019(2)	-0.005(2)	0.007(3)
C33	0.023(2)	0.032(2)	0.032(3)	-0.015(2)	0.003(2)	0.004(2)
C34	0.027(2)	0.029(2)	0.029(3)	-0.012(2)	0.004(2)	0.002(2)
C35	0.036(3)	0.038(3)	0.044(3)	-0.027(2)	0.004(2)	0.001(2)
C36	0.051(3)	0.047(3)	0.051(4)	-0.032(3)	0.011(3)	0.012(3)
C37	0.046(3)	0.060(4)	0.039(3)	-0.026(3)	-0.002(3)	0.021(3)
C38	0.030(3)	0.050(3)	0.037(3)	-0.022(2)	-0.002(2)	0.012(2)
C39	0.017(2)	0.025(2)	0.026(2)	-0.009(2)	-0.002(2)	0.004(2)
C40	0.032(3)	0.035(3)	0.025(3)	-0.016(2)	0.002(2)	0.003(2)
C41	0.042(3)	0.038(3)	0.030(3)	-0.021(2)	-0.003(2)	-0.005(2)
C42	0.036(3)	0.032(3)	0.044(3)	-0.022(2)	-0.004(2)	0.001(2)
C43	0.031(3)	0.033(3)	0.041(3)	-0.020(2)	0.003(2)	0.006(2)
C44	0.019(2)	0.029(2)	0.026(2)	-0.012(2)	0.001(2)	0.001(2)
C45	0.031(3)	0.041(3)	0.029(3)	-0.018(2)	0.004(2)	-0.006(2)
C46	0.023(2)	0.041(3)	0.033(3)	-0.014(2)	0.002(2)	-0.002(2)
C47	0.047(3)	0.043(3)	0.036(3)	-0.017(3)	-0.003(2)	0.000(2)
C48	0.064(4)	0.042(3)	0.050(4)	-0.021(3)	-0.001(3)	0.003(3)
C49	0.052(4)	0.053(4)	0.040(3)	-0.012(3)	-0.003(3)	0.010(3)
C50	0.042(3)	0.045(3)	0.040(3)	-0.021(3)	-0.001(2)	-0.003(3)
C51	0.024(2)	0.038(3)	0.027(2)	-0.013(2)	0.003(2)	0.010(2)
C52	0.022(2)	0.042(3)	0.028(2)	-0.015(2)	0.003(2)	0.006(2)
C53	0.032(3)	0.048(3)	0.037(3)	-0.017(2)	0.002(2)	0.012(3)
C54	0.043(3)	0.064(4)	0.027(3)	-0.025(3)	0.006(2)	0.004(3)
C55	0.041(3)	0.058(4)	0.038(3)	-0.022(3)	0.011(2)	-0.011(3)
C56	0.035(3)	0.041(3)	0.032(3)	-0.015(2)	0.007(2)	0.004(2)
C57	0.045(3)	0.042(3)	0.059(4)	-0.022(3)	0.009(3)	-0.003(3)
C58	0.044(3)	0.063(4)	0.038(3)	-0.028(3)	0.004(3)	0.003(3)

Table 8.3 (continued)

(b) [Ni(DPE)]-$(py)_2.H_2O$

ATOM	U11	U22	U33	U12	U13	U23
Ni(1)	0.023(1)	0.020(1)	0.021(1)	-0.001(1)	0.0135(8)	-0.001(1)
O(1)	0.040(7)	0.035(7)	0.037(7)	-0.010(6)	0.016(6)	-0.015(6)
O(2)	0.053(9)	0.08(1)	0.037(8)	-0.022(8)	0.024(7)	0.004(7)
N(1)	0.022(7)	0.023(7)	0.018(7)	0.003(6)	0.008(6)	-0.006(6)
N(2)	0.017(6)	0.033(7)	0.021(7)	0.002(6)	0.012(6)	-0.008(6)
N(3)	0.019(7)	0.017(7)	0.015(7)	0.000(6)	0.008(6)	-0.002(5)
N(4)	0.030(8)	0.031(9)	0.015(7)	0.003(6)	0.005(6)	-0.001(6)
N(5)	0.031(8)	0.026(7)	0.035(8)	0.012(6)	0.015(7)	-0.003(6)
N(6)	0.035(8)	0.013(7)	0.05(1)	0.001(6)	0.030(8)	0.007(6)
N(7)	0.07(1)	0.05(1)	0.06(1)	0.01(1)	0.04(1)	-0.001(8)
N(8)	0.09(1)	0.04(1)	0.09(1)	-0.03(1)	0.07(1)	-0.02(1)
C(1)	0.03(1)	0.022(9)	0.024(9)	0.002(7)	0.017(8)	-0.003(6)
C(2)	0.02(1)	0.028(9)	0.03(1)	0.009(7)	0.011(8)	0.010(7)
C(3)	0.014(8)	0.016(8)	0.03(1)	0.002(6)	0.010(7)	0.003(6)
C(4)	0.020(8)	0.026(8)	0.020(8)	0.004(8)	0.006(7)	-0.009(7)
C(5)	0.015(8)	0.030(9)	0.011(8)	-0.004(6)	0.003(7)	0.001(6)
C(6)	0.03(1)	0.05(1)	0.03(1)	-0.009(8)	0.036(9)	-0.016(7)
C(7)	0.03(1)	0.04(1)	0.03(1)	0.013(8)	0.02(1)	0.013(8)
C(8)	0.02(1)	0.07(1)	0.04(1)	-0.003(9)	0.02(1)	-0.02(1)
C(9)	0.030(9)	0.04(1)	0.03(1)	-0.007(9)	0.023(8)	-0.001(9)
C(10)	0.03(1)	0.03(1)	0.03(1)	-0.006(7)	0.018(9)	0.001(7)
C(11)	0.05(1)	0.017(8)	0.03(1)	-0.003(7)	0.02(1)	-0.006(7)
C(12)	0.04(1)	0.024(8)	0.019(9)	0.003(8)	0.023(8)	0.002(7)
C(13)	0.07(1)	0.014(8)	0.014(9)	0.003(8)	0.01(1)	0.001(6)
C(14)	0.04(1)	0.010(8)	0.030(9)	0.000(7)	0.021(8)	-0.000(7)
C(15)	0.03(1)	0.04(1)	0.03(1)	0.009(8)	0.007(8)	-0.009(7)
C(16)	0.02(1)	0.020(9)	0.04(1)	-0.000(7)	0.01(1)	-0.011(7)
C(17)	0.03(1)	0.05(1)	0.05(1)	0.015(9)	0.03(1)	0.02(1)
C(18)	0.03(1)	0.05(1)	0.010(8)	0.006(8)	0.013(8)	-0.004(7)
C(19)	0.015(8)	0.04(1)	0.03(1)	0.003(8)	0.009(7)	0.003(9)
C(20)	0.024(9)	0.026(9)	0.022(9)	-0.001(6)	0.020(8)	-0.001(6)
C(21)	0.04(1)	0.04(1)	0.03(1)	0.005(8)	0.025(9)	-0.007(8)
C(22)	0.04(1)	0.10(2)	0.04(1)	0.00(1)	0.03(1)	0.01(1)
C(23)	0.04(1)	0.03(1)	0.03(1)	-0.000(7)	0.023(9)	0.002(7)
C(24)	0.012(8)	0.05(1)	0.05(1)	0.008(8)	0.02(1)	-0.006(9)
C(25)	0.04(1)	0.07(1)	0.04(1)	0.00(1)	0.03(1)	-0.00(1)

Table 8.3 (b) (continued)

C(26)	0.07(2)	0.10(2)	0.07(2)	-0.02(1)	0.06(1)	0.00(1)
C(27)	0.07(1)	0.02(1)	0.03(1)	-0.001(9)	0.02(1)	-0.002(7)
C(28)	0.10(2)	0.05(1)	0.04(1)	-0.01(1)	0.04(1)	-0.00(1)
C(29)	0.05(1)	0.03(1)	0.04(1)	0.012(9)	0.01(1)	0.015(8)
C(30)	0.05(1)	0.07(1)	0.05(1)	-0.00(1)	0.04(1)	-0.01(1)
C(31)	0.03(1)	0.10(2)	0.02(1)	-0.02(1)	0.014(9)	0.00(1)
C(32)	0.08(2)	0.06(1)	0.05(1)	0.02(1)	0.05(1)	0.00(1)
C(33)	0.04(1)	0.04(1)	0.03(1)	0.004(8)	0.016(9)	-0.004(8)
C(34)	0.03(1)	0.07(1)	0.04(1)	0.01(1)	0.01(1)	0.00(1)
C(35)	0.04(1)	0.07(1)	0.06(1)	0.02(1)	0.02(1)	-0.01(1)
C(36)	0.03(1)	0.10(2)	0.03(1)	-0.02(1)	0.00(1)	-0.02(1)
C(37)	0.03(1)	0.06(1)	0.04(1)	-0.001(9)	0.01(1)	-0.02(1)
C(38)	0.03(1)	0.04(1)	0.02(1)	0.013(8)	0.006(8)	-0.002(7)
C(39)	0.03(1)	0.012(8)	0.05(1)	0.002(7)	0.029(9)	0.002(7)
C(40)	0.05(1)	0.017(9)	0.06(1)	-0.006(8)	0.04(1)	-0.024(8)
C(41)	0.06(1)	0.02(1)	0.04(1)	0.01(1)	0.02(1)	-0.008(8)
C(42)	0.07(1)	0.04(1)	0.10(2)	0.01(1)	0.08(1)	0.02(1)
C(43)	0.04(1)	0.04(1)	0.09(2)	-0.01(1)	0.06(1)	0.00(1)
C(44)	0.05(1)	0.02(1)	0.05(1)	0.013(8)	0.03(1)	0.001(8)
C(45)	0.020(9)	0.04(1)	0.02(1)	0.001(7)	0.012(8)	-0.015(7)
C(46)	0.02(1)	0.04(1)	0.03(1)	0.001(7)	0.009(9)	0.007(7)
C(47)	0.03(1)	0.06(1)	0.03(1)	-0.010(8)	0.02(1)	-0.004(9)
C(48)	0.03(1)	0.06(1)	0.03(1)	0.01(1)	0.01(1)	-0.01(1)
C(49)	0.03(1)	0.03(1)	0.02(1)	0.012(8)	0.010(9)	-0.005(7)
C(50)	0.04(1)	0.04(1)	0.03(1)	0.001(9)	0.02(1)	-0.001(8)
C(51)	0.03(1)	0.02(1)	0.04(1)	0.002(7)	0.03(1)	-0.011(8)
C(52)	0.05(1)	0.02(1)	0.03(1)	-0.003(8)	0.04(1)	-0.012(7)
C(53)	0.04(1)	0.019(8)	0.04(1)	0.014(8)	0.03(1)	0.007(7)
C(54)	0.06(1)	0.04(1)	0.06(1)	0.00(1)	0.04(1)	-0.00(1)
C(55)	0.07(2)	0.04(1)	0.05(1)	0.01(1)	0.04(1)	0.00(1)
C(56)	0.05(1)	0.04(1)	0.04(1)	-0.00(1)	0.02(1)	0.009(9)
O(3)	0.11(2)	0.10(2)	0.14(3)	-0.00(2)	0.09(2)	0.11(2)

Table 8.4 Intramolecular distances(Å) involving the nonhydrogen atoms

(a) $[Ni(DPE)]-(py)_2.2CHCL_3$

atom	atom	distance	atom	atom	distance
NI1	N1	1.922(4)	N8	C55	1.343(7)
NI1	N2	1.921(4)	N8	C56	1.336(6)
NI1	N3	1.919(4)	C1	C2	1.467(6)
NI1	N4	1.917(3)	C1	C20	1.396(6)
CL1	C57	1.760(6)	C2	C3	1.353(6)
CL2	C57	1.752(6)	C2	C21	1.496(7)
CL3	C57	1.758(6)	C3	C4	1.444(6)
CL4	C58	1.758(6)	C3	C22	1.496(6)
CL5	C58	1.746(6)	C4	C5	1.365(6)
CL6	C58	1.738(6)	C5	C6	1.380(6)
O1	C45	1.215(6)	C6	C7	1.435(6)
O2	C51	1.216(5)	C7	C8	1.353(6)
N1	C1	1.386(5)	C7	C24	1.502(6)
N1	C4	1.375(5)	C8	C9	1.467(6)
N2	C6	1.375(5)	C8	C26	1.494(7)
N2	C9	1.389(5)	C9	C10	1.394(6)
N3	C11	1.384(5)	C10	C11	1.399(6)
N3	C14	1.377(5)	C10	C33	1.492(6)
N4	C16	1.375(5)	C11	C12	1.449(6)
N4	C19	1.384(5)	C12	C13	1.358(6)
N5	C34	1.411(6)	C12	C27	1.495(7)
N5	C45	1.363(6)	C13	C14	1.433(6)
N6	C44	1.418(6)	C13	C28	1.503(6)
N6	C51	1.356(6)	C14	C15	1.372(6)
N7	C49	1.333(7)	C15	C16	1.382(6)
N7	C50	1.340(7)	C16	C17	1.445(6)
C17	C18	1.355(6)	C48	C49	1.370(8)
C17	C30	1.504(6)	C51	C52	1.498(7)
C18	C19	1.453(6)	C52	C53	1.398(7)
C18	C32	1.500(6)	C52	C56	1.391(7)
C19	C20	1.393(6)	C53	C54	1.383(7)
C20	C39	1.502(6)	C54	C55	1.386(8)
C22	C23	1.503(8)	C24	C25	1.514(9)
C28	C29	1.501(8)	C30	C31	1.512(9)
C33	C34	1.398(6)	C33	C38	1.389(6)

Table 8.4 (a) (continued)

C34	C35	1.381(6)	C35	C36	1.378(7)
C36	C37	1.366(8)	C37	C38	1.373(7)
C39	C40	1.383(6)	C39	C44	1.406(6)
C40	C41	1.381(7)	C41	C42	1.373(7)
C42	C43	1.373(7)	C43	C44	1.387(6)
C45	C46	1.493(7)	C46	C47	1.389(7)
C46	C50	1.387(7)	C47	C48	1.388(8)

(b) $[Ni(DPE)]\text{-}(py)_2.H_2O$

atom	atom	distance	atom	atom	distance
NI1	N1	1.94(1)	C3	C4	1.45(2)
NI1	N2	1.93(1)	C3	C23	1.50(2)
NI1	N3	1.92(1)	C4	C5	1.43(3)
NI1	N4	1.92(1)	C5	C6	1.42(2)
O1	C39	1.16(2)	C5	C45	1.48(2)
O2	C51	1.24(2)	C6	C7	1.50(3)
N1	C16	1.38(2)	C7	C8	1.41(2)
N1	C19	1.37(2)	C7	C24	1.53(2)
N2	C1	1.40(2)	C8	C9	1.42(3)
N2	C4	1.38(2)	C8	C25	1.51(3)
N3	C6	1.39(2)	C9	C10	1.42(2)
N3	C9	1.35(2)	C10	C11	1.40(3)
N4	C11	1.41(3)	C11	C12	1.39(2)
N4	C14	1.36(2)	C12	C13	1.39(3)
N5	C38	1.43(2)	C12	C27	1.51(3)
N5	C39	1.35(2)	C13	C14	1.47(2)
N6	C50	1.40(2)	C13	C29	1.46(2)
N6	C51	1.41(3)	C14	C15	1.41(3)
N7	C41	1.34(3)	C15	C16	1.38(3)

Table 8.4 (b) (continued)

N7	C42	1.30(3)	C15	C33	1.51(2)
N8	C53	1.40(3)	C16	C17	1.51(3)
N8	C54	1.34(2)	C17	C18	1.29(2)
C1	C2	1.45(2)	C17	C30	1.51(2)
C1	C20	1.35(2)	C18	C19	1.44(2)
C2	C3	1.38(3)	C18	C31	1.52(3)
C2	C21	1.49(3)	C19	C20	1.37(2)
C21	C22	1.52(3)	C25	C26	1.55(3)
C27	C28	1.52(3)	C31	C32	1.49(3)
C33	C34	1.44(3)	C33	C38	1.49(2)
C34	C35	1.38(2)	C35	C36	1.51(3)
C36	C37	1.39(3)	C37	C38	1.38(2)
C39	C40	1.51(3)	C40	C41	1.39(2)
C40	C44	1.39(2)	C42	C43	1.31(3)
C43	C44	1.40(3)	C45	C46	1.41(2)
C45	C50	1.47(2)	C46	C47	1.39(2)
C48	C49	1.40(3)	C47	C48	1.42(3)
C49	C50	1.37(2)	C51	C52	1.48(2)
C52	C53	1.38(2)	C52	C56	1.35(2)
C54	C55	1.31(3)	C55	C56	1.38(3)

Table 8.5 Intramolecular angles(°) involving the nonhydrogen atoms

(a) $[Ni(DPE)]-(py)_2.2CHCL_3$

atom	atom	atom	angle	atom	atom	atom	angle
N1	NI1	N2	91.9(1)	C1	C2	C21	128.7(4)
N1	NI1	N3	173.2(1)	C3	C2	C21	124.8(4)
N1	NI1	N4	88.5(1)	C2	C3	C4	107.1(4)
N2	NI1	N3	88.9(1)	C2	C3	C22	128.4(5)
N2	NI1	N4	173.5(2)	C4	C3	C22	124.5(4)
N3	NI1	N4	91.4(1)	N1	C4	C3	111.1(4)
NI1	N1	C1	129.4(3)	N1	C4	C5	124.0(4)
NI1	N1	C4	125.0(3)	C3	C4	C5	124.4(4)
C1	N1	C4	105.1(3)	C4	C5	C6	124.6(4)
NI1	N2	C6	126.1(3)	N2	C6	C5	123.9(4)
NI1	N2	C9	127.8(3)	N2	C6	C7	110.6(4)
C6	N2	C9	105.6(3)	C5	C6	C7	125.5(4)
NI1	N3	C11	129.4(3)	C6	C7	C8	107.9(4)
NI1	N3	C14	124.7(3)	C6	C7	C24	124.7(4)
C11	N3	C14	105.3(3)	C8	C7	C24	127.4(4)
NI1	N4	C16	126.6(3)	C7	C8	C9	106.0(4)
NI1	N4	C19	127.7(3)	C7	C8	C26	124.4(4)
C16	N4	C19	105.2(3)	C9	C8	C26	129.5(4)
C34	N5	C45	129.2(4)	N2	C9	C8	109.6(4)
C44	N6	C51	129.3(4)	N2	C9	C10	123.2(4)
C49	N7	C50	116.9(5)	C8	C9	C10	126.3(4)
C55	N8	C56	117.0(5)	C9	C10	C11	122.0(4)
N1	C1	C2	110.1(4)	C9	C10	C33	119.7(4)
N1	C1	C20	122.8(4)	C11	C10	C33	118.3(4)
C2	C1	C20	127.1(4)	N3	C11	C10	123.2(4)
C1	C2	C3	106.4(4)	N3	C11	C12	110.3(4)
C10	C11	C12	126.4(4)	C3	C22	C23	113.5(5)
C11	C12	C13	106.3(4)	C7	C24	C25	112.6(5)
C11	C12	C27	129.0(4)	C13	C28	C29	113.5(5)
C13	C12	C27	124.6(4)	C17	C30	C31	114.1(5)
C12	C13	C14	107.5(4)	C10	C33	C34	122.0(4)
C12	C13	C28	128.3(4)	C10	C33	C38	119.6(4)
C14	C13	C28	124.2(4)	C34	C33	C38	118.4(4)
N3	C14	C13	110.5(4)	N5	C34	C33	116.4(4)
N3	C14	C15	124.1(4)	N5	C34	C35	123.1(4)
C13	C14	C15	124.4(4)	C33	C34	C35	120.5(4)
C14	C15	C16	123.7(4)	C34	C35	C36	119.5(5)

Table 8.5 (a) (continued)

N4	C16	C15	123.6(4)	C35	C36	C37	120.7(5)
N4	C16	C17	110.4(4)	C36	C37	C38	120.3(5)
C15	C16	C17	125.9(4)	C33	C38	C37	120.7(5)
C16	C17	C18	107.3(4)	C20	C39	C40	119.9(4)
C16	C17	C30	124.8(4)	C20	C39	C44	121.5(4)
C18	C17	C30	127.7(4)	C40	C39	C44	118.4(4)
C17	C18	C19	106.1(4)	C39	C40	C41	121.9(5)
C17	C18	C32	125.1(4)	C40	C41	C42	119.0(5)
C19	C18	C32	128.7(4)	C41	C42	C43	120.7(5)
N4	C19	C18	110.2(4)	C42	C43	C44	120.7(5)
N4	C19	C20	122.4(4)	N6	C44	C39	117.5(4)
C18	C19	C20	125.8(4)	N6	C44	C43	123.3(4)
C1	C20	C19	122.2(4)	C39	C44	C43	119.3(4)
C1	C20	C39	117.6(4)	O1	C45	N5	124.3(5)
C19	C20	C39	120.1(4)	O1	C45	C46	121.8(4)
N5	C45	C46	113.9(4)	C51	C52	C56	123.2(4)
C45	C46	C47	123.4(4)	C53	C52	C56	117.4(5)
C45	C46	C50	118.7(5)	C47	C46	C50	117.8(5)
C46	C47	C48	118.5(5)	C47	C48	C49	119.1(6)
N7	C49	C48	123.6(6)	N7	C50	C46	124.0(5)
O2	C51	N6	123.7(5)	O2	C51	C52	121.8(4)
N6	C51	C52	114.4(4)	C51	C52	C53	119.4(4)
C52	C53	C54	119.2(5)	C53	C54	C55	118.6(5)
N8	C55	C54	123.4(5)	N8	C56	C52	124.3(5)
CL1	C57	CL2	110.5(3)	CL1	C57	CL3	109.8(3)
CL2	C57	CL3	110.1(3)	CL4	C58	CL5	111.0(3)
CL4	C58	CL6	110.4(3)	CL5	C58	CL6	109.4(3)

(b) $[Ni(DPE)]\text{-}(py)_2.H_2O$

atom	atom	atom	angle	atom	atom	atom	angle
N1	NI1	N2	91.1(5)	C1	C2	C21	125(2)
N1	NI1	N3	173.9(5)	C3	C2	C21	128(1)
N1	NI1	N4	88.7(6)	C2	C3	C4	107(1)
N2	NI1	N3	89.3(5)	C2	C3	C23	124(2)
N2	NI1	N4	171.7(5)	C4	C3	C23	129(2)
N3	NI1	N4	91.8(6)	N2	C4	C3	111(1)
NI1	N1	C16	125(1)	N2	C4	C5	124(1)
NI1	N1	C19	126.5(8)	C3	C4	C5	125(1)

Table 8.5 (b) (continued)

C16	N1	C19	107(1)	C4	C5	C6	119(1)
NI1	N2	C1	125.6(9)	C4	C5	C45	118(1)
NI1	N2	C4	128(1)	C6	C5	C45	123(2)
C1	N2	C4	105(1)	N3	C6	C5	124(2)
NI1	N3	C6	126(1)	N3	C6	C7	112(1)
NI1	N3	C9	129.1(8)	C5	C6	C7	122(1)
C6	N3	C9	104(1)	C6	C7	C8	102(1)
NI1	N4	C11	126(1)	C6	C7	C24	131(2)
NI1	N4	C14	132(1)	C8	C7	C24	127(2)
C11	N4	C14	103(1)	C7	C8	C9	108(2)
C38	N5	C39	125(1)	C7	C8	C25	125(2)
C50	N6	C51	123(1)	C9	C8	C25	127(1)
C41	N7	C42	117(2)	N3	C9	C8	114(1)
C53	N8	C54	120(2)	N3	C9	C10	122(2)
N2	C1	C2	110(1)	C8	C9	C10	124(2)
N2	C1	C20	123(1)	C9	C10	C11	124(2)
C2	C1	C20	126(2)	N4	C11	C10	123(1)
C1	C2	C3	106(2)	N4	C11	C12	111(2)
C10	C11	C12	124(2)	C2	C21	C22	113(1)
C11	C12	C13	110(2)	C8	C25	C26	111(2)
C11	C12	C27	127(2)	C12	C27	C28	111(1)
C13	C12	C27	123(1)	C18	C31	C32	112(2)
C12	C13	C14	102(1)	C15	C33	C34	119(1)
C12	C13	C29	129(2)	C15	C33	C38	122(1)
C14	C13	C29	130(2)	C34	C33	C38	120(1)
N4	C14	C13	114(2)	C33	C34	C35	119(2)
N4	C14	C15	121(1)	C34	C35	C36	120(2)
C13	C14	C15	126(1)	C35	C36	C37	121(2)
C14	C15	C16	123(1)	C36	C37	C38	119(2)
C14	C15	C33	116(2)	N5	C38	C33	114(1)
C16	C15	C33	121(2)	N5	C38	C37	124(2)
N1	C16	C15	124(2)	C33	C38	C37	121(2)
N1	C16	C17	107(1)	O1	C39	N5	129(2)
C15	C16	C17	128(1)	O1	C39	C40	123(2)
C16	C17	C18	107(2)	N5	C39	C40	108(1)
C16	C17	C30	127(2)	C39	C40	C41	121(2)
C18	C17	C30	127(2)	C39	C40	C44	125(1)
C17	C18	C19	109(2)	C41	C40	C44	114(2)
C17	C18	C31	126(2)	N7	C41	C40	126(2)
C19	C18	C31	125(1)	N7	C42	C43	124(2)
N1	C19	C18	109(1)	C42	C43	C44	119(2)
N1	C19	C20	124(2)	C40	C44	C43	119(2)
C18	C19	C20	127(2)	C5	C45	C46	120(1)
C1	C20	C19	126(2)	C5	C45	C50	121(1)
C46	C45	C50	119(1)	C45	C46	C47	120(2)
C46	C47	C48	121(2)	C47	C48	C49	118(1)
C48	C49	C50	123(2)	N6	C50	C45	115(1)

Table 8.5 (b) (continued)

N6	C50	C49	127(2)	C45	C50	C49	119(2)
O2	C51	N6	123(2)	O2	C51	C52	124(2)
N6	C51	C52	113(1)	C51	C52	C53	115(1)
C51	C52	C56	127(2)	C53	C52	C56	118(2)
N8	C53	C52	119(1)	N8	C54	C55	122(2)
C54	C55	C56	119(2)	C52	C56	C55	122(2)

Table 8.6 Least-squares Planes

(a) [Ni(DPE)]-$(py)_2$.$2CHCl_3$

Plane number 1		
Atoms Defining Plane	Distance	esd
N1	0.1097	0.0034
N2	-0.1184	0.0035
N3	0.1082	0.0034
N4	-0.1077	0.0033
Additional Atoms	Distance	
NI1	-0.0048	

Mean deviation from plane is 0.1110 angstroms

Plane number 2		
Atoms Defining Plane	Distance	esd
N1	0.1030	0.0034
N2	-0.1344	0.0035
N3	0.1049	0.0034
N4	-0.1019	0.0033
C1	0.0143	0.0040
C2	0.4596	0.0043
C3	0.7541	0.0043
C4	0.4814	0.0043
C5	0.4412	0.0046
C6	0.0185	0.0046
C7	-0.3825	0.0047
C8	-0.7959	0.0046
C9	-0.5597	0.0043
C10	-0.5242	0.0042
C11	-0.0523	0.0042
C12	0.3647	0.0044
C13	0.7702	0.0043
C14	0.5585	0.0042
C15	0.5705	0.0044
C16	0.0953	0.0042
C17	-0.3310	0.0043
C18	-0.8203	0.0043
C19	-0.5534	0.0039
C20	-0.4519	0.0040

Mean deviation from plane is 0.3935 angstroms

Dihedral angles between least-squares planes

plane	plane	angle
2	1	0.33

Table 8.6 (a) (continued)

Plane number 3

Atoms Defining Plane	Distance	esd
N1	-0.0230	0.0034
C1	0.0218	0.0039
C2	-0.0079	0.0042
C3	-0.0127	0.0043
C4	0.0313	0.0043

Mean deviation from plane is 0.0193 angstroms

Dihedral angles between least-squares planes

plane	plane	angle
3	1	161.26
3	2	161.53

Plane number 4

Atoms Defining Plane	Distance	esd
N2	-0.0197	0.0035
C6	0.0129	0.0044
C7	0.0123	0.0046
C8	-0.0306	0.0045
C9	0.0345	0.0043

Mean deviation from plane is 0.0220 angstroms

Dihedral angles between least-squares planes

plane	plane	angle
4	1	19.91
4	2	20.07
4	3	154.82

Plane number 5

Atoms Defining Plane	Distance	esd
N3	0.0134	0.0034
C11	-0.0091	0.0041
C12	-0.0056	0.0043
C13	0.0185	0.0043
C14	-0.0236	0.0042

Mean deviation from plane is 0.0140 angstroms

Dihedral angles between least-squares planes

plane	plane	angle
5	1	20.49
5	2	20.79
5	3	140.92
5	4	27.79

Table 8.6 (a) (continued)

Plane number 6

Atoms Defining Plane	Distance	esd
N4	-0.0286	0.0033
C16	0.0147	0.0041
C17	0.0232	0.0042
C18	-0.0480	0.0042
C19	0.0518	0.0039

Mean deviation from plane is 0.0333 angstroms

Dihedral angles between least-squares planes

plane	plane	angle
6	1	22.53
6	2	22.38
6	3	148.92
6	4	42.45
6	5	30.37

Plane number 7

Atoms Defining Plane	Distance	esd
C34	-0.0024	0.0044
C33	0.0023	0.0043
C35	0.0002	0.0051
C36	0.0039	0.0056
C37	-0.0043	0.0059
C38	-0.0001	0.0052

Mean deviation from plane is 0.0022 angstroms

Dihedral angles between least-squares planes

plane	plane	angle
7	1	111.95
7	2	112.21
7	3	49.35
7	4	114.20
7	5	91.90
7	6	105.92

Table 8.6 (a) (continued)

Plane number 8

Atoms Defining Plane	Distance	esd
C39	0.0143	0.0039
C40	-0.0028	0.0046
C41	-0.0170	0.0050
C42	0.0146	0.0048
C43	0.0059	0.0050
C44	-0.0167	0.0041

Mean deviation from plane is 0.0119 angstroms

Dihedral angles between least-squares planes

plane	plane	angle
8	1	63.62
8	2	63.89
8	3	97.66
8	4	67.00
8	5	43.32
8	6	63.51
8	7	48.63

Plane number 9

Atoms Defining Plane	Distance	esd
C52	0.0045	0.0043
C53	-0.0041	0.0050
C54	-0.0005	0.0053
C55	0.0036	0.0054
N8	-0.0008	0.0045
C56	-0.0038	0.0050

Mean deviation from plane is 0.0029 angstroms

Dihedral angles between least-squares planes

plane	plane	angle
9	1	85.95
9	2	86.27
9	3	82.00
9	4	72.83
9	5	70.62
9	6	100.83
9	7	57.96
9	8	50.50

Table 8.6 (a) (continued)

Plane number 10		
Atoms Defining Plane	Distance	esd
C46	0.0037	0.0044
C47	-0.0126	0.0056
C48	0.0078	0.0065
C49	0.0103	0.0061
N7	-0.0115	0.0047
C50	0.0083	0.0055

Mean deviation from plane is 0.0090 angstroms

Dihedral angles between least-squares planes

plane	plane	angle
10	1	100.27
10	2	100.60
10	3	64.21
10	4	91.50
10	5	81.38
10	6	108.59
10	7	36.07
10	8	46.87
10	9	22.44

Table 8.6 (continued)

(b) $[Ni(DPE)]\text{-}(py)_2.H_2O$

Plane number 1		
Atoms Defining Plane	Distance	esd
N1	0.1244	0.0122
N2	-0.1345	0.0128
N3	0.0975	0.0110
N4	-0.1254	0.0126
Additional Atoms	Distance	
NI1	0.0089	

Mean deviation from plane is 0.1205 angstroms

Table 8.6 (b) (continued)

Plane number 2

Atoms Defining Plane	Distance	esd
N1	0.1169	0.0122
N2	-0.0879	0.0128
N3	0.1713	0.0110
N4	-0.1056	0.0126
C1	-0.4634	0.0135
C2	-0.7661	0.0146
C3	-0.4912	0.0128
C4	-0.0210	0.0149
C5	0.5500	0.0141
C6	0.6815	0.0148
C7	1.0522	0.0163
C8	0.5323	0.0180
C9	0.0422	0.0162
C10	-0.3995	0.0150
C11	-0.4821	0.0136
C12	-0.6822	0.0136
C13	-0.3976	0.0144
C14	0.0181	0.0136
C15	0.4786	0.0152
C16	0.5633	0.0141
C17	0.9669	0.0173
C18	0.5428	0.0157
C19	0.0305	0.0167
C20	-0.3829	0.0132

Mean deviation from plane is 0.4178 angstroms

Dihedral angles between least-squares planes

plane	plane	angle
2	1	1.27

Table 8.6 (b) (continued)

Plane number 3

Atoms Defining Plane	Distance	esd
N1	-0.0338	0.0119
C16	0.0549	0.0143
C17	-0.0579	0.0162
C18	0.0269	0.0154
C19	0.0182	0.0161

Mean deviation from plane is 0.0383 angstroms

Dihedral angles between least-squares planes

plane	plane	angle
3	1	155.56
3	2	156.74

Plane number 4

Atoms Defining Plane	Distance	esd
N2	-0.0312	0.0128
C1	0.0251	0.0136
C2	-0.0122	0.0142
C3	-0.0097	0.0127
C4	0.0334	0.0151

Mean deviation from plane is 0.0223 angstroms

Dihedral angles between least-squares planes

plane	plane	angle
4	1	18.13
4	2	18.54
4	3	151.10

Plane number 5

Atoms Defining Plane	Distance	esd
N3	0.0239	0.0110
C6	-0.0475	0.0145
C7	0.0491	0.0170
C8	-0.0217	0.0174
C9	-0.0164	0.0157

Mean deviation from plane is 0.0317 angstroms

Dihedral angles between least-squares planes

plane	plane	angle
5	1	23.56
5	2	24.64
5	3	132.22
5	4	33.02

Table 8.6 (b) (continued)

Plane number 6

Atoms Defining Plane	Distance	esd
N4	0.0276	0.0123
C11	-0.0215	0.0135
C12	0.0040	0.0134
C13	0.0175	0.0144
C14	-0.0311	0.0134

Mean deviation from plane is 0.0203 angstroms

Dihedral angles between least-squares planes

plane	plane	angle
6	1	161.73
6	2	162.44
6	3	26.39
6	4	144.09
6	5	149.67

Plane number 7

Atoms Defining Plane	Distance	esd
N7	-0.0136	0.0145
C40	0.0070	0.0160
C41	0.0133	0.0161
C42	-0.0009	0.0191
C43	0.0291	0.0194
C44	-0.0249	0.0164

Mean deviation from plane is 0.0148 angstroms

Dihedral angles between least-squares planes

plane	plane	angle
7	1	83.83
7	2	83.79
7	3	87.64
7	4	101.33
7	5	72.56
7	6	111.18

Table 8.6 (b) (continued)

Plane number 8

Atoms Defining Plane	Distance	esd
N8	-0.0051	0.0147
C52	0.0159	0.0124
C53	-0.0153	0.0141
C54	0.0267	0.0175
C55	-0.0159	0.0162
C56	-0.0115	0.0168

Mean deviation from plane is 0.0150 angstroms

Dihedral angles between least-squares planes

plane	plane	angle
8	1	117.03
8	2	117.45
8	3	66.18
8	4	98.92
8	5	119.44
8	6	45.53
8	7	152.87

Plane number 9

Atoms Defining Plane	Distance	esd
C45	0.0049	0.0129
C46	-0.0060	0.0156
C47	-0.0024	0.0151
C48	0.0095	0.0158
C49	-0.0056	0.0132
C50	-0.0005	0.0147

Mean deviation from plane is 0.0048 angstroms

Dihedral angles between least-squares planes

plane	plane	angle
9	1	124.31
9	2	124.88
9	3	56.73
9	4	106.43
9	5	122.93
9	6	37.66
9	7	143.18
9	8	9.71

Table 8.6 (b) (continued)

Plane number 10

Atoms Defining Plane	Distance	esd
C33	0.0054	0.0150
C34	0.0043	0.0172
C35	-0.0221	0.0200
C36	0.0235	0.0196
C37	-0.0083	0.0184
C38	-0.0038	0.0152

Mean deviation from plane is 0.0112 angstroms

Dihedral angles between least-squares planes

plane	plane	angle
10	1	63.33
10	2	63.72
10	3	115.66
10	4	45.19
10	5	71.17
10	6	99.18
10	7	143.67
10	8	53.74
10	9	61.67

REFERENCES

1. Yang, R.; Chang, C. K. J. Am. Chem. Soc. 1985, 107, 898.

2. Woo, L. K.; Maurya, M. R.; Tolppi, C. J.; Jacobson, R. A.; Yang, S. Inorg. Chim. Acta (in press).

3. Cotton, F. A.; Francis, R. J. Am. Chem. Soc. 1960, 82, 2986.

4. Cromer, D. T.; Waber, J. T. International Tables for X-ray Crystallography, Vol. IV, The Kynoch Press, Birmingham, England, 1974, Table 2.2 A.

5. Ibers J. A.; Hamilton, W. C. Acta Crystallgr. 1964, 17, 781.

6. Cromer, D. T. International Tables for X-ray Crystallography, Vol. IV, The Kynoch Press, Birmingham, England, 1974, Table 2.3.1.

7. TEXSAN - TEXRAY Structure analysis package, Molecular Structure Corporation, 1985.

8. Buckingham, D. A.; Gunter, M. J.; Mander, L. N. J. Am. Chem. Soc. 1978, 100, 2899.

9. Meyer Jr., E. F. Acta Crystagr. 1972, 28B, 2162.

10. Hamor, T. A.; Caughey, W. S.; Hoard, J. L. J. Am. Chem. Soc. 1965, 87, 2305.

11. Fleischer, E. B. J. Am. Chem. Soc. 1963, 85, 146.

12. Gallucci, J. C.; Swepston, P. N.; Ibers, J. A. Acta Crystagr. 1982, 38B, 2134.

13. Cullen, D. L.; Meyer, E. F. J. Am. Chem. Soc. 1974, 96, 2095.

14. Pace, L. J.; Martinsen, J.; Ulman, A.; Hoffman B. M.; Ibers, J. A. J. Am. Chem. Soc. 1983, 105, 2612.

SUMMARY

This dissertation basically includes two parts: ultrafast laser spectroscopy and X-ray crystallography. Most of this work are related to photosynthesis.

In the first part, polarized pump-probe ultrafast spectroscopy was used to investigate the electron excitation transport in native photosystem I particles from spinach (Chl/P700~200, Chl/P700~60) and bacteriochlorophyll a-protein complex from the green sulfur bacterium Prosthecochloris aestuarii. Considerable residual anisotropy observed at long times in all of the three samples indicate the nonrandom chromophore orientations. Two transfer mechanisms (weak-coupling and strong-coupling) were tested in the investigation. The relatively slow depolarization times (5-13ps in Chl/P700~200; 2.9-6.6ps in Chl/P700~60; 4.78ps (603 nm in Bchl a-protein) suggests that the depolarization accompanies electronic excitation transport between clusters of (B)Chls chromophores rather than between individual nearest-neighbor chromophores. A common picture obtained for the three samples is that "strong-coupling" exists between the chls within the cluster (Bchls or Chls), "weak-coupling" governs the transfer between the clusters. A dynamic model has been proposed based on the X-ray structure of Bchl a-protein and the our results. In the model, protein subunits are arranged as a trimer (3-fold axis symmetry),

the depolarization life time $\tau=1/3w_{AB}$, and the residual anisotropy parameter $a = (3\gamma^2-1)^2/4$, where w_{AB} is the hopping rate between subunits in the same trimer and γ is the projection of exciton moment along the 3-fold axis.

In the second part of this thesis, X-ray diffraction and molecular mechanics were employed in the determination of the crystal and molecular structures of Mg porphrin and other metal porphrin compounds. The crystallographic parameters for these four compounds are shown in Table 9.1. The intermolecular hydrogen bonding observed in the structure of (H_2O)MgT(OME)PP provides further support for a model of chlorophyll aggregation in photosynthetic organisms. Chlorophyll aggregation system is believed to be the main organization of antenna chlorophyll in chromosomes. The structures of the three Ni porphyrine complexes lead to the possibility of synthesizing an oligmeric complex, which could be very important in developing new materials.

As we know, a detailed picture of electron excitation transfer in photosynthesis has not yet been obtained, although important advances have been made in recent years. New experiments and techniques need to be designed and developed. One of the most important would be the development of femtosecond laser spectroscopy, as a number of questions can only be answered on that time scale.

Table 9.1 Crystallographic parameters for four metalloporphyrins.

Crystal Name	Lattice	Crystal parameters	Space Group	R R_w	$(M-N)_{ave}$ (Å)	$(N-M-N)_{ave}$ (°)
$(H_2O)MgT(OME)PP \bullet CHCL_3$	monoclinic	a=15.966(5)Å b= 9.192(1)Å β=100.38(2)° c=14.882(4)Å v=2148.2(9)Å^3	I_2	0.068 0.070	2.086	88.1
[cis-$(ala)_2$DPE]Ni(II)$\bullet CHCl_3 \bullet CH_3OH$	monoclinic	a=14.195(5)Å b=12.175(6)Å β=98.97(3)° c=28.071(1)Å v=4792(3)Å^3	$P2_1/n$	0.085 0.089	1.92	90.2
[Ni(DPE)]-$(py)_2 \bullet 2CHCl_3$	triclinic	a=14.306(4)Å α=94.86° b=14.719(5)Å β=98.97(3)° c=14.296(5)Å γ=63.45(2)° v=2674(2)Å^3	PĪ	0.049 0.064	1.92	90.2
[Ni(DPE)]-$(py)_2 \bullet H_2O$	monoclinic	a=14.240(2)Å b=25.418(4)Å β=96.38(3)° c=14.725(5)Å v=4740(4)Å^3	$P2_1/n$	0.081 0.107	1.93	90.2

ACKNOWLEDGEMENTS

First of all, I am sincerely grateful to my research advisers, Professors Robert A. Jacobson and Walter Struve, for the guidance, training and support they gave me during the whole program. It is hard to imagine that ultrafast laser spectroscopy and X-ray crystallography could be combined together without their coorperation. The work contained in this dissertation should belong to them more than to me. I hope I can find a better word than "thanks" to express my gratitude.

I would like to thank Timothy P. Causgrove and Yingzhong Su who first taught me how to use the instruments and equipment in the laboratory.

I sincerely appreciate the help from Brenda and Marlene on the typing of the thesis. Thanks for the Christmas tree which made me feel at home.

I would also like to thank former and current group members: Sandy Bellefeuille, Paul Lyle, Tom Hendrixson, Cathy Day and Sharon Ringrose for their help and friendship.

Special thanks should give my husband, Lubo Zhang, and my little daughter, Sandra Zhang, for their love and encouragement.

Finally, I dedicate this dissertation to my parents, Jianhua Yang and Fenglian Lu. It is they who first led me into the field of science and encouraged me to keep going on this long way.

This work was performed at Ames Laboratory under contract no. W-7405-eng-82 with the U.S. Department of Energy. The United States government has assigned the DOE Report number IS-T 1513 to this thesis.